SUPERSYMMETRIC DARK MATTER AND PROSPECTS FOR ITS DETECTION

by

Takahiro Yamamoto

A dissertation submitted to the faculty of
The University of Utah
in partial fulfillment of the requirements for the degree of

Doctor of Philosophy

in

Physics

Department of Physics and Astronomy

The University of Utah

May 2017

The University of Utah Graduate School

STATEMENT OF DISSERTATION APPROVAL

The dissertation of **Takahiro Yamamoto**
has been approved by the following supervisory committee members:

Pearl Sandick ,	Chair(s)	**21 Feb 2017** Date Approved
Carlton DeTar ,	Member	**21 Feb 2017** Date Approved
Robert Wayne Springer ,	Member	**21 Feb 2017** Date Approved
Zheng Zheng ,	Member	**21 Feb 2017** Date Approved
Jeffrey Phillips ,	Member	**21 Feb 2017** Date Approved

by **Benjamin C. Bromley** , Chair/Dean of
the Department/College/School of **Physics**
and by **David B. Kieda** , Dean of The Graduate School.

ABSTRACT

Dark matter is a prominent and dominant form of matter in the Universe. Yet, despite various intense efforts, its nongravitational effects have not been observed. In this dissertation, we explore the nature of such elusive particles within a supersymmetric $SU(3)_{\mathrm{C}} \otimes SU(2)_{\mathrm{L}} \otimes U(1)_Y$ gauge theory. Although large regions of parameter space within supersymmetric models have been excluded by recent results from collider experiments and direct and indirect dark matter searches, we find that there is a wide range of viable parameter space once the requirements of minimal flavor violation and mass universality are relaxed. In particular, we focus on a class of models in which electroweak-scale Majorana dark matter has interactions with the Standard Model sector via relatively light charged scalars with large chiral mixing and CP-violation. Our model is shown to lead to enhanced dark matter pair annihilation, and is constrained by precise measurements of the lepton dipole moments. We illustrate that our model satisfies all constraints, including the observed thermal relic density, and investigate prospects for the detection of dark matter annihilation products. We also examine the effects of chiral mixing and CP-violation on the variation in the ratio of the flux of monoenergetic photons from annihilation to two photons relative to that from annihilation to a photon and a Z boson, as well as the helicity asymmetry in the diphoton final state. We also find the most general spectrum for internal bremsstrahlung, which interpolates between the regimes dominated by virtual internal bremsstrahlung and by final state radiation, and that it provides distinctive γ-ray signals, which could potentially be observed in the near future.

CONTENTS

LIST OF FIGURES

LIST OF TABLES

ACKNOWLEDGEMENTS

I am grateful for the extraordinary and continuous support from my supervisor, Professor Pearl Sandick. The completion of this dissertation could not have been possible without her expertise and fruitful advice. I am also indebted to Professor Jason Kumar for his keen insights, and to other collaborators with whom I have had the privilege of working: Professor Chris Kelso, Dr. Keita Fukushima, and Dr. Fei Teng.

I would also like express my gratitude to Professor Carleton DeTar, Professor Wayne Springer, Professor Zheng Zheng, and Professor Jeff Phillips for their helpful suggestions and for serving on my dissertation committee.

My special thanks go to Paul Bergeron for his much appreciated support and helpful suggestions over the years, as well as to Dr. Kuver Sinha for his useful comments.

I would also like to thank the American Physical Society, Springer-Verlag Berlin Heidelberg and Società Italiana di Fisica, The National Aeronautics and Space Administration (NASA), The Space Telescope Science Institute (STScI), National Optical Astronomy Observatory (NOAO), and Professor Stephen P. Martin for granting permission to use copyrighted materials.

Finally I wish to thank University of Utah for its support and kind hospitality.

CHAPTER 1

HIGH ENERGY PHYSICS AND COSMOLOGY

One of the great mysteries in physics is that the majority of the matter content of the Universe observed by standard cosmology cannot be explained by the standard model of particle physics. Various studies of cosmology and observations of astrophysical phenomena strongly suggest that the majority of the matter in the Universe is invisible, so-called "dark matter."

The nature of dark matter has long been a puzzle in modern physics. It is expected to be a very long-lived and massive particle that carries no electrical or color charge. Currently no such particle exists within the Standard Model (SM) of particle physics.

The progress of cosmology provides some insights on what the underlying new physics should be at a high energy scale beyond the reach of accelerator experiments on Earth, while progress in particle physics provides more accurate pictures of the early Universe. The latter even provides various ideas of new physics beyond the SM of particle physics, which includes supersymmetric gauge theories.

In this chapter, I will briefly discuss our current understanding of particle physics and cosmology, and then reveal the inconsistency of those successful theories when amalgamated together. I will also explain in detail how the existence of cold dark matter has been established with supporting evidence, which implies an urgent need for new physics, as well as the ongoing detection strategies for such particles. Next, the supersymmetric extension of the Standard Model of particle physics is briefly introduced, followed by a detailed discussion of its implications for particle physics phenomenology, including probable candidates for dark matter particles, along with their properties.

1.1 The Standard Model of particle physics

Attempts to construct convincing theories that describe high energy phenomena deduced from a few fundamental principles have seen great success in modern physics (see,

for example, Ref. [5, 28–31]). The SM of particle physics has been established based on Lorentz invariance and the gauge principle, in which the forms of interactions among scalar bosons, chiral fermions, and vector bosons are determined so that they preserve the local gauge symmetry, then followed by electroweak symmetry breaking due to the Brout-Englert-Higgs (BEH) mechanism [32, 33].

The SM has withstood strict and meticulous scrutiny for decades. Collider experiments up to the energy scale of 7-8 TeV, as well as measurements of rare processes and the magnetic moments of the SM leptons show consistency of the SM predictions with measurements to high precision. The recent discovery of a long-sought particle, the Higgs boson [34–37], represents the final piece of the SM content.

The SM is a non-Abelian type gauge theory with the group structure $SU(3)_{\rm C} \bigotimes SU(2)_{\rm L} \bigotimes U(1)_Y$, with the electroweak (EW) gauge $SU(2)_{\rm L} \bigotimes U(1)_Y$ spontaneously broken into $U(1)_{\rm EM}$ by the BEH mechanism, while the gauge group $SU(3)_{\rm C}$ describing chromodynamics remains unbroken, leaving the eight associated gluons massless. The electroweak part of the SM Lagrangian is given by

$$\mathcal{L}_{\rm EW} = \mathcal{L}_{\rm gauge} + \mathcal{L}_{\rm Higgs} + \mathcal{L}_{\rm Yukawa}. \tag{1.1}$$

The Weinberg-Salam model [38] contains three $SU(2)_{\rm L}$ gauge bosons, $W_\mu^{1,2,3}$, and a $U(1)_Y$ gauge boson, B_μ, with kinetic energy terms

$$\mathcal{L}_{\rm gauge} = -\frac{1}{4}\sum_{i=1,2,3} W^i_{\mu\nu}W^{i\mu\nu} - \frac{1}{4}B_{\mu\nu}B^{\mu\nu} + \sum_{\rm fermions} i\bar{F}\not{D}F + \sum_{\rm fermions} i\bar{f}_R\not{D}f_R, \tag{1.2}$$

where

$$\begin{aligned} W^i_{\mu\nu} &= \partial_\mu W^i_\nu - \partial_\nu W^i_\mu - g\epsilon^{ijk}W^j_\mu W^k_\nu \\ B_{\mu\nu} &= \partial_\mu B_\nu - \partial_\nu B_\mu \end{aligned} \tag{1.3}$$

are the field strengths of the vector bosons. The $SU(2)_{\rm L}$ doublet fermion F refers to $L = (\nu_L\ e_L)^T$ and $Q = (u_L\ d_L)^T$, and the $SU(2)_{\rm L}$ singlet fermion f_R refers to e_R, u_R, and d_R, for three generations. The covariant derivative is given by $D_\mu = \partial_\mu - ig\frac{\sigma^i}{2}W^i_\mu - ig'YB_\mu$ for $SU(2)_{\rm L}$ doublets with weak hypercharge Y, and $D_\mu = \partial_\mu - ig'YB_\mu$ for $SU(2)_{\rm L}$ singlets, where g' and g are the $U(1)_Y$ and $SU(2)_{\rm L}$ gauge couplings, respectively.

The Higgs field, which is a complex scalar $SU(2)_{\rm L}$ doublet, $\Phi = (\phi^+ \phi^0)^T$, enters the SM in such a way that the Higgs interaction in the electroweak gauge theory is of the form

$$\mathcal{L}_{\rm Higgs} = \left(D_\mu \Phi\right)^\dagger \left(D^\mu \Phi\right) - V(\Phi^\dagger, \Phi), \tag{1.4}$$

with the most general, renormalizable, and $SU(2)_{\rm L}$ gauge invariant scalar potential

$$V(\Phi^\dagger, \Phi) = -\mu^2 \left|\Phi^\dagger \Phi\right| + \lambda \left|\Phi^\dagger \Phi\right|^2. \tag{1.5}$$

When μ^2 is positive, the Higgs field develops a vacuum expectation value (VEV), $\langle \phi^0 \rangle = v/\sqrt{2} = \mu/\sqrt{2\lambda}$, triggering electroweak symmetry breaking (EWSB). Consequently, some of the gauge bosons acquire mass, mixing into mass eigenstates such as $W^\pm_\mu = (W^1_\mu \mp iW^2_\mu)/\sqrt{2}$ with $m_W = gv/2$, $Z_\mu = -\sin\theta_W B_\mu + \cos\theta_W W^3_\mu$ with $m_Z = \sqrt{g^2 + g'^2}v/2$, while $A_\mu = \cos\theta_W B_\mu + \sin\theta_W W^3_\mu$ remains massless. Here θ_W is defined by $\cos\theta_W = g/\sqrt{g^2 + g'^2}$ and $\sin\theta_W = g'/\sqrt{g^2 + g'^2}$. The Higgs boson itself acquires mass of $m_h = \sqrt{2\lambda}v$ at tree-level. The value of the EW VEV is determined by $v^2 = 1/\sqrt{2}G_F \approx (246\,\text{GeV})^2$ [5], where G_F is the Fermi constant, which is obtained by the measured muon lifetime $\tau_\mu^{-1} \approx G_F^2 m_\mu^5/192\pi^3$, in the limit $m_e \ll m_\mu$.

The electric charge, the coupling constant to the gauge boson of the $U(1)_{\rm EM}$ subgroup, also know as the photon, is determined by $Q = T^3 + Y$, where T^3 denotes the z-component of the isospin.

The electroweak gauge-invariant Yukawa coupling of the Higgs field to the up- and down- type quarks is

$$\mathcal{L}_{\rm Yukawa} = -\lambda_u \bar{Q} \Phi^c u_R - \lambda_d \bar{Q} \Phi d_R + h.c., \tag{1.6}$$

where $\Phi^c = -i\sigma^2 \Phi^*$. The fermion mass is generated as the Higgs field acquires a VEV, with $m_{u,d} = \lambda_{u,d} v/\sqrt{2}$. The tree-level mass of fermions is determined by the magnitude of the Yukawa coupling constant. The same mechanism can be applied to the charged lepton interactions with the Higgs field terms, analogous to the down-type quarks. Meanwhile, due to the absence of its right-handed partner in the SM content, the up-type leptons, known as neutrinos, remain massless. All the matter content and the gauge force carriers in the SM are listed in Table 1.1 and Table 1.2, with their charges and masses [5, 34–36, 39, 40]. The upper limits on neutrino masses are measured by tritium decay. The value of the top

Table 1.1. The matter content of the SM.

	Flavor	Charge	Mass
Leptons (up type)	ν_e ν_μ ν_τ	0	$\lesssim 2$ eV
Leptons (down type)	e μ τ	$+1$	0.511 MeV $\lesssim 105.6$ MeV 1777 MeV
Quarks (up type)	u c t	$+2/3$	$2.3^{+0.7}_{-0.5}$ MeV 1.275(25) GeV 173.07(52)(72) GeV
Quarks (down type)	d s b	$-1/3$	$4.8^{+0.5}_{-0.3}$ MeV $\lesssim 95(5)$ MeV 4.18(3) GeV

Table 1.2. The Higgs boson and the force carriers of the SM.

	Boson	Charge	Mass
	h	0	125.3(4)(5) GeV
Electromagnetic Force	γ	0	0
Weak Force	W	± 1	80.376(33) GeV
	Z	0	91.2 GeV
Strong Force	g	0	0

quark mass is from direct measurements. The mass of the bottom quark is evaluated as $m_b(\overline{\text{MS}})$.

Various meticulous tests of the SM have been conducted, including precise measurements of electroweak parameters, rare decays and the dipole moments of fermionic particles, up to the energy scale of 7-8 TeV, the highest energies accessible to current accelerator experiments. Yet the SM still withstands such scrutiny, and there are no unambiguous hints of new physics beyond it. The recent discovery of the Higgs boson also shows consistency with the SM.

Assuming that new physics enters at a high scale of 10^{19} GeV and that a Landau pole below this scale is absent, the two-loop upper bound for the Higgs mass within the SM is $m_h \leq 180 \pm 4 \pm 5$ GeV [41], where the first error indicates the theoretical uncertainty and the second error reflects the experimental uncertainty in the measurement of the top

quark mass. Precision electroweak measurements at the Large Electron-Positron Collider, or LEP-II, found the 95% confidence level (CL) upper limit for m_h to be 158 GeV, with a lower limit of 114.4 GeV [42] before discovery of the Higgs boson at the Large Hadron Collider (LHC), which is consistent with the measured value. Note, however, that the measurements of the Higgs and top quark masses indicate that the electroweak vacuum is a metastable state [43, 44].

Although it is a successful description of high energy phenomena, the SM possesses some serious problems. In the SM, as mentioned above, electroweak symmetry is broken with a single Higgs $SU(2)_{\mathrm{L}}$ doublet and the existence of a fundamental scalar field in the theory leads to quadratic divergences at higher energies due to radiative corrections involving all species of particles that couple to the Higgs field, requiring a fine tuning of the high energy parameters. Later we will revisit this issue in more detail. This is a primary reason why it is expected that there exists new physics which should appear at some energy between the electroweak scale and the Planck scale $m_{\mathrm{Planck}} = (8\pi G)^{-1/2} = 2.4 \times 10^{18}\,\mathrm{GeV}$, where quantum gravitational effects supposedly become apparent. Precise tests of the SM have been extensively carried out in the hopes of capturing signals of new physics.

1.2 The Λ-CDM model

Precise knowledge of high-energy physics and space-time dynamics are essential to investigate the evolutionary history of the Universe. Currently, the evolution of the Universe is most commonly described by the Friedmann-Robertson-Walker cosmology, which is based on the assumption that space-time dynamics is governed by Einstein's equations, and the observations that the Universe's expansion initiated from the Hot Big Bang, and that it is almost spatially flat, homogeneous, and isotropic on large scales [45, 46]. In terms of the density parameters, the Friedmann equation, which was derived in 1922, can be written

$$1 - \Omega_{\mathrm{tot}}(t) = -\frac{\kappa}{R_0^2 a^2(t) H^2(t)}. \tag{1.7}$$

Here the dimensionless density parameter $\Omega_{\mathrm{tot}}(t) = \rho(t)/\rho_c(t)$ is the ratio of the energy density contributed by all the components of the Universe, $\rho(t)$, to the critical density, $\rho_c(t) = 3H^2(t)/8\pi G$. κ denotes the sign of the curvature: the Universe is positively curved

if $\kappa = +1$, negatively curved if $\kappa = -1$, and flat if $\kappa = 0$. The spatial curvature can be determined from the other parameters in Eq. (1.7). If κ is nonzero, R_0 is the radius of curvature of the Universe, as measured at the present moment. $a(t)$ is a scale factor, which describes how the scale of length evolves in time during the Universe expansion, $r(t) = a(t)r(t_0)$. The scale factor is totally independent of location or direction and normalized to $a(t_0) = 1$ at the present moment. $H(t) = \dot{a}(t)/a(t)$ denotes the time evolution of the Hubble constant, which relates the radial recession velocity, v, of a nearby galaxy moving away from Earth to its distance, r, known as Hubble's law: $v = H_0 r$, discovered by Edwin Hubble in 1929 [47]. The present epoch value $H_0 = (\dot{a}/a)_{t=t_0}$ is often replaced by a constant h, defied by $H_0 = 100h$ km s^{-1} Mpc^{-1}. The Friedmann equation relates the curvature of the Universe, described by $a(t)$, κ, and R_0, to the energy density of the contents of the Universe. The total energy density consists of multiple components $\Omega_{\rm tot} = \Omega_m + \Omega_r + \Omega_\Lambda$, where each Ω_i is the density parameter for matter species, radiation, and the cosmological constant Λ in the Universe, respectively. The radiation density consists of that due to photons and neutrinos, $\Omega_r = \Omega_\gamma + \Omega_\nu$. Note that the right hand side of Eq. (1.7) does not change its sign during the evolution of the Universe. The complete present-epoch state of the homogeneous Universe can be described by the current-epoch values of all the density parameters and the Hubble constant.

These parameters also allow one to trace the history of the Universe back, at least until an epoch where interactions allow interchanges between the densities of the different species, shortly before Big Bang Nucleosynthesis (BBN). We can rewrite the Friedmann equation without explicitly including the curvature. In terms of the present-epoch parameters, it becomes:

$$\frac{H^2}{H_0^2} = \frac{\Omega_{r,0}}{a^4(t)} + \frac{\Omega_{m,0}}{a^3(t)} + \Omega_{\Lambda,0} + \frac{1 - \Omega_{\rm tot,0}}{a^2(t)}, \tag{1.8}$$

where again, $\Omega_{\rm tot,0} = \Omega_{m,0} + \Omega_{r,0} + \Omega_{\Lambda,0}$. During the early stages of expansion, the radiation term dominates the expansion, where the scale factor grows as $a(t) \propto t^{1/2}$. Then over the course of the expansion, it enters the matter-dominated phase, in which $a(t) \propto t^{2/3}$, followed by the curvature-dominated phase. If the Universe continues to expand forever, the cosmological constant term will dominate the expansion, and the scale factor will grow exponentially as $a(t) \propto e^{H_0 t}$. In the standard cosmological model,

radiation-matter equality takes place at a scale factor $a_{rm} = \Omega_{r,0}/\Omega_{m,0} \approx 2.8 \times 10^{-4}$ and matter-Λ equality takes place at $a_{m\Lambda} = (\Omega_{m,0}/\Omega_{\Lambda,0})^{1/3} \approx 0.75$.

Models based on these parameters, referred to as Λ-CDM models, are able to give a good fit to the complete set of observational data available at present. The spectrum of the Cosmic Microwave Background Radiation (CMBR), primordial nucleosynthesis, and the observation of structure formation of the Universe, along with the observation of galaxy and cluster dynamics have pinned downed the content of the Universe today. Among them, the most powerful data source for the determination of cosmological parameters is the CMB.

The CMBR is a powerful tool to investigate the history of the Universe since redshift $z \sim 1100$, the epoch when matter decoupled from photons, and has revealed that the Universe was almost flat, isotropic, and homogenous to a high degree of precision; the temperature of the CMBR across the sky is remarkably uniform: $\delta T/T \simeq 1.1 \times 10^{-5}$ on angular scales ranging from $10''$ to 180°. The radiation density $\Omega_{\gamma,0}$ is accurately measured directly from the CMB blackbody spectrum, and is determined $\Omega_{\gamma,0}h^2 = 2.47 \times 10^{-5}$ [48], corresponding to $T = 2.7255 \pm 0.0006$ K.

The CMB anisotropies are also of particular interest. Both the total intensity and two independent polarization modes are predicted to have anisotropies. The CMB carries a snapshot of the time of last scattering, often called primary anisotropies. The detailed pattern of anisotropies, shown in Figure 1.1, depends on all of the cosmological parameters, and detailed investigation of the pattern affirms the need for both nonrelativistic (or cold) dark matter and dark energy in the cosmological model to provide structure formation that reproduces the observed anisotropies. Such cold dark matter (hereafter, CDM) comprises, with baryonic matter, the total matter component of the density in the Universe, $\Omega_m = \Omega_c + \Omega_b$.

As in Figure 1.1, the anisotropy power spectrum, $\ell(\ell+1)C_\ell^{TT}/2\pi$, features a flat plateau at large angular scales (small ℓ), followed by a series of oscillatory features at higher angular scales. The first and most prominent peak is at approximately 1° ($\ell \simeq 220$) [49, 50]. These features, know as acoustic peaks, exhibit the oscillations of the photon-baryon fluid around the era of decoupling. The cause of those peaks is explained as following: Before recombination, the baryons and photons are tightly coupled, and the perturbations

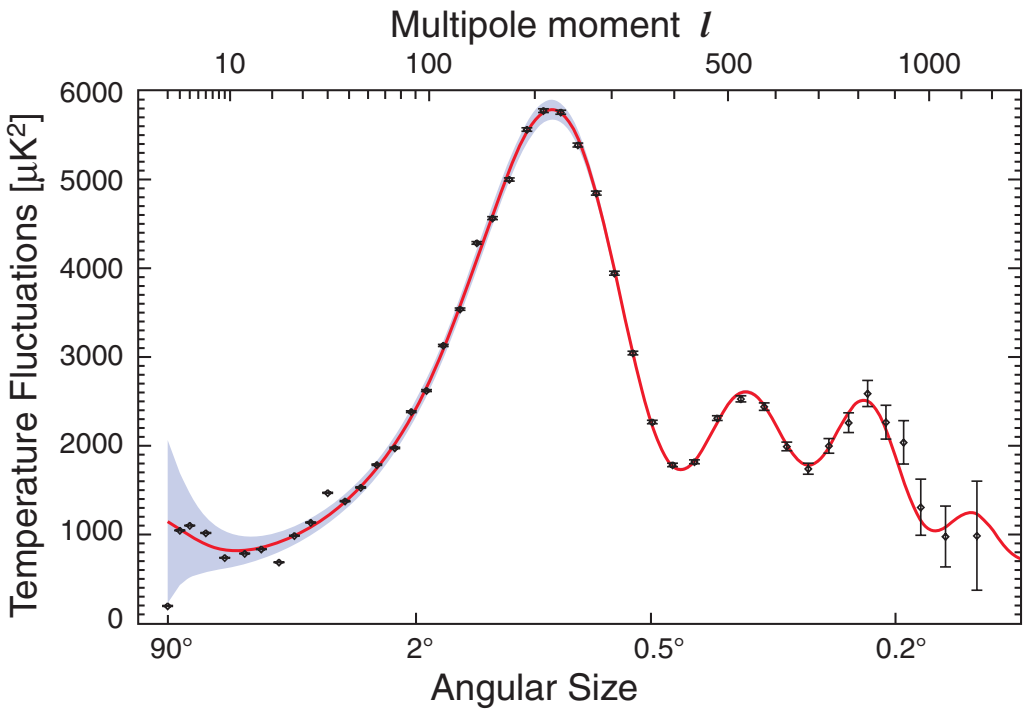

Figure 1.1. Seven-year temperature power spectrum, $\ell(\ell+1)C_\ell^{TT}/2\pi$, from the Wilkinson Microwave Anisotropy Probe (WMAP) [1]. The curve is the Λ-CDM model best fit to the seven-year WMAP data. The gray band represents cosmic variance. The shape of this curve contains a wealth of information about the history the Universe. Courtesy of NASA/WMAP Science Team.

oscillate in the potential wells generated primarily by the dark matter perturbations. After decoupling, the baryons are free to collapse into those potential wells. Since density perturbations grow only in the matter-dominated epoch, and matter domination starts earlier in the presence of DM, density perturbations start to grow earlier when DM is present, therefore allowing an earlier formation of the first galaxies.

Some features of the CMB can be closely related to specific parameters. The sound horizon at the time of last scattering provides the value of the total energy content of the Universe: the angular scale of the first peak is found at 1°, which indicates that the spatial geometry of the Universe is flat, corresponding to an energy density of the Universe being approximately unity $\Omega_{\rm tot} \approx 1$. The relative heights of the peaks probe the baryon density with high accuracy, $\Omega_b h^2 = 0.02226 \pm 0.00023$ [49, 50], which is comparable with the best quoted errors from the BBN. The BBN limits on the abundance of baryonic matter are $0.021 \leq \Omega_b h^2 \leq 0.024$ (95% confidence), which also provide a strong indication that most

of the mass density of the Universe is in a form other than baryons. Moreover many other parameters combine to determine the overall shape. Since radiation has the largest energy density in the Universe before matter-radiation equality, and photons and neutrinos are relativistic, they tend to drag DM particles out of small mass overdensities if they interact with DM during structure formation. Therefore, both the CMB temperature and polarization power spectra are prominent in determining upper limits of the DM-radiation scattering cross section. Planck data provide upper bounds of $8 \times 10^{-31} (m_\chi / \text{ GeV})$ cm^2 for the DM-photon interaction, and $2 \times 10^{-28} (m_\chi / \text{ GeV})$ cm^2 for the DM-neutrino interaction at 68% CL [51].

The indirect determination of H_0 by the Planck Collaboration found $H_0 = 67.8 \pm 0.9$ km s^{-1} Mpc^{-1} [49, 50]. However, there is strong degeneracy of H_0 with other parameters, e.g., $\Omega_{m,0}$ and the neutrino mass, and it is in tension with the value measured from the Hubble Space Telescope Key Project [52]. The most recent derivation suggests that $H_0 = 72.0 \pm 3.0$ km s^{-1} Mpc^{-1} [53]. The determination of these parameters from the CMB presumes a flat Universe. If the assumption of spatial flatness is lifted, it turns out that the CMB on its own only weakly constrains the spatial curvature, due to a parameter degeneracy in the angular-diameter distance. However, inclusion of other data readily removes this. For instance, adding the usual non-CMB data-sets, such as the distance scale measured by baryon acoustic oscillations (BAO) in galaxy surveys or Type Ia supernovae, the growth of structure determined by redshift-space distortions, plus the assumption that the dark energy is a cosmological constant, yields a 68% confidence constraint on $\Omega_{\text{tot}} = 1.0002 \pm 0.0026$ [49, 50]. Results of this type are normally taken as justifying the restriction to flat cosmologies.

Currently the most accurate determination of Ω_c comes from global fits of cosmological parameters to a variety of observations. For example, using measurements of the anisotropy of the CMB, including the CMB lensing likelihood, and of the spatial distribution of galaxies, one finds a density of cold, nonbaryonic matter $\Omega_c h^2 = 0.1188 \pm 0.0010$, and the baryonic matter density, $\Omega_b h^2 = 0.02230 \pm 0.00014$ [49, 50]. Some of the key cosmological parameters of the Λ-CDM model [48–50, 54] are provided in Table 1.3.

The Λ-CDM model with spatial flatness gives an excellent fit to observations on large

Table 1.3. The current density of each mass-energy component of the Universe.

	Density
Baryonic matter	$\Omega_b = 0.02230(14)h^{-2} = 0.04860(51)$
Cold dark matter	$\Omega_c = 0.1188(10)h^{-2} = 0.2589(57)$
Presureless matter	$\Omega_m = \Omega_b + \Omega_c = 0.3089(62)$
Dark energy	$\Omega_\Lambda = 0.6911(62)$
CMB radiation	$\Omega_\gamma = 2.473 \times 10^{-5}(T/2.7255)^4 h^{-2} = 5.46(19) \times 10^{-5}$
Curvature	$\Omega_{\rm tot} = 1.0002(26)$ (68%)

scales.[1] The fact that $\Omega_{\rm tot}$ is measured to be nearly unity in the present epoch leads to the so-called flatness problem: Rewriting Eq. (1.7) in the early Universe dominated by radiation and matter as

$$1 - \Omega_{\rm tot}(t) = \frac{(1 - \Omega_{\rm tot,0})a^2(t)}{\Omega_{r,0} + a(t)\Omega_{m,0}}, \tag{1.9}$$

one finds that when the value of $\Omega_{\rm tot}$ is extrapolated backwards into the time of radiation-matter equality, the total density parameter is equal to unity with an accuracy $|1 - \Omega_{\rm tot}(t_{rm})| \leq 2 \times 10^{-4}$. If one extrapolates backward to the Planck time $t_P = \sqrt{\hbar G} \simeq 5.4 \times 10^{-44}$s, where $a(t_P) \approx 2 \times 10^{-32}$, one finds an unnaturally strong fine-tuning $|1 - \Omega_{\rm tot}(t_P)| \leq 10^{-60}$. The most convincing explanation for the flatness problem is inflationary cosmology, which postulates a period of accelerated expansion prior to the radiation-dominated era. In that hypothesis, the rapid expansion can drive $\Omega_{\rm tot}$ sufficiently close to unity, so that $|1 - \Omega_{\rm tot}|$ remains unobservable today.

Inflation also provides an explanation for the magnetic monopole problem, i.e., magnetic monopoles have never been observed thus far, even though in the early Universe, they were supposedly overproduced due to the breakdown of the gauge symmetry of the Grand Unified Theory into $SU(3)_{\rm C} \otimes SU(2)_{\rm L} \otimes U(1)_Y$.

Additionally, inflationary cosmology provides a simple mechanism for producing primordial density perturbations that are quite similar to those observed. That is, inflation generates perturbations through the amplification of quantum fluctuations, which are stretched to astrophysical scales by the rapid expansion. Density perturbations grow between the matter-dominated and curvature-dominated epochs. If the mass density con-

[1]On the smallest scales, there remains some controversy concerning the structure of dwarf galaxies and possible substructure in galaxy halos.

tributed by the luminous matter were the major contribution to the mass density of the Universe, the duration of the epoch of structure formation would be very short, thereby requiring fluctuations in the CMB which would be larger than those observed. The most attractive scenario of structure formation that is consistent with observations is inflation-produced adiabatic density perturbations with cold dark matter, which provides the primordial density inhomogeneities necessary to initiate structure formation resulting in predictable temperature fluctuations in the CMBR, as shown in Figure 1.1.

Another piece of observational evidence for the existence of dark matter involves galactic dynamics. In the 1970s, Vera Rubin and Kent Ford discovered that rotation curves of galaxies are flat, which means the circular velocities of clouds of neutral hydrogen in spiral galaxies, measured as a function of the distance from the center of the galaxy, remain constant extending as far as they have been measured [55], as illustrated in Figure 1.2 [2]. The luminous disk is distributed no further than about 5 kpc from the center of the galaxy. If the luminous matter were the only component inside each galaxy, and if stellar motions obey Newton's laws, that is $V(r) \propto \sqrt{M(r)/r}$, the rotation curve is expected to decrease as $r^{-1/2}$ outside the luminous disk. Here r denotes the distance from the center of the galaxy, $V(r)$ is the velocity of the rotational stellar motion at the distance r, and $M(r)$ is the mass contained inside the disk of radius r. Similar phenomena of flat rotation curves have been observed for all galaxies studied, including our Milky Way, which strongly suggests that this is a universal behavior.

The simplest explanation for the observed rotational curves is that galaxies contain far more mass than the baryonic matter that accounts for the bright stellar objects residing in the galactic disks. In fact, applying Newton's laws to the motion of galaxies in clusters, one finds that the mass distribution interior to r grows as $M(r) \propto r$ at large radii, which suggests the existence of dark halos around spiral galaxies extending to galactocentric radii of 200 kpc; i.e., well beyond the optical disc. This applies in particular to the Milky Way, where both dwarf galaxy satellites and globular clusters probe the outer rotation curve [56]. The recent study [57] found a discrepancy between the observed rotation curve and the expected contribution from baryons in our Milky Way, and that the evidence for a dark component rises above 5σ significance. The velocity dispersions of dwarf spheroidal galaxies imply mass-to-light ratios larger than those observed in our "local" neighborhood

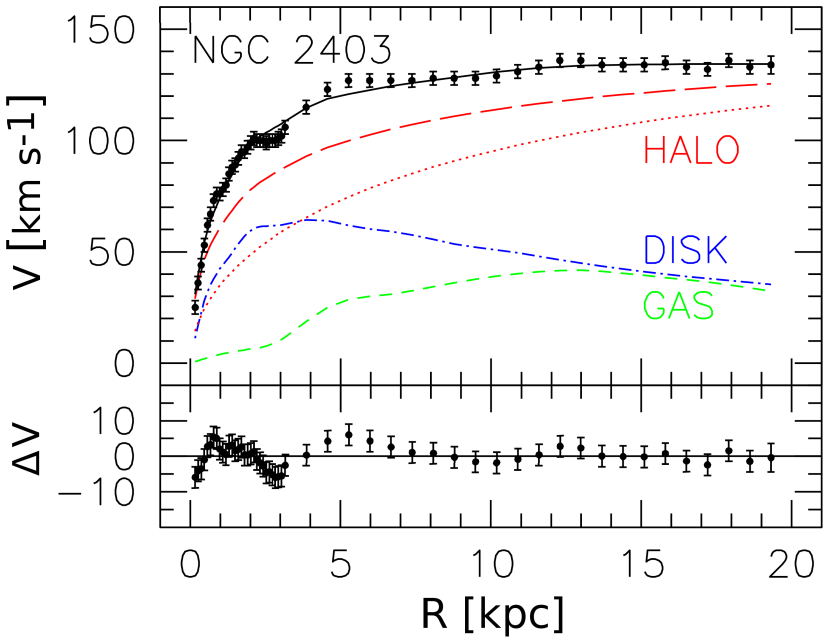

Figure 1.2. Rotation curve for the bright spiral galaxy NGC 2403 with an adiabatically contracted halo model (long-dashed line) or initial model (dotted line) [2]. The disk and gas profiles correspond to the contracted final model. The points are the measured circular rotation velocities as a function of distance from the center of the galaxy. The dashed and dotted curves are the contribution to the rotational velocity due to the observed disk and gas, respectively, and the dot-dash curve is the contribution from the dark halo. The data-fit residuals ΔV are shown in the lower part. The observed velocity data (black points) are from Ref. [3] .

and, while the profiles of individual dwarfs show scatter, strongly suggest the overall dark matter content [56]. Today, most dynamical estimates are consistent with a value $\Omega_m \sim$ 0.2-0.3 [56] on cluster scales.

The gravitational influence of DM can also be observed through distortions of an image, called "gravitational lensing." The theory of General Relativity predicts that mass bends space-time, and so it also bends the trace of light. The light from distant objects is bent towards a region of large mass when it passes by, thus, multiple images of distant objects may be seen, or, if these images cannot be individually resolved, the background object may appear brighter, as shown in Figure 1.3. Some of these images may be distorted or sheared. This effect can be used to uncloak the existence of non-luminous matter. Lensing measurements confirm the existence of enormous quantities of dark matter both in galaxies and in clusters of galaxies.

Figure 1.3. Gravitational lensing in the galaxy cluster Abell S1063 captured by the Hubble Space Telescope. The huge mass of the cluster distorts and magnifies the light from galaxies that lie far behind it due to gravitational lensing. Courtesy of NASA, ESA, and J. Lotz (STScI).

Measuring the mass of each galaxy also revealed that there must be more matter than luminous matter inside galaxies. In fact, historically, Fritz Zwicky was the first to propose the idea of dark matter's existence by the observation of the Coma Cluster [58]. In studying the Coma Cluster of galaxies, he estimated the total mass of the Coma Cluster by measuring the dispersion in the peculiar velocity of the cluster's galaxies, which correlates with the gravitational potential within the cluster. The cluster was treated as a self-gravitating system of point masses, which follows the steady-state virial theorem. Zwicky concluded that in order to keep the galaxies in the Coma Cluster from flying apart into the surrounding voids, the cluster must contain a large amount of "dunkle Materie," or dark matter. The recent observation of hot gas in the Coma Cluster, shown in Figure 1.4, also confirmed the presence of a vast reservoir of dark matter inside. X-rays in the image, which are emitted from the hot inter-cluster gas due to bremsstrahlung emission and line emission from highly ionized iron and other heavy elements, can only be explained by a large dark matter component that provides the gravitational potential well to hold the gas

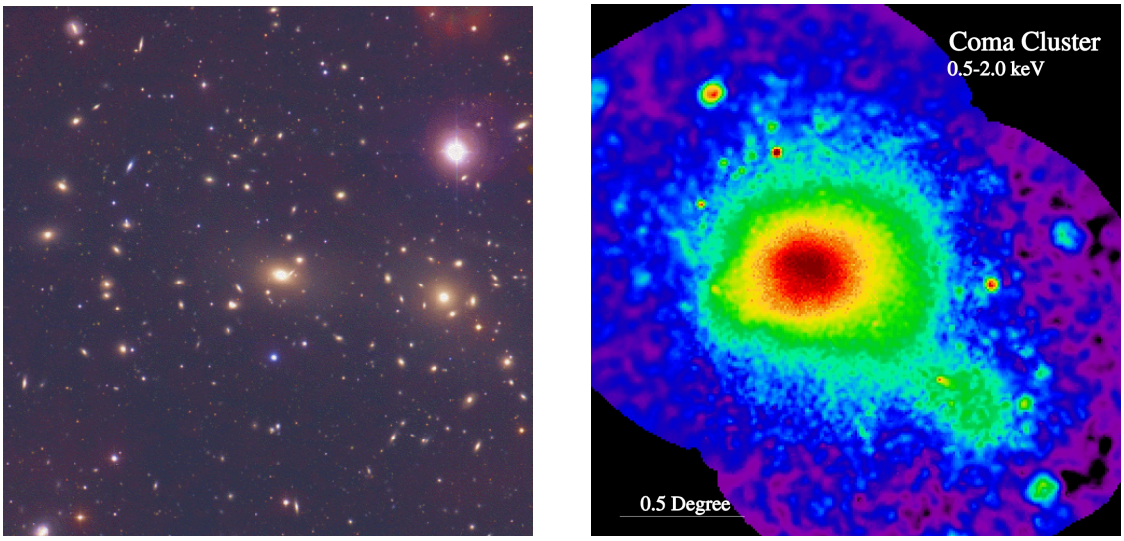

(a) Optical (b) X-ray

Figure 1.4. (a) The optical and (b) the X-ray image of the Coma Cluster (Abell 1656), containing more than 1000 galaxies. The X-ray image, observed by the ROSAT satellite, indicates the presence of hot gas. Courtesy of (a) Omar Lopez-Cruz & Ian Shelton/NOAO/AURA/NSF and (b) S. L. Snowden USRA, NASA/GSFC.

together. If there were no dark matter to anchor the gas gravitationally, the hot gas would have expanded beyond the cluster on time scales much shorter than the Hubble time.

Another particularly compelling example is the Bullet Cluster, which recently, on cosmological time scales, formed from a collision of two clusters. A recent image of the Bullet Cluster of galaxies taken by the Chandra X-ray observatory is shown in Figure 1.5. Here one can see the separation of baryonic matter, mostly consisting of hot gas (in pink), seen by X-ray emission, and dark matter (in blue), deduced from gravitational lensing. In the process of the head-to-head collision of the two clusters, the dark matter has passed through the collision point, indicating that DM self-interactions are indeed weak, while the baryonic matter in the form of the gas cloud was decelerated due to interactions and remains in the region at the center of the new cluster, whereas the galaxies in the clusters proceeded on ballistic trajectories.

1.3 WIMPs

Analyses of structure formation in the Universe indicate that most DM should have been nonrelativistic at the epoch of galaxy formation. Candidates for nonbaryonic DM must also satisfy several conditions: (i) they must be stable on cosmological time scales to

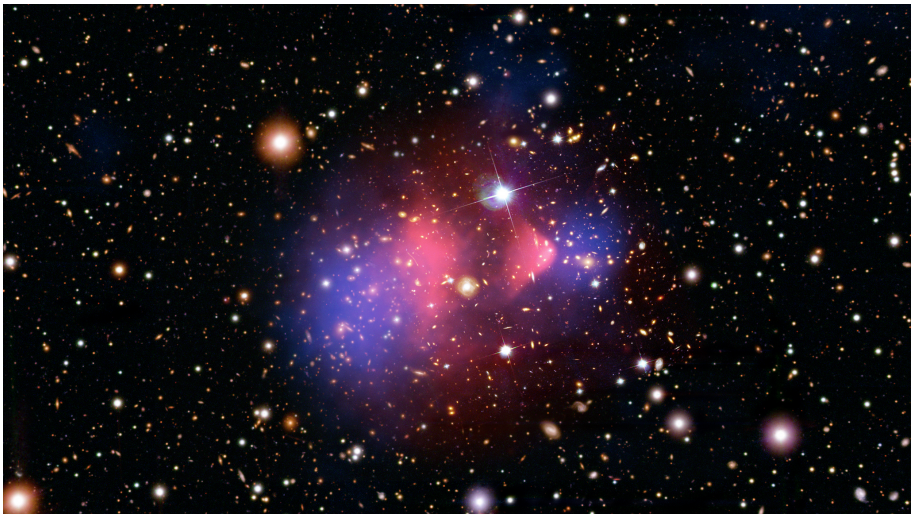

Figure 1.5. The image of the Bullet Cluster (1E 0657-56) of galaxies, in which a cluster formed out of a collision of two smaller clusters, captured by the Chandra X-ray observatory. Most of the matter in the clusters (blue) is clearly separate from the normal matter (pink), giving direct evidence that nearly all of the matter in the clusters is dark. Courtesy of NASA/CXC/CfA/ M. Markevitch *et al.* (X-ray); NASA/STScI; ESO WFI; Magellan/U. Arizona/ D. Clowe *et al.* (Lensing Map); NASA/STScI; Magellan/U. Arizona/D. Clowe *et al.* (Optical).

realize the observed growth of density perturbations; (ii) they must have very weak interactions with the SM sector to be consistent with observations of structure formation and the absence of electromagnetic radiation emission and absorption; and (iii) they must have the right relic density to explain the CMB anisotropies and the observations of galaxies and cluster distributions. Weakly interacting massive particles (WIMPs) are particles with mass roughly between a few GeV and a few TeV, and with a self-annihilation cross section of approximately weak strength. Within standard cosmology, their present relic density can be calculated by assuming that the WIMPs were in thermal and chemical equilibrium with the plasma of SM particles after inflation. In such conditions, their density would become Boltzmann-suppressed, $\sim \exp(-m_\chi/T)$ at $T < m_\chi$, and therefore drop out of thermal equilibrium (dubbed as "freeze out") once the rate of DM pair annihilation into SM particles (or vice versa) becomes smaller than the Hubble expansion rate of the Universe. After freeze out, the comoving WIMP density remains essentially constant; if the Universe evolved adiabatically after WIMP decoupling, this implies a constant WIMP number to entropy density ratio. Their present relic density is then approximately given by [59]

$$\Omega_c h^2 \simeq \text{const.} \times \frac{T_0^3}{m_{\text{Planck}}^3 \langle \sigma_A v \rangle} \simeq \frac{0.1\text{pb} \cdot c}{\langle \sigma_A v \rangle}, \tag{1.10}$$

where T_0 is the current CMB temperature, m_{Planck} is the Planck mass, c is the speed of light, and $\langle \sigma_A v \rangle$ is the thermally averaged total WIMP pair annihilation cross section into SM particles times the relative velocity of WIMPs in their center of mass system. WIMPs are expected to have a cross section $\langle \sigma_A v \rangle$ near the typical size of weak interaction cross sections. In that case, where $\langle \sigma_A v \rangle \approx 1\text{pb} \cdot c = 3 \times 10^{-26}\text{cm}^3\,\text{s}^{-1}$, the standard thermal freeze-out mechanism yields the qualitatively correct relic density, $\Omega_c h^2 \approx 0.1$ [8, 59–63]. Although this is not a necessary condition, this remarkable coincidence, dubbed the "WIMP miracle," has drawn huge attention over the years.

1.4 Detection strategies for WIMPs

If most CDM consists of WIMPs, they should be gravitationally trapped inside galaxies and should be adequately distributed to account for the observed rotational curves. WIMPs can be slowed down, captured, and trapped in celestial objects like the Earth or the Sun, or more massive objects such as neutron stars, thus enhancing their density and their probability of annihilation. These conditions determine the main features of experimental detection of WIMPs; i.e., probing the interactions of WIMPs with ordinary matter, known as direct detection, and examining the annihilation products of WIMPs, known as indirect detection. WIMPs could also be directly produced at particle colliders. Since DM interacts weakly with ordinary matter, it, if produced, will escape collider detectors. One possible signature is a single final-state object recoiling against missing (transverse) energy. Another method of detecting dark matter is by measuring its gravitational effect on luminous matter. The observations of the motions of stars within galaxies and of galaxies within clusters, as well as the studies of cosmic history, indicate that there is a significant amount of dark matter in the Universe.

1.4.1 Direct detection

WIMPs are expected to interact with ordinary matter through elastic scattering on nuclei. For WIMP masses in the range of 10 GeV to 10 TeV, typical nuclear recoil energies, E_R, are of the order of 1 to 100 keV. The expected interaction rates depend on the local WIMP flux and the interaction cross section. The differential scattering rate per detector and per

target nucleus averaged over the galactic WIMP velocity distribution can be calculated as

$$\frac{dR}{dE_R} = N_T \left(\frac{\rho_\odot}{m_\chi}\right) \int_{v>v_{\min}} \frac{d\sigma(v, E_R)}{dE_R} v f_E(\mathbf{v}) d^3v, \tag{1.11}$$

where N_T is the number of target nuclei in the detector, $f_E(\mathbf{v})$ is the velocity distribution of WIMPs, usually taken to be Maxwellian with $v_{\text{rms}} = 155$ km s^{-1}, and

$$v_{\min} = \frac{1}{\mu_T}\sqrt{\frac{m_T E_R}{2}}, \tag{1.12}$$

where m_T is the target nuclei mass, and $\mu_T = (1/m_T + 1/m_\chi)^{-1}$, is the reduced mass of the target nuclei and the WIMP. The DM density in the "neighborhood" of our solar system was first estimated as early as 1922 by J. H. Jeans, who analyzed the motion of nearby stars transverse to the galactic plane [56]. He concluded that in our galactic neighborhood, the average density of DM must be roughly equal to that of luminous matter (stars, gas, dust). Remarkably enough, the recent estimate [64] finds a quite similar result for the smooth component of the local DM density, $\rho_\odot$, at the location of the Sun, $r_\odot = 8.33$ kpc:

$$\rho_\odot = (0.39 \pm 0.03) \cdot (1.2 \pm 0.2) \cdot (1 \pm \delta_{\text{triax}})\,\text{GeV/cm}^3. \tag{1.13}$$

The first term on the right-hand side gives the average DM density at a point one solar distance from the center of our Galaxy. This has been derived by fitting a complete model of our galaxy to a host of data, including the galactic rotation curve. The second factor accounts for the fact that the baryons in the galactic disk, in which the solar system is located, also increase the local DM density [65]. The third factor corrects for possible deviations from a purely spherical halo, with $\delta_{\text{triax}} \leq 0.2$ [66]. There is, however, a large systematic uncertainty in the Milky Way dark matter halo density profile (see for example Ref. [67–69]).

The mean WIMP velocity is approximately 220 km s^{-1} [64] at the location of our solar system, and the galactic escape velocity is approximately 544 km s^{-1}. The WIMP velocity distribution is usually assumed to follow a Maxwell-Boltzmann distribution in the galactic rest frame, shifted into the Earth rest frame. The cross section, $\sigma(v, E_R)$, depends on the nature of the interaction between DM and target nuclei. For nonrelativistic Majorana WIMPs, it includes spin-independent (SI), spin-dependent (SD), anapole, pseudo-scalar-mediated, and $\mathbf{L} \cdot \mathbf{S}$ scattering [70]. SI interactions involve scalar currents, while SD interactions

involve axial vector currents, the latter existing only if DM carries spin. Due to coherence effects, the SI cross-section scales approximately as the square of the size of the nucleus, therefore, heavy nuclei such as Xe are often favored, whereas for SD interactions, the cross section depends on the nuclear spin factor, and target nuclei often used include ^{19}F, ^{73}Ge, ^{127}I, ^{129}Xe, and ^{131}Xe.

At low WIMP mass, the sensitivity of detectors drops due to the detector recoil energy threshold, whereas at high mass, the sensitivity also decreases due to the decrease of the WIMP flux as $1/m_\chi$ for a fixed mass density. The sensitivity is best if the WIMP mass is near that of the recoiling nucleus.

The effect of the motion of the detecter frame with respect to the Galactic frame, $\mathbf{v}_{\rm obs}(t)$, is also of interest. Taking into account the motion of the Local Standard of Rest (LSR), namely the rotation of the Sun around the Galactic Center (GC), $\mathbf{v}_{\rm LSR}$, the peculiar solar motion, $v_\odot$, and the motion of the Earth around the Sun, $\mathbf{V}_\oplus$, one finds

$$\mathbf{v}_{\rm obs}(t) = \mathbf{v}_{\rm LSR}(t) + v_\odot(t) + \mathbf{V}_\oplus(t). \tag{1.14}$$

Within Galactic coordinates where $\hat{\mathbf{x}}$ is the direction to the GC, $\hat{\mathbf{y}}$ the direction of disk rotation, and $\hat{\mathbf{z}}$ the North Galactic Pole, $\mathbf{v}_{\rm LSR} = (0, \Theta_0, 0)$ and $v_\odot \simeq (11.10, 12.24, 7.25)$ km s^{-1} [71], where $\Theta_0 \approx 220$ km s^{-1} is the typical mean WIMP velocity. Neglecting the ellipticity of the Earth's orbit, the motion of the Earth around the Sun is,

$$\mathbf{V}_\oplus(t) = V_\oplus[\hat{\epsilon}_1 \cos\omega(t - t_1) + \hat{\epsilon}_2 \sin\omega(t - t_1)], \tag{1.15}$$

where $V_\oplus = 29.8$ km s^{-1} and $t_1 = 0.218$ is the fraction of the year before the Spring equinox, while $\hat{\epsilon}_1$ and $\hat{\epsilon}_2$ are the directions of the Earth's velocity at times t_1 and $t_1 + 0.25$ years [64]. Because of the motion of the Earth through the DM halo, an annual modulation is predicted for WIMP signals [72]. The DAMA collaboration has reported results from a total of 7 years exposure with the LIBRA phase involving 250 kg of target nuclei plus the earlier 6 years exposure of the original DAMA/NaI experiment with 100 kg of target nuclei [73, 74]. They observe an annual modulation of the signal in the 2 to 6 keVee (keV electron equivalent) bin, with the period of 1 year and phase with maximum around June 2nd, as expected, at the 9.3σ level. If interpreted within the standard halo model, two cases are compatible: (i) a WIMP with $m_\chi \simeq 50\,$GeV and $\sigma_{\chi p} \simeq 7 \times 10^{-6}$ pb; or (ii) $m_\chi \simeq$

6-10 GeV range with $\sigma_{\chi p} \sim 10^{-3}$ pb. Many other experiments, however, exclude both the high and low mass DAMA/LIBRA scenarios. Both Germanium and Xenon detectors now exclude the DAMA/LIBRA signal by a large margin under standard assumptions [4].

Figure 1.6 summarizes all recent results, under standard assumptions, illustrating the limits and positive claims for WIMP scattering cross sections [4], normalized to scattering on a single nucleon, for SI couplings, as functions of WIMP mass. It also includes the neutrino background projection for coherent neutrino-nucleus scattering, and a typical expectation for a supersymmetric model after the LHC Run 1 results [6, 7]. Currently many experiments exclude both the high and low mass DAMA/LIBRA solutions. As of February 2017, the most stringent limit on the SI cross section is provided by LUX, a 370 kg double phase Xenon detector, which is currently leading the field for masses above 20 GeV, setting a limit of 7.6×10^{-10} pb for a WIMP mass of 33 GeV [75]. LUX also provides the best limit for SD WIMPs with pure neutron couplings at all masses [76]. A 300-live-day run is in progress, allowing an expected improvement in sensitivity by a factor of 5. XENON1T, the successor to XENON100 is planning to take data soon, and it is expected to overtake LUX in the coming year, if the backgrounds are kept within specifications. LUX-ZEPLIN is expected to have sensitivity reaching about 10^{-12} pb for a WIMP mass of 500 GeV [77].

1.4.2 Indirect detection

As in the early Universe, ongoing WIMP annihilation is expected at the current epoch, and the stable annihilation products may be detected; these include neutrinos, gamma rays, positrons, antiprotons, and antinuclei. These methods are complementary to direct detection and might make it possible to explore higher masses and different coupling scenarios. "Smoking gun" signals for indirect detection are: (i) GeV neutrinos coming from the center of the Sun or Earth, since such high energy neutrinos cannot be produced by nuclear reactions; and (ii) mono-energetic photons of $\sim$ GeV scale from WIMP annihilation in space, for no astrophysical background events can produce such high energy mono-energetic γ-rays. Both types of signals are also easy to trace back their sources of production, as they propagate along straight paths through matter.

Upward-going muons from WIMP annihilation can be detected in large neutrino telescopes such as SuperKamiokande (SuperK) and IceCube. The best upper limit for WIMPs

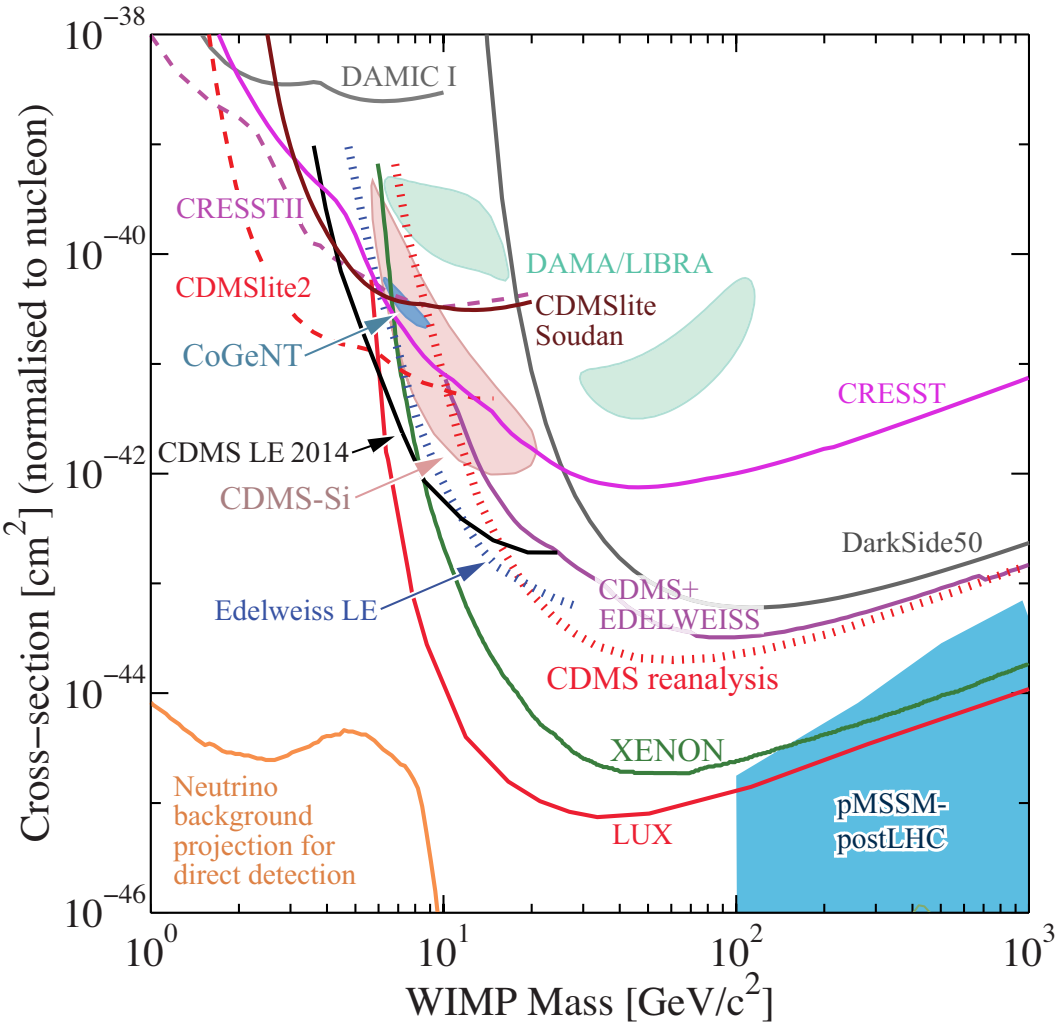

Figure 1.6. WIMP cross sections (normalized to a single nucleon) for SI coupling versus mass [4, 5]. The DAMA/LIBRA, CDMS-Si and CoGeNT enclosed areas are regions of interest from possible signal events. For context, the blue shaded region shows a scan of the parameter space of the pMSSM, a version of the MSSM with 19 parameters, by the ATLAS collaboration [6, 7], which integrates constraints set by LUX and ATLAS Run 1; the favored region is around 10^{-10} pb and 500 GeV.

with mass below 200 GeV that produce muons in the final state comes from SuperK. For WIMPs annihilating into $b\bar{b}$ pairs, the resulting upper limit on the SD scattering cross section on protons is about 1.5 (2.3) fb for $m_\chi = 10$ (50) GeV; for WIMPs annihilating exclusively into $\tau^+\tau^-$ pairs, the bounds are about one order of magnitude stronger [78].

Detection of the photon flux from DM annihilations is of particular interest. The differential flux of photons from a given angular direction produced by the annihilation of Majorana DM is

$$\frac{d\Phi(E_\gamma)}{dE_\gamma} = \frac{1}{2}\frac{r_\odot}{4\pi}\left(\frac{\rho_\odot}{m_\chi}\right)^2 \int_{\Delta\Omega} d\Omega \sum_f \int_{\text{l.o.s}} \frac{ds}{r_\odot}\left(\frac{\rho(r(s,\theta))}{\rho_\odot}\right)^2 \langle\sigma v\rangle_f \frac{dN_\gamma^f}{dE_\gamma}, \tag{1.16}$$

where dN_γ^f/dE_γ is the energy spectrum of photons produced per one annihilation in the channel with final state f, integrated over a given angular range $\Delta\Omega$, and along the line of sight (l.o.s) denoted as s. The functional forms of a DM halo profile, based on numerical N-body simulations of large-scale structure formation, $\rho(r)$, have been proposed by various astrophysicists. One of the standard forms, proposed by Navarro, Frenk, and White (NFW) [79] is

$$\rho_{\text{NFW}}(r) = \rho_s \frac{r_s}{r}\left(1 + \frac{r}{r_s}\right)^{-2}, \tag{1.17}$$

where r is the radial distance from the Galactic Center (GC), $r_s = 24.42$ kpc is a typical scale radius, and $\rho_s = 0.184$ GeV cm^{-3} is a typical scale density, both of which are determined from dynamical constraints. Although the determination of the NFW profile makes use of numerical simulation without baryons, whose role is not negligible in the inner Galaxy, it has been found to explain the observed rotation curves well [57].

WIMP annihilation in the halo can give rise to a continuous spectrum of gamma-rays and, at the one-loop level, also to mono-energetic photons from the $\gamma\gamma$ and γZ channels. These channels allow one to search for WIMPs for which direct detection experiments have little sensitivity. The size of this signal depends strongly on the halo model, but is expected to be most prominent near the Galactic Center, as can be seen in Eqs. (1.16) and (1.17). The central region of our Galaxy hosts a strong TeV point source discovered [80, 81] by the H.E.S.S. Cherenkov telescope. Moreover, Fermi Large Area Telescope (LAT) data revealed a new extended source of GeV photons near the Galactic Center above and below the galactic plane, the so-called "Fermi bubbles" [82], as well as several dozen point sources of GeV photons in the inner kpc of our Galaxy [83]. These sources are, however, very likely of astrophysical origin. The presence of these unexpected backgrounds makes it more difficult to discover WIMPs in this channel.

Analyses of Fermi-LAT data also find an excess of events in the few GeV range from an extended region around the center of our Galaxy, consistent with several WIMP interpretations [15, 84]. A recent analysis by the Fermi-LAT collaboration [83] found evidence for emission of GeV photons from the inner few degrees around the GC not accounted for by their modeling of astrophysical sources. The spectrum and the morphology are

compatible with those expected from annihilating DM particles. In particular, they are best fit by 30-50 GeV DM particles annihilating into $\bar{b}b$ with $\langle \sigma_A v \rangle \approx 7 \times 10^{-27}$ cm^3 s^{-1} [85]. However, the size and spectrum of the fitted "excess" depends strongly on the details of the fits, and most photons detected from directions around the GC actually originate from astrophysical foregrounds, which are not precisely understood. As the collaboration concludes, "a precise physical interpretation of its origin is premature."

As of February 2017, the best bound on WIMP annihilation into photons in the current Universe comes from a combination of Fermi-LAT observations of dwarf galaxies [8]. It excludes WIMPs annihilating either hadronically or into $\tau^+\tau^-$ pairs with the canonical cross section, needed for thermal relics, if the WIMP mass is below $\sim 100\,\mathrm{GeV}$. Current best limits on DM annihilation from Milky Way dwarf spheroidal galaxies from six years of Fermi-LAT data [8] are shown in Figure 1.7, which compares constraints on the DM annihilation cross section for the $\tau^+\tau^-$ channel from Ref. [8] with previously published constraints from the LAT analysis of the Milky Way halo (3σ limit) [9], 112 h of observations of the Galactic Center with H.E.S.S. [10], and 157.9 h of observations of Segue 1 with MAGIC [11]. Closed contours and the marker with error bars show the best-fit cross section and mass from several interpretations of the Galactic Center excess [12–15]. To summarize, Fermi-LAT data provides limits that exclude the thermal relic annihilation cross section for WIMPs with $m_\chi \lesssim 100$ GeV annihilating to quark and τ-lepton final states.

Antiparticles arise as additional WIMP annihilation products in the halo. The best measurements of the antiproton flux come from the PAMELA satellite and the BESS Polar balloon mission. These data exclude WIMP models that annihilate dominantly into $W^\pm$ or Z boson pairs; however, largely due to systematic uncertainties; e.g., DM halo model and electric and magnetic fields within and outside our Galaxy, they do not significantly constrain conventional WIMP models.

The best measurements of the $e^\pm$ flux at energies of tens to hundreds of GeV come from AMS-02 [86, 87] and PAMELA [88], showing a rise of the positron fraction between 10 and 200 GeV; the AMS-02 data are compatible with a flattening of the positron fraction at the highest energies. These observations can in principle be explained through WIMP annihilation. However, this requires cross sections well above that indicated by $\langle \sigma_A v \rangle$

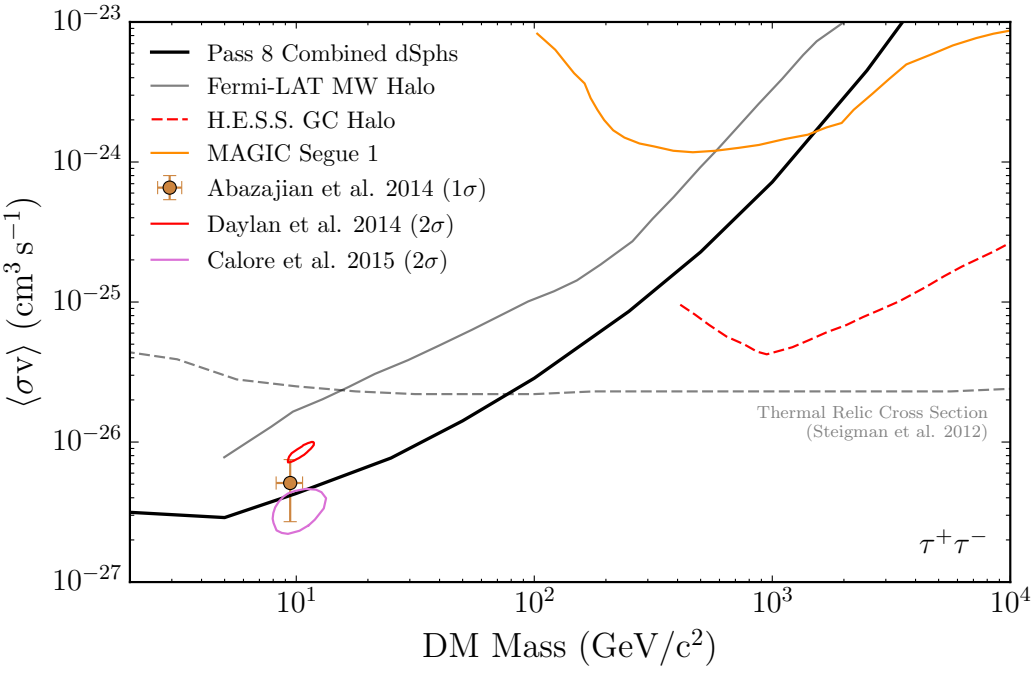

Figure 1.7. Comparison of constraints on the DM annihilation cross section for $\tau^+\tau^-$ channels [8] with previously published constraints from LAT analysis of the Milky Way halo (3σ limit) [9], 112 h of observations of the GC with H.E.S.S. [10], and 157.9 h of observations of Segue 1 with MAGIC [11]. Closed contours and the marker with error bars show the best-fit cross section and mass from several interpretations of the GC excess [12–15].

in Eq. (1.10) for a thermal WIMP. Most of the models that resolve this tension have now been excluded by the stringent bounds from Fermi-LAT and from analyses of the CMB. In contrast, viable astrophysical explanations for the excess, which include introducing new primary sources of electrons and positrons; e.g., pulsars [89, 90] or a nearby supernova that exploded about two million years ago [91], have also been suggested.

The high quality of the AMS-02 data on the positron fraction, which does not show any marked features, also allows one to impose stringent bounds on WIMPs with mass below 300 GeV annihilating directly into leptons [16]. Figure 1.8 shows the upper limits (95% CL) on the DM annihilation cross section, as derived from the AMS positron fraction, for various final states [16], WMAP7 (for $\ell^+\ell^-$) [17–22] and Fermi-LAT dwarf spheroidals (for $\mu^+\mu^-$ and $\tau^+\tau^-$) [23]. The dotted portions of the curves are potentially affected by solar modulation. $\langle\sigma_A v\rangle_{\text{therm}} = 3 \times 10^{-26}$ cm^3 s^{-1} is indicated by the gray horizontal line. The AMS limits are shown for reasonable reference values of the local DM density and energy

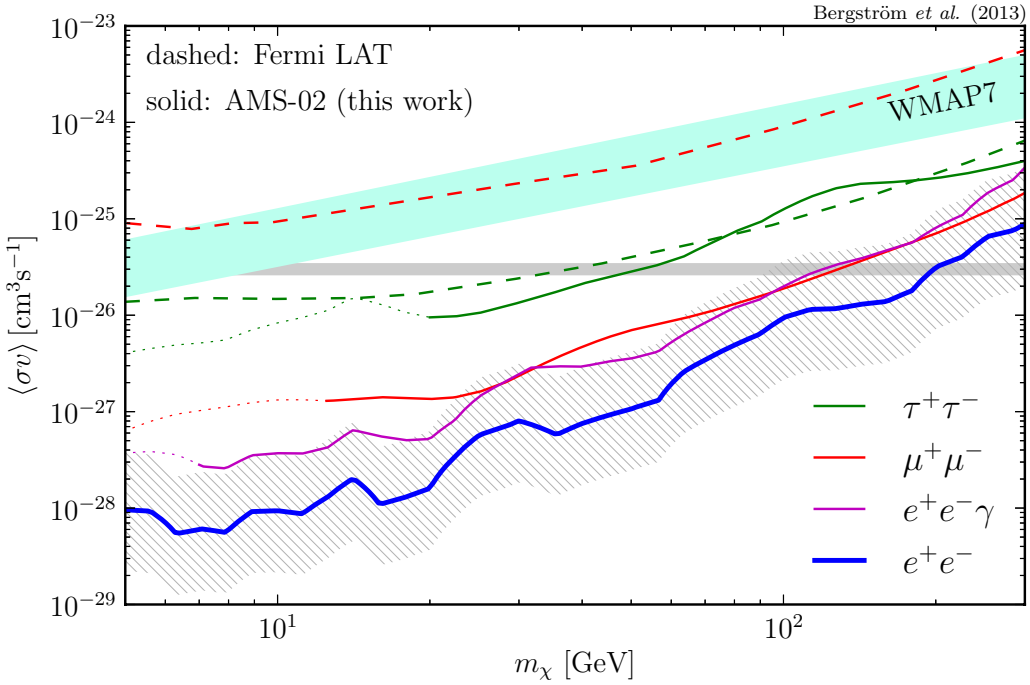

Figure 1.8. The upper limits (95% CL) on the DM annihilation cross section [16], as derived from the AMS positron fraction, for various final states [16], WMAP7 (for $\ell^+\ell^-$) [17–22] and Fermi-LAT dwarf spheroidals (for $\mu^+\mu^-$ and $\tau^+\tau^-$) [23]. The dotted portions of the curves are potentially affected by solar modulation. $\langle\sigma_A v\rangle_{\text{therm}} = 3 \times 10^{-26}$ cm^3 s^{-1} is indicated by the gray horizontal line. The AMS limits are shown for reasonable reference values of the local DM density and energy loss rate, and can vary by a factor of a few, as indicated by the hatched band (for clarity, this band is only shown around the e^+e^- constraint).

loss rate, and can vary by a factor of a few, as indicated by the hatched band (for clarity, this band is only shown around the e^+e^- constraint, but it applies to each annihilation channel). The AMS data significantly limit light DM models with $m_\chi \sim \mathcal{O}(10)$ GeV, particularly annihilating into e^+e^- and $\mu^+\mu^-$ with thermal relic cross sections.

1.4.3 Collider searches

The interaction between DM and SM particles can also be investigated at collider experiments by directly producing DM particles. The minimal experimental signature of DM production at a hadron collider consists of an excess of events with a single final-state object X recoiling against large amounts of missing transverse energy $\not{E}_T$. A variety of such "mono-X" signatures involving jets of hadrons, gauge bosons, top and bottom quarks, as well as the Higgs boson in the final state, has been examined in LHC Run 1 and 2, as well

as a second class of $\not{E}_T$ signatures that arises from the production of "partner" particles that decay to DM and SM particles [92–94].

In order to interpret the cross section limits obtained from the LHC and the Tevatron $\not{E}_T$ searches, and to relate these bounds to the constraints derived from direct and indirect detection, one needs a theory of DM. Effective field theory (EFT) allows one to describe the DM-SM interactions mediated by all kinematically inaccessible particles in a universal way [95–97]. The DM-EFT approach allows one to derive stringent bounds on the scale of new physics, Λ, that suppresses the higher-dimensional operators. Currently, LHC experiments have stronger bounds on operators leading to spin-dependent scattering than direct detection experiments, while direct detection probes are more constraining for spin-independent scattering for WIMP masses above a few GeV [92]. Similarly the Tevatron provides the current best limit, particularly for light dark matter, below 5 GeV, and for spin dependent interactions [97].

EFTs, however, cannot describe correctly the full kinematics of DM production at the LHC at high energy. To capture some set of signals accurately at LHC energies at Run 2 and beyond, one needs complete DM models that resolve the EFT contact interactions into single particle s-channel or t-channel exchanges [98].

1.5 The supersymmetric Standard Model

The cosmological arguments stated above imply that evidence for dark matter is compelling in dwarfs, spiral galaxies, and galaxy clusters, as well as at cosmological scales. However, this is at odds with the description of Nature by the SM of particle physics. For instance, neutrino species are stable and interact with baryonic matter weakly, but they are, even if assumed to have finite mass, too light to account for CDM, and therefore give rise to a considerably different primordial fluctuation spectrum. The Higgs and Z^0 boson are both neutral and interact with (light) baryonic matter weakly. They are, however, short-lived to be candidates for CDM. For these reasons, extension of the SM has been pursued in a variety of ways. It has been found that the Minimal Supersymmetric Standard Model (MSSM), which is one of these extensions, naturally accommodates neutral, weakly interacting, massive and stable particles. This model has been studied extensively since first proposed circa 1970 [99]. In the following section, I will first introduce a new type of symmetry

called "supersymmetry" and explain how the models that feature this symmetry are free from quadratic divergences. Then we will see that the MSSM provides particles that are suitable WIMPs, called "neutralinos" [63]. Finally I will discuss the phenomenology of DM within this framework.

1.5.1 Supersymmetry and the hierarchy problem

Supersymmetry (SUSY) relates particles differing by $1/2$ unit of spin; e.g., spin-0 scalars and spin-$1/2$ fermions or spin-$1/2$ fermions and spin-1 vector bosons (see for example Ref. [24, 63, 100]). The particles and their *superpartners* are contained in *supermultiplets*, and the particles in the same supermultiplets must share the same mass[2] and the same gauge quantum numbers, meaning that the SUSY extension of the SM leads to roughly twice as many particle species as in the SM alone. Obviously SUSY is not exactly preserved in Nature; as of today, no scalar particle has been discovered with the same mass and quantum numbers as, for example, the electron. In fact, there are no candidates for supersymmetric scalar partners for any of the SM fermions in the experimentally observed spectrum. We will discuss the patterns of SUSY breaking allowed in realistic SUSY gauge theories in Sec. 1.5.4. As already mentioned, the MSSM provides good candidates for CDM. Another pleasant feature of the MSSM is that it suggests the unification of the fundamental forces at a high-energy scale.

A SUSY transformation turns a bosonic state into a fermionic state, and vice versa. There are two types of supermultiplets relevant for our purposes of constructing realistic models, *chiral supermultiplets* and *gauge supermultiplets*. Chiral supermultiplets, $\Phi \supset (\phi, \psi, \mathcal{F})$, consist of a complex scalar field, ϕ, a 2-component Weyl fermion field, ψ, and an *auxiliary field*, $\mathcal{F}$.[3] The free Lagrangian is given by

$$\mathcal{L}_{\text{free}} = -\partial^\mu \phi^* \partial_\mu \phi + i\psi^\dagger \bar{\sigma}^\mu \partial_\mu \psi + \mathcal{F}^* \mathcal{F}, \tag{1.18}$$

where $\bar{\sigma}^0 = \sigma^0 = \mathbf{1}$ is the 2×2 identity matrix and $\bar{\sigma}^i = -\sigma^i$ for $i = 1, 2, 3$ denote the Pauli matrices. $\mathcal{L}_{\text{free}}$ is invariant under the SUSY transformations

[2] The gauge coupling of the SUSY particle to the Higgs field causes the mass splitting with its superpartner when EW symmetry is broken.

[3] The auxiliary fields $\mathcal{F}$ and $\mathcal{D}^a$ appear in the Lagrangian with no kinetic energy term, thus they have no physical contribution. They are introduced to make the Lagrangian consistent when the fields are off-shell and to make the SUSY gauge transformation linear.

$$\begin{aligned}\delta\phi &= \epsilon\psi,\\ \delta\psi_\alpha &= -i(\sigma^\mu\epsilon^\dagger)_\alpha\partial_\mu\phi + \epsilon_\alpha\mathcal{F},\\ \delta\mathcal{F} &= -i\epsilon^\dagger\bar{\sigma}^\mu\partial_\mu\psi.\end{aligned} \tag{1.19}$$

Gauge supermultiplets, $\Phi \supset (\lambda^a, A^a_\mu, \mathcal{D}^a)$, consist of a massless gauge field with field strength $F^a_{\mu\nu} = \partial_\mu A^a_\nu - \partial_\nu A^a_\mu + g f^{abc} A^b_\mu A^c_\nu$, a 2-component Majorana fermion field, λ^a , and a real auxiliary field, $\mathcal{D}^a$. The Lagrangian is of the form,

$$\mathcal{L}_{\text{gauge}} = -\frac{1}{4}F^a_{\mu\nu}F^{a\mu\nu} + i\lambda^{\dagger a}\bar{\sigma}^\mu D_\mu\lambda^a + \frac{1}{2}\mathcal{D}^a\mathcal{D}^a, \tag{1.20}$$

where $D_\mu\lambda^a = \partial_\mu\lambda^a + g f^{abc}A^b_\mu\lambda^c$. $\mathcal{L}_{\text{gauge}}$ is invariant under the SUSY transformations,

$$\begin{aligned}\delta\lambda^a_\alpha &= \frac{i}{2\sqrt{2}}(\sigma^\mu\bar{\sigma}^\nu\epsilon)_\alpha F^a_{\mu\nu} + \frac{1}{\sqrt{2}}\epsilon_\alpha\mathcal{D}^a,\\ \delta A^a_\mu &= -\frac{1}{\sqrt{2}}\left(\epsilon^\dagger\bar{\sigma}_\mu\lambda^a + \lambda^{\dagger a}\bar{\sigma}_\mu\epsilon\right),\\ \delta\mathcal{D}^a &= \frac{i}{\sqrt{2}}\left(-\epsilon^\dagger\bar{\sigma}^\mu D_\mu\lambda^a + D_\mu\lambda^{\dagger a}\bar{\sigma}^\mu\epsilon\right).\end{aligned} \tag{1.21}$$

As discussed previously, supersymmetric gauge theories address the fine-tuning problem for the fundamental scalar particle by providing cancelations of the quadratic divergences at all orders. The MSSM predicts the lightest Higgs mass to be of the same order as m_Z at tree level, and $m_h^{\text{MSSM}} \lesssim 135$ GeV [101] when radiative corrections are included.

Although, in reality, the Higgs mass receives quantum corrections from the virtual effects of every particle that couples to the Higgs field, including via Yukawa and gauge couplings and self interactions, the most dominant contribution comes from the Higgs-top quark interaction due to the large Yukawa coupling ($y_t \simeq m_t/174(\,\text{GeV}) \simeq 1$). It is therefore sufficient to consider the effect of Higgs-fermion interactions for our present purpose. To see how the cancelation of quadratic divergences occurs, consider a simplified model with a real scalar boson, h, and a Dirac fermion, f, with no gauge interactions. When electroweak symmetry is spontaneously broken, Eqs. (1.4), (1.5) and (1.6) become

$$\begin{aligned}\mathcal{L}_f &= \bar{f}(i\partial\!\!\!/ - m_f)f + (\partial_\mu h)(\partial^\mu h) - \frac{y_f}{\sqrt{2}}h\bar{f}f - V(h),\\ V(h) &= \frac{1}{2}m_h^2h^2 + \frac{m_h^2}{2v}h^3 + \frac{m_h^2}{8v^2}h^4,\end{aligned} \tag{1.22}$$

where $\not{\partial} = \partial_\mu \gamma^\mu$ and γ^μ for $\mu = 0, 1, 2, 3$ are the Dirac matrices. Here $\phi^0 = (v + h)e^{i\eta}/\sqrt{2}$ and $v/\sqrt{2} \simeq 174$ GeV. A correction to m_h^2 from a loop containing a Dirac fermion f with mass m_f and with number of color charges n_c is

$$\Delta m_h^2 = -\frac{|y_f|^2}{8\pi^2} n_c \left[\Lambda_{\rm UV}^2 + (m_h^2 - 6m_f^2) \ln\left(\frac{\Lambda_{\rm UV}}{m_f}\right) + \cdots \right], \tag{1.23}$$

which shows that if $\Lambda_{\rm UV}$ is taken of order $m_{\rm Planck}$, then the Higgs mass receives enormous corrections, approximately 10^{15} times larger than its required value. This is known as the "hierarchy problem." Although the SM fermion and gauge boson masses do not have direct quadratic sensitivity to $\Lambda_{\rm UV}$, some of them obtain masses from the Higgs field. Therefore, the mass spectrum of all the SM particles is directly or indirectly sensitive to the cutoff scale.

Next, consider the effect of the superpartners of a Dirac fermion f, the two massive complex scalar particles $\tilde{f}_i$ with mass $m_{\tilde{f}_i}$, which couple to the Higgs field with a Lagrangian term $-\lambda_{\tilde{f}_i} |\phi^0|^2 |\tilde{f}_i|^2$ and which carry the same $SU(3)_{\rm C}$ gauge quantum number as f. Then the full Lagrangian density is given as,

$$\mathcal{L}' = \mathcal{L}_f + \sum_{i=1,2} \left(|\partial_\mu \tilde{f}_i|^2 - m_{\tilde{f}}^2 |\tilde{f}_i|^2 + \lambda_{\tilde{f}} v h |\tilde{f}_i|^2 + \frac{\lambda_{\tilde{f}}}{2} h^2 |\tilde{f}_i|^2 \right). \tag{1.24}$$

A radiative correction to the Higgs mass from the scalar quartic term is then

$$\Delta m_h^2 = \frac{\lambda_{\tilde{f}}}{16\pi^2} n_c \left[2\Lambda_{\rm UV}^2 - 2 \sum_{i=1,2} m_{\tilde{f}_i}^2 \ln\left(\frac{\Lambda_{\rm UV}}{m_{\tilde{f}_i}}\right) + \cdots \right]. \tag{1.25}$$

Adding one-loop corrections from a Dirac fermion and two complex scalars together, we find

$$\Delta m_h^2 = \frac{n_c}{8\pi^2} (\lambda_{\tilde{f}} - |y_f|^2) \Lambda_{\rm UV}^2 + \cdots. \tag{1.26}$$

This cancelation of the quadratic divergence requires that the associated dimensionless couplings should be related as $\lambda_{\tilde{f}_i} = |y_f|^2$. It has been found that this cancelation takes place to all orders in perturbation theory as stated in the perturbative non-renormalization theorems [102]. We will see later that the condition imposed on the dimensionless couplings actually holds true even when SUSY is not exactly conserved. We can see from Eq. (1.24) that there is also a scalar cubic term, which contributes logarithmically to the

correction of the Higgs mass. With these effects included, the one-loop correction turns out to be

$$\Delta m_h^2 = \frac{|y_f|^2}{8\pi^2}\left[2m_f^2 \ln\left(\frac{\Lambda_{\rm UV}}{m_f}\right) - \sum_{i=1,2} m_{\tilde{f}_i}^2 \ln\left(\frac{\Lambda_{\rm UV}}{m_{\tilde{f}_i}}\right) + \cdots\right]. \tag{1.27}$$

If there is no gauge interaction and SUSY is exactly conserved, $m_{\tilde{f}_i} = \sqrt{\lambda_{\tilde{f}} v^2/2} = y_f v/\sqrt{2} = m_f$, which leads to the vanishing of the logarithmicly divergent part as well. In realistic models, however, there are mass splittings between particles and their superpartners because supersymmetry is "softly" broken, so the quantum correction is

$$\Delta m_h^2 \sim m_{\rm soft}^2 \left[\frac{\lambda}{16\pi^2} \ln\left(\frac{\Lambda_{\rm UV}}{m_{\rm soft}^2}\right) + \cdots\right], \tag{1.28}$$

where $m_{\rm soft}$ is the characteristic mass difference between a SM particle and its superpartner, and λ is the characteristic coupling constant with the Higgs field. This relation implies that the masses of SUSY particles, especially the superpartners of the top and bottom quarks and W and B bosons, which give large contributions to the Higgs mass corrections, cannot be too huge; otherwise we would lose our successful cure for the hierarchy problem.

1.5.2 The construction of the MSSM

Having seen how the MSSM alleviates the hierarchy problem, we now cast our attention to the construction of realistic models of supersymmetric particle physics. The construction of the SM yields that each of the known fundamental particles is in either a chiral or gauge supermultiplet and must have a superpartner with spin differing by 1/2 unit. Since only chiral supermultiplets can contain fermions whose left-handed parts transform differently under the gauge group than their right-handed parts, all of the SM fermions must be contained in chiral supermultiplets. The left-handed and right-handed components of the quarks and leptons are separate two-component Weyl spinors with different gauge transformation properties, consequently, each must have its own complex scalar partner, called "squark" and "slepton," respectively, by convention. In general, superpartners of fermions gain a prefix "s-." Similar to the construction of matter fields, all the gauge bosons must be members of massless gauge supermultiplets, and each must have its own spinor partner, called "gaugino." In general, superpartners of bosons gain a suffix "-ino." All the chiral and gauge supermultiplets carry the same gauge quantum numbers as in the SM, and the scalar, spinor, and auxiliary fields of the same supermul-

tiplet must be in the same representation of the gauge group. The only exception to this rule is that the MSSM must contain two species of Higgs supermultiplets, rather than one as is possible in the SM. This is because of the structure of SUSY theories; more precisely, the demand that the superpotential be a holomorphic[4] function of complex scalars and coupling constants, so only the $Y = 1/2$ Higgs chiral supermultiplet can give mass to up-type quarks, and only the $Y = -1/2$ Higgs can give mass to down-type quarks and charged leptons. The physical SM Higgs boson is therefore a mixture of H_u^0 and H_d^0, each of which has its own spinor partner, called "Higgsino." All of the supermultiplets are summarized in Tables 1.4 and 1.5, in which all the chiral supermultiplets are defined in terms of left-handed Weyl spinors, so the conjugates of the right-handed quarks and leptons appear. There are, of course, 3 generations of quark and lepton superfields, denoted by the subscript $i = 1, 2, 3$.

The most general renormalizable nongauge interactions for chiral supermultiplets allowed in SUSY models are determined by a single holomorphic function of the complex scalar fields, the *superpotential*,

$$W = \frac{1}{2} M^{ij} \phi_i \phi_j + \frac{1}{6} y^{ijk} \phi_i \phi_j \phi_k, \tag{1.29}$$

where all of the coefficients M^{ij} and y^{ijk} are completely determined by the SM. The most general Lagrangian for chiral supermultiplets is

[4]In fact, it is the holomorphicity of the superpotential that maintains the absence of quadratic divergences in radiative corrections to scalar masses in the MSSM to all orders in perturbation because of the perturbative nonrenormalization theorems [103], even when it is not protected by a symmetry.

Table 1.4. The chiral supermultiplets in the MSSM in gauge eigenstate.

	Supermultiplet	**Scalar field**	**Spinor field**	$SU(3)_C$	$SU(2)_L$	$U(1)_Y$
Quark sector	Q_i	$(\tilde{u}_L\ \tilde{d}_L)$	$(u_L\ d_L)$	**3**	**2**	$1/6$
($i = 1, 2, 3$)	$\bar{u}_i$	$\tilde{u}_R^*$	$u_R^\dagger$	$\bar{\mathbf{3}}$	**1**	$-2/3$
	$\bar{d}_i$	$\tilde{d}_R^*$	$d_R^\dagger$	$\bar{\mathbf{3}}$	**1**	$1/3$
Lepton sector	L_i	$(\tilde{\nu}_e\ \tilde{e}_L)$	$(\nu_e\ e_L)$	**1**	**2**	$-1/2$
($i = 1, 2, 3$)	$\bar{e}_i$	$\tilde{e}_R^*$	$e_R^\dagger$	**1**	**1**	1
Higgs sector	H_u	$(H_u^+\ H_u^0)$	$(\widetilde{H}_u^+\ \widetilde{H}_u^0)$	**1**	**2**	$1/2$
	H_d	$(H_d^0\ H_d^-)$	$(\widetilde{H}_d^0\ \widetilde{H}_d^-)$	**1**	**2**	$-1/2$

Table 1.5. The gauge supermultiplets in the MSSM in the gauge eigenstate.

	Supermultiplet	**Spinor field**	**Vector field**	$SU(3)_{\rm C}$	$SU(2)_{\rm L}$	$U(1)_Y$
$SU(3)_{\rm C}$	g	$\tilde{g}$	g	**8**	**1**	0
$SU(2)_{\rm L}$	$W^{1,2,3}$	$\widetilde{W}^{1,2,3}$	$W^{1,2,3}$	**1**	**3**	0
$U(1)_Y$	B	$\widetilde{B}$	B	**1**	**1**	0

$$\begin{aligned}\mathcal{L}_{\rm chiral} = &-D^\mu \phi^{*i} D_\mu \phi_i + i\psi^{\dagger i}\bar{\sigma}^\mu D_\mu \psi_i + \mathcal{F}^{*i}\mathcal{F}_i \\ &- \frac{1}{2}M^{ij}\psi_i\psi_j - \frac{1}{2}M^*_{ij}\psi^{\dagger i}\psi^{\dagger j} - \frac{1}{2}y^{ijk}\phi_i\psi_j\psi_k - \frac{1}{2}y^*_{ijk}\phi^{*i}\psi^{\dagger j}\psi^{\dagger k} \\ &+ \left(M^{ij}\phi_j + \frac{1}{2}y^{ijk}\phi_j\phi_k\right)\mathcal{F}_i + \left(M^*_{ij}\phi^{*j} + \frac{1}{2}y^*_{ijk}\phi^{*j}\phi^{*k}\right)\mathcal{F}^{*i}, \quad (1.30)\end{aligned}$$

and the most general interactions for gauge supermultiplets are

$$\begin{aligned}\mathcal{L}_{\rm gauge} = &-\frac{1}{4}F^a_{\mu\nu}F^{a\mu\nu} + i\lambda^{\dagger a}\bar{\sigma}^\mu D_\mu \lambda^a + \frac{1}{2}\mathcal{D}^a\mathcal{D}^a \\ &- \sqrt{2}g(\phi^{*i}T^a\psi_i)\lambda^a - \sqrt{2}g\lambda^{\dagger a}(\psi^{\dagger i}T^a\phi_i) + g(\phi^{*i}T^a\phi_i)\mathcal{D}^a. \quad (1.31)\end{aligned}$$

Thus, realistic renormalizable supersymmetric gauge models can be constructed unambiguously by adding $\mathcal{L}_{\rm MSSM} = \mathcal{L}_{\rm chiral} + \mathcal{L}_{\rm gauge}$, which are surely invariant under the following SUSY transformations,

$$\begin{aligned}\delta\phi_i &= \epsilon\psi_i \\ \delta\psi_{i\alpha} &= -i(\sigma^\mu\epsilon^\dagger)_\alpha D_\mu\phi_i + \epsilon_\alpha\mathcal{F}_i \\ \delta\mathcal{F}_i &= -i\epsilon^\dagger\bar{\sigma}^\mu D_\mu\psi_i + \sqrt{2}g(T^a\phi)_i\epsilon^\dagger\lambda^{\dagger a} \\ \delta\lambda^a_\alpha &= \frac{i}{2\sqrt{2}}(\sigma^\mu\bar{\sigma}^\nu\epsilon)_\alpha F^a_{\mu\nu} + \frac{1}{\sqrt{2}}\epsilon_\alpha\mathcal{D}^a \\ \delta A^a_\mu &= -\frac{1}{\sqrt{2}}\left(\epsilon^\dagger\bar{\sigma}_\mu\lambda^a + \lambda^{\dagger a}\bar{\sigma}_\mu\epsilon\right) \\ \delta\mathcal{D}^a &= \frac{i}{\sqrt{2}}\left(-\epsilon^\dagger\bar{\sigma}^\mu D_\mu\lambda^a + D_\mu\lambda^{\dagger a}\bar{\sigma}^\mu\epsilon\right), \quad (1.32)\end{aligned}$$

alongside with the gauge transformations,

$$\begin{aligned}A^a_\mu &\to A^a_\mu + \partial_\mu\Lambda^a + gf^{abc}A^b_\mu\Lambda^c \\ \lambda^a &\to \lambda^a + gf^{abc}\lambda^b\Lambda^c \\ X_i &\to X_i + ig\Lambda^a(T^aX)_i, \quad (1.33)\end{aligned}$$

for $X_i = \phi_i, \psi_i, \mathcal{F}_i$. By eliminating the nonpropagating auxiliary fields $\mathcal{F}_i$, $\mathcal{F}^{*i}$, and $\mathcal{D}^a$ using their equations of motion and the relations $V(\phi, \phi^*) = \mathcal{F}^{*i}\mathcal{F}_i$, we obtain

$$\mathcal{L}_{\text{chiral}} = -D^\mu \phi^{*i} D_\mu \phi_i + i\psi^{\dagger i}\bar{\sigma}^\mu D_\mu \psi_i - \frac{1}{2}M^{ij}\psi_i\psi_j - \frac{1}{2}M^*_{ij}\psi^{\dagger i}\psi^{\dagger j} - \frac{1}{2}y^{ijk}\phi_i\psi_j\psi_k - \frac{1}{2}y^*_{ijk}\phi^{*i}\psi^{\dagger j}\psi^{\dagger k} - V(\phi, \phi^*) \quad (1.34)$$

and

$$\mathcal{L}_{\text{gauge}} = -\frac{1}{4}F^a_{\mu\nu}F^{a\mu\nu} + i\lambda^{\dagger a}\bar{\sigma}^\mu D_\mu \lambda^a - \sqrt{2}g(\phi^{*i}T^a\psi_i)\lambda^a - \sqrt{2}g\lambda^{\dagger a}(\psi^{\dagger i}T^a\phi_i) - \frac{1}{2}g^2(\phi^{*i}T^a\phi_i)^2, \quad (1.35)$$

where the scalar field interactions are given by

$$V(\phi, \phi^*) = M^*_{ik}M^{kj}\phi^{*i}\phi_j + \frac{1}{2}M^{il}y^*_{jkl}\phi_i\phi^{*j}\phi^{*k} + \frac{1}{2}M^*_{il}y^{jkl}\phi^{*i}\phi_j\phi_k + \frac{1}{4}y^{ijn}y^*_{kln}\phi_i\phi_j\phi^{*k}\phi^{*l}, \quad (1.36)$$

which make possible a variety of gauge and non-gauge interactions.

One of the promising features of the MSSM is that the three gauge couplings apparently unify at a single energy scale [104]. The one-loop renormalization group (RG) equations for the SM gauge couplings $\alpha_a = g_a^2/4\pi$ for $g_{1,2,3}$ are

$$\frac{d}{dt}\alpha_a^{-1}(t) = -\frac{b_a}{2\pi}, \quad (1.37)$$

where $t = \ln(Q/Q_0)$, with Q the RG scale, and $(b_1, b_2, b_3) = (41/10, -19/6, -7)$ for the SM and $(33/5, 1, -3)$ for the MSSM, where the difference comes from the extra MSSM particles entering in loops. Here g_a are conventionally defined by $g_1 = \sqrt{5/3}g'$, $g_2 = g$ and $g_3 = g_s$,[5] where g_s is the coupling constant of the $SU(3)_C$ gauge group. Figure 1.9 compares the RG evolution of the $\alpha_a^{-1}(t)$ [24], including two-loop effects, in the SM (dashed lines) and the MSSM (solid lines). Unlike the SM, the MSSM includes just the right particle content[6] to ensure that the gauge couplings unify at an energy below the Planck scale, strongly implying a Grand Unified Theory (GUT), which occurs at $Q_{GUT} \sim 2 \times 10^{16}$ GeV.

[5]This normalization is chosen to agree with the canonical covariant derivative for grand unification of the gauge group $SU(3)_C \otimes SU(2)_L \otimes U(1)_Y$ into $SU(5)$ or $SO(10)$.

[6]In the MSSM case, the masses of the supersymmetric particles are treated as a common threshold varied between 500 GeV and 1.5 TeV.

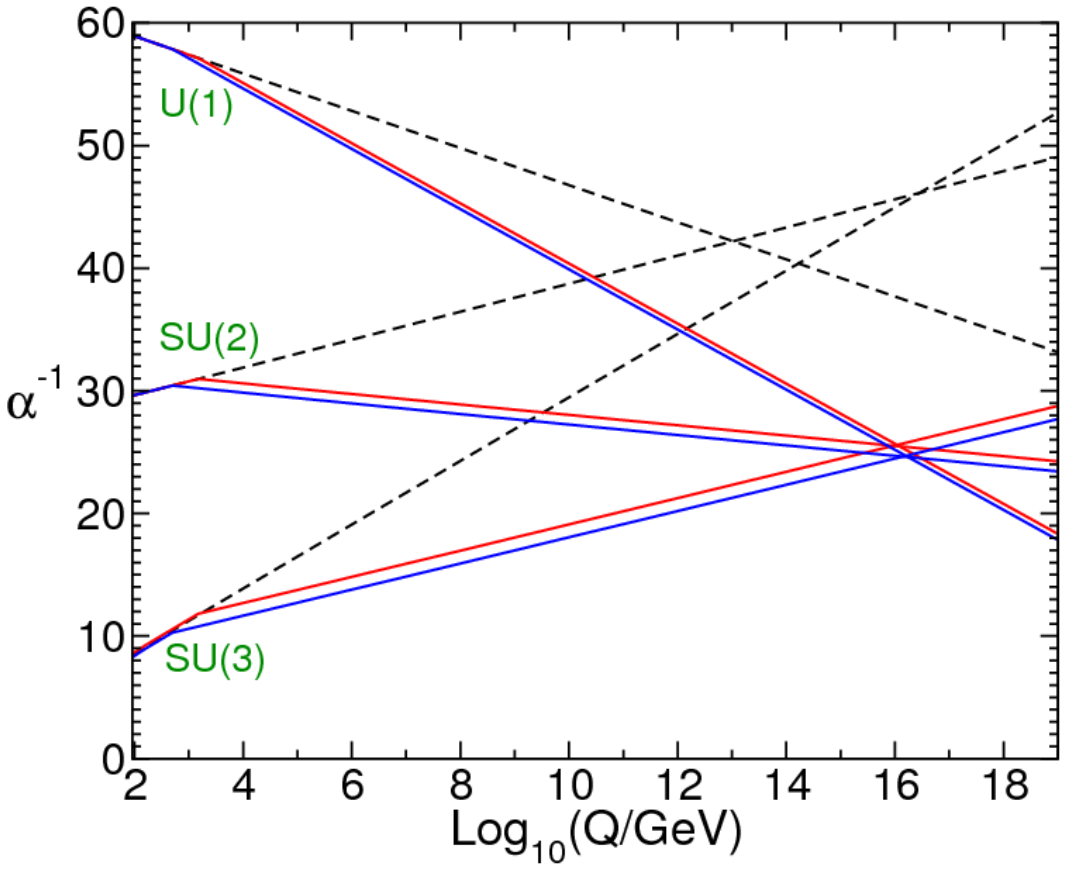

Figure 1.9. The two-loop renormalization group equation of the inverse gauge couplings $\alpha_a^{-1}(Q)$ in the SM (dashed lines) and the MSSM (solid lines) [24], which unify at a scale at $Q_{GUT} \sim 2 \times 10^{16}$ GeV. In the MSSM case, the masses of the supersymmetric particles are treated as a common threshold varied between 500 GeV and 1.5 TeV, and $\alpha_3(m_Z)$ is varied between 0.117 and 0.121.

1.5.3 R-parity and the LSP stability

So far we have seen that the MSSM with soft SUSY breaking provides some particle species that are massive and electrically and color neutral, namely neutralinos and sneutrinos. In order to be consistent with cosmological constraints, suitable candidates for the WIMP must be stable, at least on cosmological scales. In this section, we introduce a new discrete symmetry, called R-parity, which ensures the stability of the lightest SUSY particle (LSP), and therefore provides long-lived dark matter candidates.

R-parity is defined as $R_p = (-1)^{3(B-L)+2s}$. Here B is the baryon number carried by the chiral supermultiplets Q_i ($B = +1/3$) and $\bar{u}_i$ and $\bar{d}_i$ ($B = -1/3$), L is the total lepton number carried by L_i ($L = +1$) and $\bar{e}_i$ ($L = -1$), and s is the spin of the particle. All

the SM particles have even R-parity ($R_p = 1$), while all of the SUSY particles have odd R-parity ($R_p = -1$). Introducing exact R-parity prevents the models from having terms which violate baryon and lepton number conservation, rather than deliberately removing those terms by hand. In addition, if R-parity is exactly conserved, then there can be no mixing between the SM particles and sparticles, and every interaction vertex in the theory must contain an even number of $R_p = -1$ particles. As a consequence, the reactions such as $\tilde{\chi}_i \leftrightarrow X_j \tilde{\chi}_k$ (decay), $\tilde{\chi}_i X_j \leftrightarrow \tilde{\chi}_k X_l$ (interaction), $\tilde{\chi}_i \tilde{\chi}_j \leftrightarrow X_k X_l$ (annihilation, production), are allowed, while decays of the single SUSY particle into the SM particles, $\tilde{\chi}_i \leftrightarrow X_j X_k$, are forbidden.

1.5.4 Phenomenology of the MSSM

We have seen that general renormalizable supersymmetric gauge models can be constructed by Eqs. (1.34), (1.35), and (1.36), and that the MSSM can be constructed by adding the chiral and gauge supermultiplets with the correct gauge quantum numbers, summarized in Tables 1.4 and 1.5. In this section, we discuss the various implications of the new particles for phenomenology.

1.5.4.1 The Higgs sector and EWSB

We now investigate the phenomenological implications of the MSSM. To get a clear idea of the nongauge interactions generated by the scalar potential $V(\phi, \phi^*)$, we will write down only the terms associated with the neutral Higgs fields and the up-type leptons that couple to the Higgs field, essentially the top quark. The same argument is applicable for down-type leptons as well, aside from the replacement of H_u^0 with H_d^0. In this case, the superpotential is just

$$W = y_f \tilde{f}_L \tilde{f}_R^* H_u^0 - \mu H_u^0 H_d^0, \tag{1.38}$$

and scalar field interaction terms of the neutral Higgs sector and the up-type sfermion sector are given by

$$\begin{aligned} -\mathcal{L}_{\text{int}}^{\text{chiral}} = {} & |\mu|^2 (|H_u^0|^2 + |H_d^0|^2) \\ & - \mu y_f^* \tilde{f}_L^* \tilde{f}_R H_d^0 - \mu^* y_f \tilde{f}_L \tilde{f}_R^* H_d^{*0} + |y_f|^2 (|\tilde{f}_L|^2 + |\tilde{f}_R|^2) |H_u^0|^2 \\ & + |y_f|^2 |\tilde{f}_L|^2 |\tilde{f}_R|^2. \end{aligned} \tag{1.39}$$

Notice that as mentioned in the argument of the Higgs field instability above, the dimensionless coupling of $|\tilde{f}_{L.R}|^2|H_u^0|^2$ is indeed $|y_f|^2$, so the vanishing of the quadratic divergence is certainly guaranteed. One also sees that adding terms such as $m_{\tilde{F}}^2|\tilde{f}_L|^2$, $m_{\tilde{f}}^2|\tilde{f}_R|^2$, $(a_f y_f \tilde{f}_L \tilde{f}_R^* H_d^0 + h.c.)$, $m_{u,d}^2|H_{u,d}^0|^2$ and $-b(H_u^0 H_d^0 + h.c.)$ to the interaction Lagrangian does not spoil the quadratic divergence cancellation. These terms break SUSY softly, and are therefore called soft SUSY-breaking terms. We will see that the first two parameters, namely the soft masses for sfermions, m_F and $m_{\tilde{f}}$, and the couplings to the Higgs fields, a_f, determine the mixing angles and CP-violating phases for sfermions, and the last two parameters, namely the soft masses for the Higgs fields, $m_{u,d}$ and b, play a crucial roll in EWSB. In general, unlike the term that exactly conserves SUSY, the SUSY-breaking part contains many unknown parameters and a considerable amount of arbitrariness which cannot be deduced from the SM. Constraining such parameters is discussed in detail in Sec. 1.5.7. Bearing these in mind, we will study the mechanism of EWSB in this section, and the mass spectrum and mixing angle patterns of the sfermions in Sec. 1.5.4.2.

We now inspect the new scalar quartic interactions associated with the gauge couplings. Again for definiteness we look only at the gauge couplings of $U(1)_Y$ and $SU(2)_{\rm L}$ with the neutral Higgs bosons and up-type sfermions. In this case, the last term of Eq. (1.35) becomes

$$-\mathcal{L}_{\rm int}^{\rm gauge} = \frac{g^2}{8}\sum_{a=1,2,3}\left(\begin{bmatrix}H_u^{+*} & H_u^{0*}\end{bmatrix}\sigma^a\begin{bmatrix}H_u^+\\ H_u^0\end{bmatrix} + \begin{bmatrix}H_d^{0*} & H_d^{-*}\end{bmatrix}\sigma^a\begin{bmatrix}H_d^0\\ H_d^-\end{bmatrix} + \begin{bmatrix}\tilde{f}_L^* & \tilde{f}_L'^*\end{bmatrix}\sigma^a\begin{bmatrix}\tilde{f}_L\\ \tilde{f}_L'^*\end{bmatrix}\right)^2 + \frac{g'^2}{2}\left(\frac{1}{2}|H_u^0|^2 - \frac{1}{2}|H_d^0|^2 + Y_L|\tilde{f}_L|^2 + Y_R|\tilde{f}_R|^2\right)^2, \quad (1.40)$$

where $\tilde{f}_L'$ is the down-type sfermion in the same $SU(2)_{\rm L}$ doublet with $\tilde{f}_L$. This can be simplified as

$$-\mathcal{L}_{\rm int}^{\rm gauge} = \frac{g^2}{8}\left(-|H_u^0|^2 + |H_d^0|^2 + |\tilde{f}_L|^2 + \cdots\right)^2 + \frac{g'^2}{2}\left(\frac{1}{2}|H_u^0|^2 - \frac{1}{2}|H_d^0|^2 + Y_L|\tilde{f}_L|^2 + Y_R|\tilde{f}_R|^2\right)^2. \quad (1.41)$$

Some of the cross terms induce the mass splitting between $\tilde{f}_L$ and $\tilde{f}_R$ by EWSB.

The classical scalar potential for the Higgs boson fields in the MSSM is given by

$$V = (|\mu|^2 + m_{H_u}^2)(|H_u^+|^2 + |H_u^0|^2) + (|\mu|^2 + m_{H_d}^2)(|H_d^0|^2 + |H_d^-|^2)$$

$$+ b(H_u^+ H_d^- - H_u^0 H_d^0 + c.c.)$$
$$+ \frac{1}{8}(g^2 + g'^2)(|H_u^+|^2 + |H_u^0|^2 - |H_d^0|^2 - |H_d^-|^2)^2 + \frac{g^2}{2}|H_u^+ H_d^{0*} - H_u^0 H_d^{-*}|^2. \quad (1.42)$$

The terms proportional to $|\mu|^2$ are contributions from the chiral scalar potential, terms proportional to the gauge couplings are from $\mathcal{D}$-terms, and terms proportional to $m^2_{H^0_{u,d}}$ and b are from the soft SUSY-breaking terms. Here we can set $H_u^+ = H_d^- = 0$ at the minimum of the potential, since $SU(2)_{\rm L}$ gauge transformations allow us to choose that the charged components of the Higgs bosons do not get VEVs, hence, the expression can be simplified as

$$V = (|\mu|^2 + m^2_{H_u})|H_u^0|^2 + (|\mu|^2 + m^2_{H_d})|H_d^0|^2 - b(H_u^0 H_d^0 + c.c.)$$
$$+ \frac{1}{8}(g^2 + g'^2)(|H_u^0|^2 - |H_d^0|^2)^2. \quad (1.43)$$

Notice that without negative soft SUSY-breaking mass terms for the Higgs bosons, the Higgs potential is nonnegative with a minimum at $H_u^0 = H_d^0 = 0$. The potential is bounded from below by the following requirements: (i) the quadratic part of the scalar potential must be positive along the $\mathcal{D}$-flat directions $H_u^0 = H_d^0$; (ii) one linear combination of H_u^0 and H_d^0 must have a negative squared mass near $H_u^0 = H_d^0 = 0$; and (iii) the potential must have a minimum satisfying $\langle H_u^0 \rangle = v_1/\sqrt{2}$ and $\langle H_d^0 \rangle = v_2/\sqrt{2}$, and $v^2 = v_1^2 + v_2^2 \simeq (246\,\text{GeV})^2$. One obtains the following conditions necessary for electroweak symmetry breaking, $SU(2)_{\rm L} \otimes U(1)_Y \to U(1)_{\rm EM}$, to occur,

$$\sin(2\beta) = \frac{2b}{m^2_{H_u} + m^2_{H_d} + 2|\mu|^2}$$
$$m_Z^2 = \frac{|m^2_{H_u} - m^2_{H_d}|}{\sqrt{1 - \sin^2(2\beta)}} - m^2_{H_u} - m^2_{H_d} - 2|\mu|^2, \quad (1.44)$$

where $\tan\beta = v_1/v_2$. One of the striking traits of the MSSM is that EWSB can be naturally induced as $m^2_{H_{u,d}}$ is RG-evolved to negative or small values at the electroweak scale due to the significant radiative corrections driven by the large Yukawa coupling of the t-quark [105]. This mechanism is known as radiative electroweak symmetry breaking. Meanwhile, the sfermions, which receive smaller quantum corrections, do not get VEVs. Hence, $SU(3)_{\rm C} \otimes U(1)_{\rm EM}$ is preserved. An example of the RG evolution of the mass spectrum of sparticles and the Higgs scalars is illustrated [24] in Figure 1.10. Here both

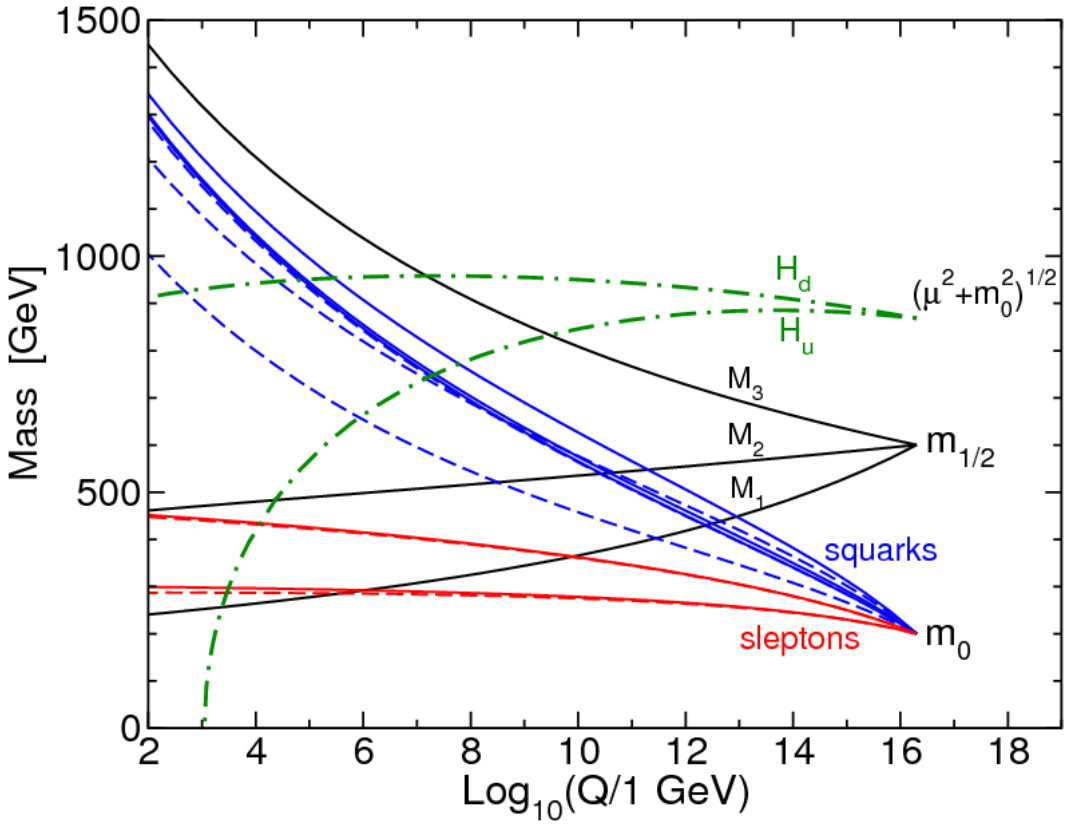

Figure 1.10. RG evolution of scalar and gaugino mass parameters in the MSSM [24] with a typical MSUGRA boundary conditions ($m_0 = 200$ GeV, $M_{1/2} = -A_0 = 600$ GeV, $\tan\beta = 10$, and sign(μ)= +) imposed at $Q = 2 \times 10^{16}$GeV. The parameter $(\mu^2 + m_{H_u}^2)$ runs negative mainly due to the large Yukawa coupling of the t and $\tilde{t}$, provoking EWSB, whilst the mass of sleptons and squarks remains positive.

Higgs masses are $\sqrt{\mu^2 + m_0^2}$ at $Q = 2 \times 10^{16}$ GeV, whilst all sfermions' masses are m_0. The meaning of m_0 and $M_{1/2}$ will be explained in Sec. 1.5.5. In this case, the mass of H_u becomes negative at the EW-scale, triggering EWSB. When EW symmetry is broken, the Higgs scalar fields in the MSSM mix to comprise two CP-even neutral scalars, h^0 and H^0, one CP-odd neutral scalar, A^0, and a charged scalar, $H^{\pm}$. The light CP-even Higgs scalar, h^0, has properties that resemble those of the minimal SM Higgs boson. At tree level, the MSSM bounds on the lightest Higgs mass are $m_h < m_Z \cos(2\beta) \leq m_Z$, and since the superpotential is not renormalized in perturbation theory, the Higgs mass remains small even if one includes the radiative corrections [103]. The computations that incorporate the leading two-loop contributions yield $m_h \lesssim 135$ GeV [101] in the large $\tan\beta$ regime for $m_t = 175\,\text{GeV}$ and $m_{\tilde{t}_1} m_{\tilde{t}_2} \lesssim (2\,\text{TeV})^2$. The prediction of a relatively light Higgs boson

is associated with the shallow Higgs potential due to the small value of the coefficient in front of the quartic terms, $(g^2 + g'^2)$.

1.5.4.2 The sfermions and chiral mixing

Eq. (1.39) gives rise to sfermion mixing, which may provide some important consequences for particle physics phenomenology. This can be seen as follows: when EWSB occurs, sfermions acquire mass, which, in the chiral-eigenstate basis $(\tilde{f}_L\ \tilde{f}_R)$, is given by

$$-\mathcal{L}^{\text{sfermion}}_{\text{mass}} = \begin{bmatrix}\tilde{f}_L^* & \tilde{f}_R^*\end{bmatrix} \begin{bmatrix} m_f^2 + \Delta_{\tilde{f}_L} + m_F^2 & y_f^*(-\mu v_2 + a_f^* v_1)/\sqrt{2} \\ y_f(-\mu^* v_2 + a_f v_1)/\sqrt{2} & m_f^2 + \Delta_{\tilde{f}_R} + m_{\tilde{f}}^2 \end{bmatrix} \begin{bmatrix}\tilde{f}_L \\ \tilde{f}_R\end{bmatrix}. \tag{1.45}$$

Here m_f is the fermion mass $y_f v_1/\sqrt{2}$ as in the SM, $\Delta_{\tilde{f}_{L,R}} = m_Z^2 \cos 2\beta (T_3 - Q \sin^2\theta_W)$ denotes the hyperfine splitting due to the gauge interactions of scalar quartic terms in the $\mathcal{D}$-term contribution, and m_F and $m_{\tilde{f}}$ are the soft SUSY-breaking masses for $\tilde{f}_L$ and $\tilde{f}_R$, respectively. Eq. (1.45) can be rewritten as

$$-\mathcal{L}^{\text{sfermion}}_{\text{mass}} = \begin{bmatrix}\tilde{f}_L^* & \tilde{f}_R^*\end{bmatrix} \begin{bmatrix} m_f^2 + \Delta_{\tilde{f}_L} + m_F^2 & m_f(a_f^* - \mu \cot\beta) \\ m_f(a_f - \mu^* \cot\beta) & m_f^2 + \Delta_{\tilde{f}_R} + m_{\tilde{f}}^2 \end{bmatrix} \begin{bmatrix}\tilde{f}_L \\ \tilde{f}_R\end{bmatrix}. \tag{1.46}$$

Changing the basis to the mass eigenstates, we diagonalize the mass matrix with unitary matrices, which can be written generally as

$$\begin{bmatrix}\tilde{f}_1 \\ \tilde{f}_2\end{bmatrix} = \begin{bmatrix} e^{i\phi_1}\cos\alpha & -e^{-i\phi_2}\sin\alpha \\ e^{i\phi_2}\sin\alpha & e^{-i\phi_1}\cos\alpha \end{bmatrix} \begin{bmatrix}\tilde{f}_L \\ \tilde{f}_R\end{bmatrix}. \tag{1.47}$$

Here α is the sfermion mixing angle, since it parametrizes the mixing of $\tilde{f}_L$ and $\tilde{f}_R$. It is expected that the third generation of sleptons may have a large mixing angle due to the large Yukawa coupling, as seen in Eq. (1.46). The sneutrino mass comes from the soft mass and the gauge interactions, $m_{\tilde{\nu}}^2 = m_L^2 + \frac{1}{2} m_Z^2 \cos 2\beta$.

1.5.4.3 The EW gaugino sector

The third and fourth terms in Eq. (1.35) give gaugino-fermion-sfermion interactions, associated with the gauge interactions. For instance, the interactions of $U(1)_Y$ gaugino, $\widetilde{B}$, with sfermions $\tilde{f}_{L,R}$ are

$$-\mathcal{L}^{\text{gauge}}_{\text{int}} = \sqrt{2} g' \widetilde{B}^\dagger \left(Y_L f_L^\dagger \tilde{f}_L + Y_R f_R^\dagger \tilde{f}_R \right) + h.c. \tag{1.48}$$

The possible soft SUSY-breaking terms in the gauge interactions are the soft masses for gauginos $\left(-\frac{1}{2} M_a \lambda^a \lambda^a\right)$, which turn out to play a vital roll in SUSY phenomenology.

Now we study the mass spectrum of neutralinos. In general, the Higgsinos and electroweak gauginos mix with each other to form neutralinos, χ_i^0, and charginos, $\chi_i^\pm$, because of the effect of EWSB. Here we will investigate all terms related to the masses of the gauginos and Higgsinos. First, from the given superpotential we obtain the mixing terms of the Higgsinos in the chiral interactions,

$$W = \mu(H_u^+ H_d^- - H_u^0 H_d^0) \tag{1.49}$$

$$-\mathcal{L}_{\text{mass}}^{\text{chiral}} = \frac{\mu}{2}(-\widetilde{H}_u^0 \widetilde{H}_d^0 + \widetilde{H}_u^+ \widetilde{H}_d^- + h.c.). \tag{1.50}$$

The $SU(2)_{\text{L}} \otimes U(1)_Y$ gauge interactions generate the couplings of the Higgs scalars with Higgsinos with gauginos,

$$\begin{aligned} -\mathcal{L}_{\text{mass}}^{\text{gauge}} = \sqrt{2}g \sum_{i=1,2,3} \left(\begin{bmatrix} H_u^{+*} & H_u^{0*} \end{bmatrix} \frac{\sigma^i}{2} \begin{bmatrix} \widetilde{H}_u^+ \\ \widetilde{H}_u^0 \end{bmatrix} \widetilde{W}^i + \begin{bmatrix} H_d^{0*} & H_d^{-*} \end{bmatrix} \frac{\sigma^i}{2} \begin{bmatrix} \widetilde{H}_d^0 \\ \widetilde{H}_d^- \end{bmatrix} \widetilde{W}^i + h.c. \right) \\ + \sqrt{2}g' \left(\frac{1}{2} H_u^{0*} \widetilde{H}_u^0 \widetilde{B} - \frac{1}{2} H_d^{0*} \widetilde{H}_d^0 \widetilde{B} + h.c. \right). \end{aligned} \tag{1.51}$$

Rewriting Eq. (1.51), we get

$$\begin{aligned} -\mathcal{L}_{\text{mass}}^{\text{gauge}} = \frac{\sqrt{2}}{2} \left[H_u^{0*} \widetilde{H}_u^0 (g' \widetilde{B} - g \widetilde{W}^3) + H_d^{0*} \widetilde{H}_d^0 (-g' \widetilde{B} + g \widetilde{W}^3) + h.c. \right] \\ + \frac{\sqrt{2}}{2} g \left[H_u^{0*} \widetilde{H}_u^+ \widetilde{W}^- + H_d^{0*} \widetilde{H}_d^- \widetilde{W}^+ + h.c. \right], \end{aligned} \tag{1.52}$$

where $\widetilde{W}^\pm = (\widetilde{W}^1 \mp i\widetilde{W}^2)/\sqrt{2}$, which is analogous to the charged weak vector in the SM. Finally the soft SUSY-breaking terms provide

$$\begin{aligned} -\mathcal{L}_{\text{soft}} &= \frac{1}{2} M_1 \widetilde{B}\widetilde{B} + \frac{1}{2} M_2 \sum_{i=1,2,3} \widetilde{W}^i \widetilde{W}^i \\ &= \frac{1}{2} M_1 \widetilde{B}\widetilde{B} + \frac{1}{2} M_2 \left(\widetilde{W}^3 \widetilde{W}^3 + \widetilde{W}^+ \widetilde{W}^- + \widetilde{W}^- \widetilde{W}^+ \right). \end{aligned} \tag{1.53}$$

Collecting all of these terms, the mass matrices for the neutralinos and charginos in the gauge-eigenstate basis $(\widetilde{\psi}^0)^T = (\widetilde{B}\ \widetilde{W}^3\ \widetilde{H}_d^0\ \widetilde{H}_u^0)$ and $(\widetilde{\psi}^\pm)^T = (\widetilde{W}^+\ \widetilde{H}_u^+\ \widetilde{W}^-\ \widetilde{H}_d^-)$ are

$$-\mathcal{L}_{\text{mass}} = \frac{1}{2} (\widetilde{\psi}^0)^\dagger \mathbf{M}_{\widetilde{\chi}_i^0} \widetilde{\psi}^0 + \frac{1}{2} (\widetilde{\psi}^\pm)^\dagger \mathbf{M}_{\widetilde{\chi}_i^\pm} \widetilde{\psi}^\pm, \tag{1.54}$$

where, with the Higgs scalar fields replaced by their VEVs, the neutralino mass matrix is given by

$$\mathbf{M}_{\chi_i^0} = \begin{bmatrix} M_1 & 0 & -g'v_2 & g'v_1 \\ 0 & M_2 & gv_2 & -gv_1 \\ -g'v_2 & gv_2 & 0 & -\mu \\ g'v_1 & -gv_1 & -\mu & 0 \end{bmatrix}, \tag{1.55}$$

which can be rewritten in terms of the parameters m_Z, θ_W, and β as

$$\mathbf{M}_{\chi_i^0} = \begin{bmatrix} M_1 & 0 & -m_Z c_\beta s_W & m_Z s_\beta s_W \\ 0 & M_2 & m_Z c_\beta c_W & -m_Z s_\beta c_W \\ -m_Z c_\beta s_W & m_Z c_\beta c_W & 0 & -\mu \\ m_Z s_\beta s_W & -m_Z s_\beta c_W & -\mu & 0 \end{bmatrix}. \tag{1.56}$$

The chargino mass matrix is in 2×2 block form,

$$\mathbf{M}_{\chi_i^\pm} = \begin{bmatrix} \mathbf{O} & \mathbf{X} \\ \mathbf{X}^T & \mathbf{O} \end{bmatrix}, \tag{1.57}$$

with

$$\mathbf{X} = \begin{bmatrix} M_2 & \sqrt{2} g v_2 \\ \sqrt{2} g v_1 & \mu \end{bmatrix} = \begin{bmatrix} M_2 & \sqrt{2} m_W c_\beta \\ \sqrt{2} m_W s_\beta & \mu \end{bmatrix}. \tag{1.58}$$

Thus the chargino mass spectra are doubly degenerate.

The RG evolution of gaugino soft masses $M_{1,2,3}$ are shown in Figure 1.10. Here all gauginos' masses are taken to have the same value $M_{1/2}$ at $Q = 2 \times 10^{16}$ GeV. The meaning of m_0 and $M_{1/2}$ will be explained in Sec. 1.5.5. In this case, one sees the large separation of $M_{1,2}$ and M_3 at the EW scale. This holds true in the standard cases, as the running gluino mass grows relatively quickly into the infrared because of the larger QCD couplings compared to those of the EW gauge.

1.5.4.4 Phenomenology of neutralinos

In the previous section, we have seen that the mass spectrum of neutralinos and charginos depends on μ and the soft SUSY-breaking parameters $M_{1,2,3}$. As the lightest neutralino can be a favorite candidate for the WIMP,[7] the variation of the mass spectrum and its phenomenological implication are of interest. In this section, we discuss how those SUSY parameters affect the annihilation of neutralinos, and hence the thermal relic density of CDM.

We have seen that the mass eigenvalues of the neutralino are obtained by diagonalizing the 4×4 matrix, and so the mixture of each eigenstate is obtained by solving quartic equations, which in general is quite complicated and not intuitive. If we take the limit in which $m_Z \ll |\mu \pm M_1|, |\mu \pm M_2|$, then the neutralino mass eigenstates become nearly

[7] Sneutrinos have also long been considered as WIMP candidates. However the sneutrino LSP scenario is refuted by the invisible Z width measurements at LEP [106] and the Heidelberg-Moscow direct double β decay experiment [107].

$\chi_1^0 \approx \widetilde{B}$ (mostly bino) with $m_{\chi_1^0} \approx M_1$, $\chi_2^0 \approx \widetilde{W}^3$ (mostly wino) with $m_{\chi_2^0} \approx M_2$, and $\chi_{3,4}^0 \approx (\widetilde{H}_u^0 \pm \widetilde{H}_d^0)/\sqrt{2}$ (mostly Higgsino) with $m_{\chi_{3,4}^0} \approx |\mu|$. Under this condition, the chargino mass eigenstates consist of $\chi_1^\pm \approx \widetilde{W}^\pm$ (mostly wino) with $m_{\chi_1^\pm} \approx M_2$ and $\chi_2^\pm \approx \widetilde{H}_u^+$ or $\widetilde{H}_d^-$ (mostly Higgsino) with $m_{\chi_2^\pm} \approx |\mu|$.

If the LSP is mostly Higgsino-like, $M_{1,2} \gg |\mu|$, the mass difference δ between $\chi_{3,4}^0$ is very small:

$$\delta \simeq \frac{8 m_Z^2 \sin^2\theta_W}{3 M_1}, \tag{1.59}$$

and the Higgsino-like neutralinos are also degenerate with the Higgsino-like chargino, $\chi_2^\pm$. The high degeneracy of the LSP and other SUSY particles leads to efficient annihilation processes because of the effects known as "coannihilation" [108, 109] and "Sommerfeld enhancement" [110–112]. Therefore, in order for the Higgsino-like neutralino to be the LSP, it must have a large mass (heavier than a few TeV) so that its relic density is consistent with the observed value. The same argument also applies to the wino-like neutralino, whose mass is degenerate with the mostly-wino chargino, $\chi_1^\pm$. This is in tension with our estimate, that the masses of at least the lightest few superpartners should not be much greater than the TeV scale in order for the MSSM scalar potential to provide a Higgs VEV resulting in the observed weak boson masses without fine tuning.

Aside from efficient annihilation due to coannihilation or Sommerfeld Enhancement, neutral wino and Higgsino states can also couple directly to SM gauge bosons, resulting in efficient annihilations, and therefore an underabundance of dark matter, unless the pure wino or Higgsino LSP is relatively heavy. Including the effects from neutralino-chargino coannihilation, Sommerfeld enhancement, and Sudakov enhancement due to electroweak radiative corrections to two initial-state neutralinos, one finds Higgsino LSPs must be heavier than $\sim$ 1.1 TeV and wino LSPs must be heavier than $\sim$ 2.6 TeV for the thermal relic abundance of each to explain the entirety of the dark matter [113–115].

If, on the other hand, the LSP is a bino-like neutralino, then large sfermion masses typically lead to a small annihilation cross section, since processes mediated by sfermions are p-wave suppressed. If, however, the LSP bino and the next-to-lightest SUSY particle (NLSP), in many cases one of the sleptons or squarks, are degenerate in mass to within $\sim$ 10%, then coannihilation takes place and drastically reduces the relic density [109, 116–119]. Another case of annihilation enhancement is that since the bino is a Majorana

fermion, if the mass of the bino-like LSP is about half of the mass of the CP-odd neutral Higgs, m_A, then the Higgs pole resonance takes place to boost the annihilation rate significantly [108, 120, 121].

1.5.5 The constrained MSSM

As explained earlier, the most general MSSM contains a vast number of free parameters, most of which are from the soft SUSY-breaking terms; careful counting yields 124 independent physical parameters in total, of which 105 are from the SUSY extension [122, 123]. As seen in Eq. (1.38), the most general holomorphic, renormalizable, and R-parity-conserving superpotential W contains:

(i) A complex Higgsino mass parameter μ

(ii) Nine Yukawa couplings

The soft SUSY-breaking sector contains:

(i) Three complex gaugino Majorana mass parameters, $M_{1,2,3}$

(ii) Five diagonal hermitian 3×3 matrices of sfermon squared-mass parameters, $(\mathbf{m}^2_{\tilde{\mathbf{f}}})^i_j$, where $f = Q$, $\bar{u}$, $\bar{d}$, L, $\bar{e}$, corresponding to the scalar fields in the chiral supermultiplets, listed in Table 1.4

(iii) Three scalar squared-mass parameters, $m^2_{H_{u,d}}$ and b, which appear in the diagonal Higgs squared-mass terms, $m^2_{u,d}|H^0_{u,d}|^2$, and a complex off-diagonal Higgs squared-mass term, $-b(H^0_u H^0_d + h.c.)$

(iv) Three complex 3×3 matrices $(\mathbf{a}_{\mathbf{f}})^i_j$, which appear in the holomorphic Higgs-sfermion-sfermion trilinear interaction terms, $\left((\mathbf{a}_{\mathbf{f}})_{ij}\tilde{f}^i_L \tilde{f}^{*j}_R H^0_{u,d} + h.c.\right)$, where $f = u$, d, e, and i, j can be different flavor

These new parameters can potentially cause lepton number violation of individual leptons e, μ, τ; unsuppressed flavor-changing neutral currents (FCNCs); and additional CP violation that is inconsistent with the experimental bounds. The nonobservation of baryon and lepton number violation such as proton decay and $\mu \to e\gamma$ decay, as well as the absence of FCNCs, places strong constraints on the off-diagonal matrix elements of $(\mathbf{m}^2_{\tilde{\mathbf{f}}})^i_j$

and $(\mathbf{a_f})^i_j$ [124–128]. Additionally, some combinations of the complex phase of the gaugino mass parameters, the trilinear parameters, and μ must be less than $\mathcal{O}(10^{-2})$-$\mathcal{O}(10^{-3})$ to avoid generating electric dipole moments for the neutrons, electron, and atoms [129–132].

Potential flavor-changing and CP-violating effects in the MSSM are easily evaded if one assumes "soft SUSY-breaking universality," an idealized limit in which the sfermion squared-mass matrices $(\mathbf{m}^2_\mathbf{f})^i_j$ and the trilinear coupling matrices $(\mathbf{a_f})^i_j$ are diagonal in flavor space, or flavor-blind. This strongly restricts sfermion mixing among different flavors. SUSY contributions to FCNC processes will therefore be suppressed. Making the further assumption that trilinear couplings are each proportional to the corresponding Yukawa coupling matrix, $\mathbf{a}_f = A_f \mathbf{y_f}$, for $f = u, d, e$, ensures that only the third family can have large trilinear couplings. Here, A_f are often called "A-parameters". Furthermore, one can avoid disastrously large CP-violating effects by assuming that the soft SUSY-breaking parameters do not introduce new complex phases. If one assumes $\mathrm{Im}(M_{1,2,3}) = \mathrm{Im}(A_{u,d,e}) = 0$, then all flavor-violating and CP-violating transitions are governed by the Cabibbo-Kobayashi-Maskawa (CKM) matrix [133], and therefore the general structure of FCNC processes present in the SM is preserved by new physics. These conditions make up the hypothesis of "minimal flavor violation" (MFV).

The "irrelevancy" or "decoupling" idea, where the sparticle masses are extremely heavy so that their contributions to flavor-changing and CP-violating diagrams are strongly suppressed, can also address the absence of observations of flavor-changing and CP-violating processes.

The number of parameters can further be reduced if one assumes a unified field theory at a high-energy scale. As in the SM, this approach exhibits MFV, which comes from the nontrivial flavor structure of the trilinear Higgs-fermion Yukawa couplings. Moreover, the strong implication of GUT suggests that the other MSSM couplings and soft mass parameters might be unified at the GUT scale Q_{GUT} as well.

With this line of thought, the soft SUSY-breaking parameters at the high-energy scale take a particularly simple form:

$$(\mathbf{m}^2_\mathbf{f})^i_j(Q_{GUT}) = m_0^2\mathbf{1},\ m^2_{H_{u,d}}(Q_{GUT}) = m_0^2,\ M_{1,2,3}(Q_{GUT}) = M_{1/2},\ A_{u,d,e}(Q_{GUT}) = A_0, \tag{1.60}$$

where $\mathbf{1}$ is the 3×3 identity matrix in flavor space. The model which imposes mass and tri-

linear universality conditions is called the constrained Minimal Supersymmetric Standard Model (CMSSM) and has only 5 free real input parameters: the sign of μ, $\tan\beta = v_1/v_2$, m_0, $M_{1/2}$, and A_0. Additionally, the gravitino mass $m_{3/2}$ is also considered as a free parameter in the CMSSM. However, $m_{3/2}$ is independent of the parameters that govern the mass spectrum of the superpartners of the SM, and is often assumed implicitly to be irrelevantly large. We note that the CMSSM is a two-parameter generalization of the model which assumes gravity-mediated supersymmetry breaking at the Planck scale, often referred to as the minimal supergravity (mSUGRA) model, which is a real UV-complete fundamental theory with GUT-scale universality.

1.5.6 Simplified models

It is also possible to probe the MSSM by focusing on a small subset of the supersymmetric particle spectrum and studying its phenomenology with minimal theoretical bias. In this simplified model approach, we assume that observables, such as cross sections, branching ratios and masses, depend only on a few relevant parameters, and thus provide a framework for studies of supersymmetric phenomena, independently of the precise details of the theory that govern the supersymmetric parameters. A simplified model should fulfill the following criteria [98]: (i) it should be simple enough to form a credible unit within a more complicated model; (ii) it should be complete enough to be able to describe accurately the relevant physics phenomena; (iii) the Lagrangian should contain all terms that are renormalizable and consistent with Lorentz invariance, the SM gauge symmetries, and DM stability; and (iv) the additional interactions should not violate the exact and approximate accidental global symmetries of the SM. A simplified model can be understood as a limit of a more general new-physics scenario, where all but the lightest dark-sector states are integrated out. The physics of such models can therefore be characterized in terms of a small number of parameters, such as particle masses and couplings.

1.5.7 Constraints on the MSSM

Weak-scale supersymmetry was motivated as a natural solution to the hierarchy problem, providing the mechanism of EWSB without a significant fine-tuning of the fundamental parameters of the MSSM. In this context, the soft SUSY-breaking masses must be

generally $\mathcal{O}(1)$ TeV or below, which may serve as a constraint on the MSSM parameters.

At present, there is no evidence for weak-scale supersymmetry from the data analyzed by the LHC experiments. Recent LHC data has ruled out the existence of colored supersymmetric particles, primarily the gluino and the first two generations of squarks with mass below $\sim$ 1 TeV [5]. The tension between the present experimental lower limits on the masses of colored supersymmetric particles and the expectation of weak scale SUSY was exacerbated by the observed value of the Higgs mass at $\sim$ 125 GeV by the ATLAS and CMS experiments [34–37, 39, 40].

Additional constraints arise from precision EW observables, which place limits on contributions of virtual supersymmetric particle exchange to a variety of SM processes [134–136]. There are a number of low-energy measurements that are sensitive to the effects of new physics through indirect searches via supersymmetric loop effects. Those measurements include m_W, $\sin^2\theta_W$, the Z-pole Γ_Z, m_h, and the muon anomalous magnetic moment $a_\mu = (g_\mu - 2)/2$. Currently the theoretical SM prediction for a_μ exhibits a deviation at the level of 3-4 σ from the observed value [137]. The present sparticle mass bounds [138], however, are rendering the SUSY interpretation of a_μ somewhat dubious in the CMSSM.

The rare decay $B_s \to \mu^+\mu^-$ is especially sensitive to supersymmetric loop effects, with some loop contributions scaling as $\tan^6\beta$ when $\tan\beta \gg 1$ [139–142]. The observations of this rare decay mode along with the first observation of $B_d \to \mu^+\mu^-$ are compatible with the predicted SM rates at the 1.2σ and 2.2σ level, respectively [143]. Increasing pressure is being placed on models with large $\tan\beta$ by the strengthening experimental constraint on the rate of $B_s \to \mu^+\mu^-$, and in particular, the recent detection by LHCb of $B_s \to \mu^+\mu^-$ with a value close to the SM prediction [144–146].

In models with extended Higgs sectors, the decays $B^\pm \to \tau^\pm\nu_\tau$ and $B \to D^{(*)}\tau^-\bar{\nu_\tau}$ may also be relevant since these processes possess tree-level charged Higgs exchange contributions that can compete with the dominant W-exchange. Measurements by the Belle Collaboration are consistent with SM expectations [147]. The BaBar Collaboration measured values of the rates for $B \to D\tau^-\bar{\nu_\tau}$ and $B \to D^*\tau^-\bar{\nu_\tau}$ that showed a combined 3.4σ discrepancy from the SM predictions [148, 149]. Subsequent measurements by the Belle and LHCb Collaborations [150, 151] are consistent with the BaBar measurements. The most recent Belle measurements are also compatible (at the 2σ level) with either the

SM or a two-Higgs doublet model [151].

The flavor changing neutral current decay $b \to s\gamma$ is of remarkable theoretical interest and has been the subject of numerous theoretical investigations [152]. Its total branching fraction is very sensitive to physics beyond the SM as it may be affected by the presence of charged Higgs or supersymmetric particles in the loop mediating this transition, which may lead to substantial deviations from the predicted rate. The present theoretical prediction for the branching fraction within the SM is $\mathcal{B}(b \to s\gamma) = (3.28 \pm 0.33) \times 10^{-4}$, or $(3.73 \pm 0.30) \times 10^{-4}$ [153], depending on a choice for the scale-dependence of the charm quark mass. The CLEO Collaboration has reported a measurement of the branching fraction $\mathcal{B}(b \to s\gamma) = (3.21 \pm 0.43 \pm 0.27^{+0.18}_{-0.10}) \times 10^{-4}$, where the errors are statistical, systematic, and from theory corrections. This result is in good agreement with the SM prediction. The Belle Collaboration has reported $\mathcal{B}(b \to s\gamma) = (3.55 \pm 0.32^{+0.30+0.11}_{-0.31-0.07}) \times 10^{-4}$ [154], where, again, the errors are statistical, systematic, and from theory corrections. The BABAR Collaboration has reported $\mathcal{B}(B \to X_s\gamma) = (3.88 \pm 0.36 \pm 0.37^{+0.43}_{-0.23}) \times 10^{-4}$ [155, 156], where the errors are statistical, systematic, and from theory corrections. None of the deviations from the SM in rare B decays are significant enough to definitively rule out the SM. The absence of discrepancies in these B-physics observables from their SM predictions also places useful constraints on the MSSM parameter space [126–128, 157–159].

1.5.8 Viable parameter space in the CMSSM

Currently, much of the low-mass parameter space in the CMSSM has been excluded by the principal, experimental, phenomenological, and cosmological constraints on SUSY models [25], which include: (i) the measured cosmological abundance of CDM; (ii) the strongest upper limit on the spin-independent CDM-nucleon scattering cross section; (iii) the limits on flavor-changing processes; (iv) the limits from searches for missing-energy events provided by the LHC experiments ATLAS and CMS; and (v) the measurement of the properties of the Higgs boson by CMS and ATLAS.

Figure 1.11 displays the interplay of these constraints in the ($M_{1/2}$, m_0) plane of the CMSSM for $\tan\beta = 10$ and 40, and $A_0 = 2.5m_0$, assuming $\mu > 0$. m_h is in general too small for low A_0, in which case the parameter space is largely excluded. The brown shaded

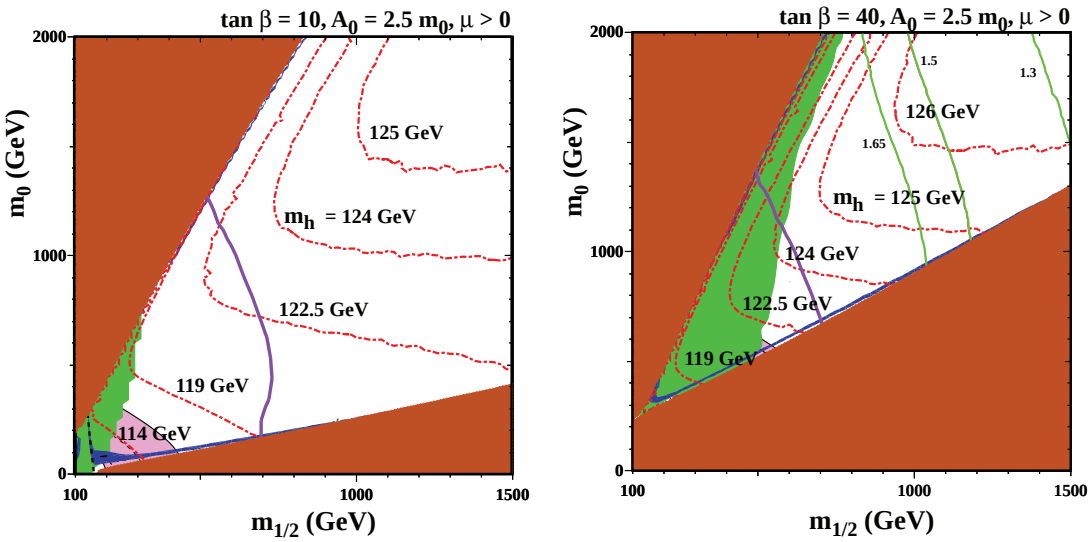

(a) $\tan\beta = 10$ (b) $\tan\beta = 40$

Figure 1.11. Viable parameter space [25] in the ($M_{1/2}$, m_0) planes of the CMSSM for $A_0 = 2.5m_0$, $\mu > 0$ and (a) $\tan\beta = 10$ or (b) $\tan\beta = 40$, after the discovery of the Higgs boson at the LHC. Much of the low-mass parameter space in the CMSSM has been excluded by the principal, experimental, phenomenological, and cosmological constraints on SUSY model, which include: (i) the measured cosmological abundance of CDM-nucleon; (ii) the strongest upper limit on the spin-independent CDM scattering cross section; (iii) the limits on flavor-changing processes; (iv) the limits from searches for missing-energy events provided the LHC experiments ATLAS and CMS; and (v) the measurement of the properties of the Higgs boson by CMS and ATLAS. See the text for the description of each shading and contour.

region is where the stau (in the lower right) or stop (in the upper left) becomes the LSP or tachyonic. The regions excluded by $b \to s\gamma$ are shaded green. The LEP chargino exclusion is shown as a near-vertical dashed black line at small $M_{1/2}$. Those regions favored by $(g_\mu - 2)$ are shaded pink. And those favored by the thermal relic density $\Omega_c h^2 \approx 0.1$ are shaded dark blue.[8] Contours of m_h are shown as red dash-dotted lines, and the ATLAS exclusion from the search for events with missing transverse energy (MET) is shown as a solid purple line. The three green lines apparent in the $\tan\beta = 40$ case are contours of $\mathcal{B}(B_s \to \mu^+\mu^-)/\mathcal{B}(B_s \to \mu^+\mu^-)_{\rm SM} = 1.65$, 1.5, and 1.3, which are the 95% CL upper limit from LHCb alone, that of LHCb and combined experiments, and the 68% CL upper limit from LHCb [144–146].

[8]Note that, here, an enlarged range for the DM density ($0.06 < \Omega_c h^2 < 0.2$) is shaded for reasons of visibility.

For the $\tan\beta = 40$, $A_0 = 2.5m_0$ case, there is compatibility for $M_{1/2} > 1\,\text{TeV}$ along the $\tilde{\tau}_1$ coannihilation strip. This region is also compatible with the LHC MET constraint. To the right of the $\tilde{t}_1$ LSP boundary there is a stop coannihilation strip which occurs at relatively low m_h when $\tan\beta = 10$ and is in the region excluded by $b \to s\gamma$ when $\tan\beta = 40$. The MET constraint allows only the upper end of the coannihilation strip close to the $\tilde{\tau}_1$ LSP boundary. The $B_s \to \mu^+\mu^-$ constraint has no impact for low $\tan\beta$, but for $\tan\beta = 40$ its restriction on the coannihilation strip is stronger than that of the MET constraint. The bulk region is excluded by the Higgs mass and the rare B decay constraints. In summary, one can conclude that the parameter space compatible with constraints from the Higgs boson mass and cosmology is only a very restricted coannihilation region in the large $\tan\beta$ and A_0 case, which is all excluded by rare B_s decay measurements.

CHAPTER 2

NEW BULK REGION

The great advantages of supersymmetric models include the elimination of quadratic divergences, precision grand unification, and the presence of an acceptable dark matter candidate. Frameworks such as the CMSSM also elegantly satisfy experimental constraints on flavor-changing neutral currents (FCNCs). As of February 2017, the most recent measurement of the dark matter abundance from the Planck satellite is $\Omega_c h^2 = 0.1188 \pm 0.0010$ [49, 50].

For the remainder of this dissertation, we consider a scenario in which the requirements of MFV, vanishing *CP*-violation, and mass universality are relaxed, specifically focusing on scenarios with light sleptons. We find a large region of parameter space, analogous to the original bulk region, for which the lightest neutralino is a thermal relic with an abundance consistent with that of dark matter. We find that these leptophilic models are constrained by measurements of the magnetic and electric dipole moments of the electron and muon, and that these models have interesting signatures at a variety of direct and indirect detection experiments, including the gamma-ray signals from DM annihilation, which we explore in the following chapters.

In this chapter, we introduce the model in detail and identify the key relationships between the parameters of the model: DM mass, slepton masses, mixing angles, and *CP*-violating phases.

This chapter is adapted from published articles: Phys. Rev. D **90**, *095007 (2014). MSSM Dark Matter and a Light Slepton Sector: The Incredible Bulk. K. Fukushima, C. Kelso, J. Kumar, P. Sandick, T. Yamamoto.* ©*Owned by the authors, published by American Physical Society, 2014. and Phys. Rev. D* **94**, *015022 (2016). Gamma-Ray Signals from Dark Matter Annihilation via Charged Mediators. J. Kumar, P. Sandick, F. Teng, T. Yamamoto.* ©*Owned by the authors, published by American Physical Society, 2016. With kind permission of the American Physical Society.*

2.1 Motivation

Recent experimental results from the LHC have placed strong constraints on the masses of colored superpartners. The MSSM parameter space is also constrained by the measurement of the Higgs boson mass, and the requirement that the properties of the lightest neutralinos be consistent with dark matter observations. Indeed, as we saw in Sec. 1.5.7, within the CMSSM and other supersymmetric frameworks in which scalar mass universality is assumed, constraints from colliders and cosmology are at odds. Although large regions of the MSSM parameter space are excluded by these combined bounds, leptophilic versions of the MSSM can survive these constraints.

2.1.1 Annihilation and the relic density of DM

In this section, we discuss the thermal relic DM density, where Majorana DM annihilates primally into a pair of SM fermions, $\chi\chi \to \bar{f}f$. Assuming that dark matter is a thermal relic, the freeze-out temperature is computed using the best fit solution to the Boltzmann equation, as in Ref. [56],

$$\frac{1}{x_f} = \ln\left[\sqrt{\frac{45}{8}}\frac{m_\chi m_{\rm Planck}\langle\sigma v\rangle_{x_f}}{g_*^{1/2}\pi^3}x_f^{1/2}\right], \tag{2.1}$$

where m_χ is the dark matter mass, $m_{\rm Planck}$ is the Planck mass, $\langle\sigma v\rangle_{x_f}$ and g_* are the thermally-averaged annihilation cross section and effective number of degrees of freedom, respectively, at freeze-out, and $x_f = T_f/m_\chi$, where T_f is the freeze-out temperature. The cold dark matter relic abundance is then simply [160]

$$\Omega_c h^2 \simeq \frac{8.77\times10^{-11}\ {\rm GeV}^{-2}}{\sqrt{g_*}\int_0^{x_f} dx\,\langle\sigma v\rangle_x}. \tag{2.2}$$

Since x_f depends only logarithmically on the annihilation cross section, the relic density is roughly inversely proportional to $\langle\sigma v\rangle_{x_f}$. To obtain a relic density in agreement with the observed value, one would need $\langle\sigma v\rangle_{x_f} \sim 0.7$ pb (see also [161]).

As explained in Sec. 1.5.4.4, if dark matter is electroweak-scale (~ 100 GeV) neutralinos, they must be dominantly bino-like. However, for bino-like dark matter in the standard scenarios, there are well-known difficulties in obtaining an annihilation cross section large enough to sufficiently deplete the dark matter relic density, since processes mediated by

sfermions are suppressed. If DM annihilation exhibits no s-channel resonances, one can expand $\langle \sigma v \rangle$ in powers of $x = m_\chi / T$ [160, 162] as

$$\langle \sigma v \rangle = c_0 + c_1 x + \mathcal{O}(x^2), \tag{2.3}$$

where c_0 and c_1 are the velocity-independent s-wave and the velocity-dependent p-wave contribution, respectively. For Majorana DM annihilation, the s-wave part of the annihilation cross section is chirality-suppressed by a factor $\sim m_f^2 / m_\chi^2$, while the p-wave part of the cross section is velocity-suppressed by a factor $v^2 \approx 0.1$ at freeze-out.

There is, however, a scenario with light sfermions and an electroweak-scale bino-like neutralino LSP, wherein no special mechanism such as coannihilation or resonance annihilation is necessary to suppress the relic abundance to within the range measured by the Planck satellite, $\Omega_c h^2 = 0.1188 \pm 0.0010$ [49, 50]. This has long been termed the "bulk" region in the CMSSM [108, 163–166], though it has been excluded for some time because it predicts light squarks and a light CP-even Higgs boson with a low mass $m_h \lesssim 114$ GeV.

But if one departs from the assumption of minimal flavor violation in the slepton sector, then there can be large mixing of left- and right-handed sleptons, which eliminates the chirality-suppression. Electroweak-scale bino-like dark matter is therefore a viable option so long as some sfermions are sufficiently light to mediate the annihilation. We then find a new allowed "bulk" region in a scenario that constitutes a minimal leptophilic version of the MSSM.

2.1.2 Collider constraints on the MSSM

Extensive searches for supersymmetric particles, including the lightest supersymmetric particle (LSP) dark matter candidate, have been carried out using a variety of approaches. As of February 2017, the absence of any direct production of sfermions at the LHC excludes gluinos and 1st/2nd generation squarks (if degenerate) with masses $\lesssim 1$ TeV, while the sbottom and stop must be heavier than ~ 100 GeV [5]. Moreover, the discovery of a Standard Model-like Higgs boson with mass $m_h \sim 125$ GeV [39, 40] indicates $m_{\tilde{t}} \gtrsim \mathcal{O}(1$ TeV) [167]. If scalar mass universality is assumed, as in the CMSSM [108, 163–165, 168–188], the absence of supersymmetric particles found at the LHC, the Higgs mass, and the lack of experimental evidence of deviations from SM expectations for rare decays all force the sfermion masses to be heavy as well [25, 189–195].

In spite of these tight constraints on the squark masses and the very limited viable parameter space of the CMSSM, the current data still leave open the possibility of models that possess relatively light sleptons and an electroweak-scale bino-like LSP, but with much heavier squarks. Bounds on the masses of sleptons are much weaker than on squark masses; in particular, the selectron, smuon, and stau need only be heavier than $\sim$ 100 GeV [5].

In this context, we examine a model that relaxes the standard assumptions of mass universality, minimal flavor violation, and CP-conservation for the slepton sector. Essentially, the parameters of the $SU(3)_C$-charged sector of the theory and the leptonic sector will be decoupled; the $SU(3)_C$ sector will be chosen to ensure consistency with collider searches and the Higgs mass measurement, while the leptonic sector will provide the annihilation channels required in order for the lightest neutralino to have a thermal relic density that agrees with astronomical observations.

Relaxing scalar mass universality allows us to revive scenarios with electroweak-scale bino-like neutralino dark matter that annihilates via light slepton exchange, while heavy squarks satisfy all collider constraints and boost the Higgs mass to the range measured at the LHC. If one relaxes gaugino universality and takes the $SU(3)_C$ gaugino field to be much heavier than the other gaugino and sfermion fields at the unification scale, then the mass splitting between the electroweakinos and the gluino induces a mass splitting between the sleptons and squarks [196].

The departure from the assumptions of the CMSSM presented here, however, will blemish some of the aforementioned advantages of MSSM as a candidate of new physics; for example, because high-scale universality of soft supersymmetry-breaking mass parameters is relaxed, FCNC constraints are not automatically satisfied, and a moderate fine-tuning of soft SUSY-breaking parameters, or a "little hierarchy," may be introduced. Even so, given the significant tension with data which exists in much of the parameter space of the CMSSM, it is quite possible that some of these motivations must indeed be weakened in any model that can be consistent with observations. The scenario we consider thus represents a relaxation of the motivated assumptions underlying the CMSSM in a way which allows one to cleanly reconcile the model with data.

Supersymmetric constructions with spectra similar to those studied here have been

shown to arise in supergravity grand unification models with gluino-driven radiative supersymmetry-breaking [196]. A similar mass spectrum can also be obtained in so-called split-family supersymmetry, where the sfermions of the first two generations are lighter than those of the third generation. Explicit constructions leading to such spectra are discussed in Ref. [197] and Ref. [198]. Here, we explore the phenomenology of generic MSSM scenarios with electroweak-scale bino-like dark matter and light sleptons. We refer to this scenario as the *new bulk region*.

This study also serves as a guide for understanding the phenomenology of more general models with singlet fermion dark matter that couples to leptons via charged scalars.

2.2 The model and its general features

In the new bulk region, the leading dark matter annihilation channel is $\chi\chi \to \ell^+\ell^-$, through t-channel exchange of sleptons (this scenario is also considered in Ref. [199], and the $\ell = \tau$ scenario is discussed in detail in Ref. [200]). For simplicity, we assume a model in which the dark matter candidate is a SM gauge singlet Majorana fermion, or pure bino LSP in MSSM.[1] We will assume that the only light SUSY particles are the lightest neutralino χ and the sleptons $\tilde{\ell}_{1,2}$. Following the notation in Ref. [201], the interaction Lagrangian can be written as

$$\mathcal{L}_{\rm int} = \sum_{i=1,2} \left[\bar{\ell}(g^L_{\tilde{\ell}_i \ell 1} P_L + g^R_{\tilde{\ell}_i \ell 1} P_R)\chi \tilde{\ell}_i + \bar{\chi}(g^{L^*}_{\tilde{\ell}_i \ell 1} P_R + g^{R^*}_{\tilde{\ell}_i \ell 1} P_L)\ell \tilde{\ell}^*_i \right], \tag{2.4}$$

where $P_{L(R)}$ are the chiral projectors and ℓ is a lepton charged under $U(1)_{\rm EM}$, and $\widetilde{\ell}_{L(R)}$ are the charged scalar mediators. We also assume that the dark matter is absolutely stable because it is the lightest particle charged under an unbroken hidden symmetry, namely R-parity, and the $\widetilde{\ell}_{L(R)}$ are also charged under the same symmetry, while the fermion f is uncharged under the symmetry that stabilizes the dark matter. To ensure that the dark matter is stable, we assume $m_{\widetilde{\ell}_{1,2}} > m_\chi$. However, m_ℓ can be either larger or smaller than m_χ. The coupling constants are explicitly given as,

$$\begin{aligned} g^L_{\tilde{\ell}_1 \ell 1} &= \sqrt{2} g' e^{i\frac{\varphi}{2}} \sin\alpha \epsilon_1 = -\lambda^*_R \sin\alpha \\ g^R_{\tilde{\ell}_1 \ell 1} &= \frac{g'}{\sqrt{2}} e^{-i\frac{\varphi}{2}} \cos\alpha = \lambda^*_L \cos\alpha \end{aligned}$$

[1] Doping the LSP with some Higgsino content would enhance the annihilation cross section. We do not consider this case further.

$$\begin{aligned} g^L_{\tilde{\ell}_2 \ell 1} &= -\sqrt{2} g' e^{i\frac{\varphi}{2}} \cos\alpha \epsilon_1 = \lambda^*_R \cos\alpha \\ g^R_{\tilde{\ell}_2 \ell 1} &= \frac{g'}{\sqrt{2}} e^{-i\frac{\varphi}{2}} \sin\alpha = \lambda^*_L \sin\alpha, \end{aligned} \tag{2.5}$$

where we will take $\epsilon_1 = -1$, and the magnitudes of the constants are determined by the hypercharges of leptons and the $U(1)$ gauge coupling g'. The mixing parameter α relates the slepton mass eigenstates and the chiral eigenstates by

$$\begin{bmatrix} \tilde{\ell}_1 \\ \tilde{\ell}_2 \end{bmatrix} = \begin{bmatrix} \cos\alpha & -\sin\alpha \\ \sin\alpha & \cos\alpha \end{bmatrix} \begin{bmatrix} \tilde{\ell}_L \\ \tilde{\ell}_R \end{bmatrix}. \tag{2.6}$$

The appearance of the CP-violating phase can be explained in the following way: in general, the mass matrix in the chiral basis can be diagonalized by a unitary matrix as

$$\begin{bmatrix} \tilde{\ell}_1 \\ \tilde{\ell}_2 \end{bmatrix} = \begin{bmatrix} e^{i\varphi_1}\cos\alpha & -e^{i\varphi_2}\sin\alpha \\ e^{-i\varphi_2}\sin\alpha & e^{-i\varphi_1}\cos\alpha \end{bmatrix} \begin{bmatrix} \tilde{\ell}_L \\ \tilde{\ell}_R \end{bmatrix}. \tag{2.7}$$

Now noting that any overall phase can be removed by a vectorlike phase rotation of $\tilde{\ell}_{L,R}$, we redefine the scalar fields as

$$\begin{bmatrix} \tilde{\ell}_1 \\ \tilde{\ell}_2 \end{bmatrix} = \begin{bmatrix} e^{i\varphi_1}\cos\alpha & -e^{i\varphi_2}\sin\alpha \\ e^{-i\varphi_2}\sin\alpha & e^{-i\varphi_1}\cos\alpha \end{bmatrix} \begin{bmatrix} e^{i\theta_1}\tilde{\ell}_L \\ e^{i\theta_2}\tilde{\ell}_R \end{bmatrix}. \tag{2.8}$$

We see that, although the most general matrix relating the scalar mass and chiral eigenstates contains three complex phases, they can be absorbed by a phase rotation of the chiral eigenstates, $\tilde{\ell}_{L,R}$, and the mass eigenstates, $\tilde{\ell}_{1,2}$, so that the elements of the unitary matrix are all real. The condition yields: $\varphi_1 + \theta_1 = 0$, $\varphi_2 + \theta_2 = 0$, $\varphi_2 - \theta_1 = 0$, and $\varphi_1 - \theta_2 = 0$. Therefore, choosing $\theta_1 = -\theta_2 = \varphi/2$, the expression becomes

$$\begin{bmatrix} \tilde{\ell}_1 \\ \tilde{\ell}_2 \end{bmatrix} = \begin{bmatrix} \cos\alpha & -\sin\alpha \\ \sin\alpha & \cos\alpha \end{bmatrix} \begin{bmatrix} e^{i\frac{\varphi}{2}}\tilde{\ell}_L \\ e^{-i\frac{\varphi}{2}}\tilde{\ell}_R \end{bmatrix}. \tag{2.9}$$

The phase φ cannot be rotated away any further, and is then absorbed in the coupling constants.

Note that in the case where $\alpha = 0$, the Lagrangian in Eq. (2.4) respects a chiral symmetry, whereas the presence of nonzero α induces a nonzero divergence for the Noether current, and therefore breaks the chiral symmetry. If $\sin 2\alpha = 0$, the requirement that the mixing matrix be real only fixes two phases, in which case, the phase φ can then be absorbed into a chiral rotation of the $\tilde{\ell}_{L,R}$. Similarly, if $m_\ell = 0$, then the phase φ can be removed by a chiral rotation of f. As a result, one can deduce that CP-violating effects must scale as $(m_\ell/m_\chi)\sin 2\alpha$.

Within the MSSM framework, where $\lambda_L = \sqrt{2} g Y_L e^{i\frac{\varphi}{2}}$ and $\lambda_R = \sqrt{2} g Y_R e^{-i\frac{\varphi}{2}}$, we are left with five free parameters for this simplified model: $(m_\chi, m_{\tilde{\ell}_1}, m_{\tilde{\ell}_2}, \alpha, \varphi)$. This scenario has been considered recently in Ref. [199, 200, 202]. In the following chapters, we also briefly consider the possibility of a new heavy fermion, in which case there is an additional parameter necessary to specify its mass, m_ℓ.

Finally, we note that if the left-right slepton mixing angle, α, is large, then one may potentially generate new charge-breaking vacua. If one demands that the charge-neutral vacuum be a global minimum, then very tight constraints are imposed on the mixing angle. But these conditions are weakened if one only requires that the charge-neutral vacuum be metastable, with a lifetime as long as the age of the universe; even maximal mixing is consistent with this metastability condition for the range of masses we consider [203].

CHAPTER 3

TWO-BODY ANNIHILATION

In this chapter, we consider the $\chi\chi \to \bar{f}f$ cross section[1] within the model described in Sec. 2.2. The dominant contribution to $\chi\chi \to \bar{f}f$ is from t and u-channel exchange of sfermions, displayed in Figure 3.1. It is widely known that Majorana DM annihilation into the fermion pair is inefficient due to chiral suppression. In the following section, we see how chiral mixing of the sfermion sector lifts this suppression and thus enhances the cross section.

In the case where $m_f/m_\chi \to 0$, the cross section for the process $\chi\chi \to \bar{f}f$ must scale with the remaining parameters, including $(m_\chi, m_{\tilde{f}_1}, m_{\tilde{f}_2}, \alpha, \varphi)$, which break flavor symmetry. Since the chiral mixing induces a chirality flip, the large value of α enhances the s-wave annihilation rate. The reason is that since the dark matter is Majorana and the initial state wave function must be antisymmetric, the s-wave initial state must have the total angular momentum $J = 0$. The final state $\bar{f}$ and f must then have the same helicity, implying that the f and $\bar{f}$ arise from different Weyl spinors. The final state is thus not invariant under chiral flavor symmetries and must vanish in the $m_f/m_\chi \to 0$ limit in the case of MFV.

In the following section, we see this effect explicitly by carrying out the full calculation of the DM 2-body annihilation cross section.

This chapter is adapted from published articles: Phys. Rev. D **90**, *095007 (2014). MSSM Dark Matter and a Light Slepton Sector: The Incredible Bulk. K. Fukushima, C. Kelso, J. Kumar, P. Sandick, T. Yamamoto.* ©*Owned by the authors, published by American Physical Society, 2014. and Phys. Rev. D* **94**, *015022 (2016). Gamma-Ray Signals from Dark Matter Annihilation via Charged Mediators. J. Kumar, P. Sandick, F. Teng, T. Yamamoto.* ©*Owned by the authors, published by American Physical Society, 2016. With kind permission of the American Physical Society.*

[1] We denote $\bar{f}f$ for the final state when the result is generic for any type of fermion, and $\ell^+\ell^-$ when we specifically consider leptonic final states.

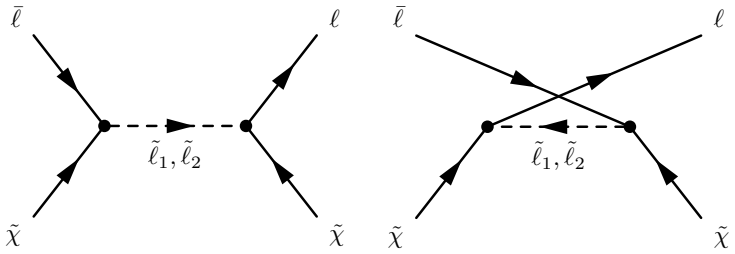

Figure 3.1. Feynman diagrams of $\chi\chi \to \bar{f}f$.

3.1 The cross section of $\chi\chi \to \bar{f}f$

In center of mass frame, we can write the spin-averaged cross section as Eq. (4.84) in Ref. [28]

$$\frac{d\sigma_{\chi\chi\to\bar{f}f}}{d\cos\theta} v_{rel} = \frac{N_c}{64\pi(m_\chi^2+\mathbf{p}^2)} \left[\frac{1}{4}\sum_{\text{spins}} |\mathcal{M}|^2\right] \sqrt{1-\frac{m_f^2}{m_\chi^2+\mathbf{p}^2}}, \tag{3.1}$$

where N_c is the number of colors of final state particles, and where θ is the angle between the incoming dark matter and the outgoing Standard Model leptons. Here, $\sum_{\text{spins}} |\mathcal{M}|^2$ is the sum

$$\begin{aligned}
\sum_{\text{spins}} |\mathcal{M}_{1(s)}|^2 &= 4m_\chi^4 \left(1+\frac{\mathbf{p}^2}{m_\chi^2}\right)^2 \left[(\Re(\Xi_2))^2 + \left(1-\frac{m_f^2}{m_\chi^2+\mathbf{p}^2}\right)(\Im(\Xi_2))^2\right] \\
&\quad + m_f^2 m_\chi^2 \Xi_{1+}^2 - 4m_\chi^3 m_f \left(1+\frac{\mathbf{p}^2}{m_\chi^2}\right) \Re(\Xi_2)\Xi_{1+} \\
\sum_{\text{spins}} |\mathcal{M}_{2(s)}|^2 &= (m_\chi^2 - m_f^2 + \mathbf{p}^2)(2m_\chi^2 + \mathbf{p}^2 + \mathbf{p}^2\cos^2\theta)\Xi_{3-}^2 \\
&\quad + (m_\chi^2 - m_f^2 + \mathbf{p}^2)(m_\chi^2 + \mathbf{p}^2\cos^2\theta)(\Im(\Xi_4))^2 \\
&\quad + \left((m_\chi^2+\mathbf{p}^2)(2m_\chi^2+m_f^2+\mathbf{p}^2) + \mathbf{p}^2(m_\chi^2-m_f^2+\mathbf{p}^2)\cos^2\theta\right)\Xi_{3+}^2 \\
&\quad + \left(2m_\chi^2 m_f^2 + m_f^2\mathbf{p}^2 + m_\chi^2(m_\chi^2+\mathbf{p}^2) + \mathbf{p}^2(m_\chi^2-m_f^2+\mathbf{p}^2)\cos^2\theta\right)(\Re(\Xi_4))^2 \\
&\quad - 6m_\chi m_f (m_\chi^2+\mathbf{p}^2)\Re(\Xi_4)\Xi_{3+} \\
\sum_{\text{spins}} |\mathcal{M}_{1(p)}|^2 &= 4\left[(m_\chi^2 - m_f^2 + \mathbf{p}^2)(\Re(\Xi_2))^2 + (m_\chi^2+\mathbf{p}^2)(\Im(\Xi_2))^2\right]\mathbf{p}^2 \\
&\quad + \Big[(m_\chi^2 - m_f^2 + \mathbf{p}^2)(1+\cos^2\theta)\Xi_{1+}^2 \\
&\quad + \left(m_\chi^2 + m_f^2 + \mathbf{p}^2 + (m_\chi^2 - m_f^2 + \mathbf{p}^2)\cos^2\theta\right)\Xi_{1-}^2\Big]\mathbf{p}^2 \\
\sum_{\text{spins}} |\mathcal{M}_{2(p)}|^2 &= 4(m_\chi^2 - m_f^2 + \mathbf{p}^2)\mathbf{p}^2\cos^2\theta(\Re(\Xi_4))^2
\end{aligned}$$

$$+4(m_f^2+(m_\chi^2-m_f^2+\mathbf{p}^2)\cos^2\theta)\mathbf{p}^2(\Im(\Xi_4))^2, \tag{3.2}$$

where the subscripts on $\mathcal{M}$ are as follows: $1(s)$ indicates initial and final $J=0$ states; $2(s)$ indicates initial and final $J=1$ states; $1(p)$ indicates a $J=0$ initial state and a $J=1$ final state; and $2(p)$ indicates a $J=1$ initial state and a $J=0$ final state, respectively. Here, we use the shorthand notation defined by

$$\begin{aligned}
\Xi_{1+} &= \sum_{i=1,2}(|g^L_{\tilde{f}_i f 1}|^2+|g^R_{\tilde{f}_i f 1}|^2)\Phi_i^+ = \sum_{i=1,2} 2S^+_{f\tilde{f}_i}\Phi_i^+ \\
\Xi_{1-} &= \sum_{i=1,2}(|g^L_{\tilde{f}_i f 1}|^2-|g^R_{\tilde{f}_i f 1}|^2)\Phi_i^+ = \sum_{i=1,2} 2S^-_{f\tilde{f}_i}\Phi_i^+ \\
\Xi_2 &= \sum_{i=1,2} g^{R*}_{\tilde{f}_i f 1} g^L_{\tilde{f}_i f 1}\Phi_i^+ = \sum_{i=1,2} D_{f\tilde{f}_i}\Phi_i^+ \\
\Xi_{3+} &= \sum_{i=1,2}(|g^L_{\tilde{f}_i f 1}|^2+|g^R_{\tilde{f}_i f 1}|^2)\Phi_i^- = \sum_{i=1,2} 2S^+_{f\tilde{f}_i}\Phi_i^- \\
\Xi_{3-} &= \sum_{i=1,2}(|g^L_{\tilde{f}_i f 1}|^2-|g^R_{\tilde{f}_i f 1}|^2)\Phi_i^- = \sum_{i=1,2} 2S^-_{f\tilde{f}_i}\Phi_i^- \\
\Xi_4 &= \sum_{i=1,2} g^{R*}_{\tilde{f}_i f 1} g^L_{\tilde{f}_i f 1}\Phi_i^- = \sum_{i=1,2} D_{f\tilde{f}_i}\Phi_i^-,
\end{aligned} \tag{3.3}$$

with

$$\begin{aligned}
\Phi_i^+ &\equiv \frac{1}{m^2_{\tilde{f}_i}-t}+\frac{1}{m^2_{\tilde{f}_i}-u} \\
\Phi_i^- &\equiv \frac{1}{m^2_{\tilde{f}_i}-t}-\frac{1}{m^2_{\tilde{f}_i}-u}.
\end{aligned} \tag{3.4}$$

t and u are customarily defined as

$$\begin{aligned}
t &= m_f^2-m_\chi^2-2\mathbf{p}^2+2|\mathbf{p}|\sqrt{m_\chi^2+\mathbf{p}^2-m_f^2}\cos\theta \\
u &= m_f^2-m_\chi^2-2\mathbf{p}^2-2|\mathbf{p}|\sqrt{m_\chi^2+\mathbf{p}^2-m_f^2}\cos\theta,
\end{aligned} \tag{3.5}$$

and the products of couplings are defined by

$$\begin{aligned}
S^+_{f\tilde{f}i} &= \frac{1}{2}\left(|g^L_{\tilde{f}_i f 1}|^2+|g^R_{\tilde{f}_i f 1}|^2\right) \\
S^-_{f\tilde{f}i} &= \frac{1}{2}\left(|g^L_{\tilde{f}_i f 1}|^2-|g^R_{\tilde{f}_i f 1}|^2\right) \\
D_{f\tilde{f}i} &= g^{R*}_{\tilde{f}_i f 1} g^L_{\tilde{f}_i f 1}.
\end{aligned} \tag{3.6}$$

Since $\Phi_i^- \sim v$, all terms containing Ξ that are multiplied by Φ_i^-, namely, Ξ_{3+}, Ξ_{3-}, and Ξ_4, are p-wave suppressed. In the massless lepton limit, the dominant contribution comes from $\mathcal{M}_{1(s)}$; all other contributions are suppressed by v^2. In the MSSM, the coupling

constants can be written as $D_{f\tilde{f}i} = \pm g^2 Y_L Y_R \cos\alpha \sin\alpha$, where the $+$ is chosen for $i = 1$ and the $-$ for $i = 2$. In the nonrelativistic limit, $\Phi_i^+ \approx 2/(m_{\tilde{f}_i}^2 + m_\chi^2)$. Therefore, the s-wave contribution, c_0, can also be expressed as

$$c_0 = N_c \frac{m_\chi^2}{2\pi} g^4 Y_L^2 Y_R^2 \cos^2\alpha \sin^2\alpha \left(\frac{1}{m_{\tilde{f}_1}^2 + m_\chi^2} - \frac{1}{m_{\tilde{f}_2}^2 + m_\chi^2} \right)^2 . \tag{3.7}$$

The v^2-suppressed contribution,[2] c_1, is

$$\begin{aligned} c_1 = N_c \frac{m_\chi^2}{2\pi} g^4 \Bigg(& \frac{(Y_L^4 \cos^4\alpha + Y_R^4 \sin^4\alpha)(m_{\tilde{f}_1}^4 + m_\chi^4)}{(m_{\tilde{f}_1}^2 + m_\chi^2)^4} + \frac{(Y_L^4 \sin^4\alpha + Y_R^4 \cos^4\alpha)(m_{\tilde{f}_2}^4 + m_\chi^4)}{(m_{\tilde{f}_2}^2 + m_\chi^2)^4} \\ & + \frac{2(Y_L^4 + Y_R^4)\sin^2\alpha\cos^2\alpha(m_{\tilde{f}_1}^2 m_{\tilde{f}_2}^2 + m_\chi^4)}{(m_{\tilde{f}_1}^2 + m_\chi^2)^2 (m_{\tilde{f}_2}^2 + m_\chi^2)^2} \\ & + \frac{Y_L^2 Y_R^2 \sin^2\alpha\cos^2\alpha(m_{\tilde{f}_1}^2 - m_{\tilde{f}_2}^2)^2}{2(m_{\tilde{f}_1}^2 + m_\chi^2)^4 (m_{\tilde{f}_2}^2 + m_\chi^2)^4} \Big[3 m_{\tilde{f}_1}^4 m_{\tilde{f}_2}^4 - 52 m_\chi^4 m_{\tilde{f}_1}^2 m_{\tilde{f}_2}^2 + 3 m_\chi^8 \\ & - 14 m_\chi^2 (m_{\tilde{f}_1}^2 + m_{\tilde{f}_2}^2)(m_\chi^4 + m_{\tilde{f}_1}^2 m_{\tilde{f}_2}^2) - 5 m_\chi^4 (m_{\tilde{f}_1}^4 + m_{\tilde{f}_2}^4) \Big] \Bigg). \end{aligned} \tag{3.8}$$

While Eqs. (3.7) and (3.8) are valid in the massless fermion limit, both c_0 and c_1 do depend on φ in terms proportional to m_f. The effect of this, however, is not significant for light SM leptons. In the subsequent analysis, we will use the full m_f-dependent forms of c_0 and c_1.

If $\sin(2\alpha)$ is small, then the p-wave term dominates the annihilation cross section, resulting in roughly a factor of 10 suppression in the cross section at freeze out, and yielding a negligible annihilation cross section in the current epoch. But if $\sin(2\alpha) \sim \mathcal{O}(1)$, then the annihilation cross section can be unsuppressed both at freeze-out and in the current epoch.

In this analysis, we explore only $m_\chi = 100$ GeV. If the neutralino mass is smaller, then lighter sleptons must mediate the annihilations. Scenarios with very light neutralinos with 1 GeV $< m_\chi <$ 30 GeV and light sleptons have been explored in Ref. [204] and Ref. [205], though both allow a nonnegligible Higgsino content for the LSP. They find neutralinos as light as 15 GeV with $\sim$ 100 GeV sleptons and $\sim$ 200 GeV charginos and next-to-lightest neutralinos are compatible with all current collider constraints. Since we focus here on $\sim$ 100 GeV dark matter, a more relevant question is how large the LSP mass could be while

[2]The v^2-suppressed terms arise from both the s-wave and p-wave matrix elements, but the s-wave terms will vanish in the $\sin(2\alpha) \to 0$ limit.

remaining in the *new bulk*. We find that if $m_\chi \sim m_{\tilde{\ell}_1}$, then the mediating slepton must be lighter than $\sim$ 150 GeV, making this a well-defined region with quite small charged sparticle masses.[3]

Annihilation from an s-wave initial state can only be relevant to freeze-out (or current observations) if the mixing terms are large. Since right-handed neutrinos have no hypercharge, the only relevant s-wave annihilation channels are those with two charged leptons in the final state. The s-wave annihilation cross section can be expressed as

$$c_0 \sim (1.59\text{ pb}) \left(\frac{m_{\tilde{\ell}_1}}{100\text{ GeV}}\right)^{-2} \sin^2(2\alpha) \left(\frac{2}{r_1^{1/2}+r_1^{-1/2}} - \frac{m_{\tilde{\ell}_1}}{m_{\tilde{\ell}_2}} \frac{2}{r_2^{1/2}+r_2^{-1/2}}\right)^2, \quad (3.9)$$

where $r_i = m_{\tilde{\ell}_i}^2/m_\chi^2$. Assuming $m_{\tilde{\ell}_1} \leq m_{\tilde{\ell}_2}$, it is thus clear that c_0 is maximized for $m_{\tilde{\ell}_2} \gg m_{\tilde{\ell}_1}$ and $\sin(2\alpha) = 1$, with $m_{\tilde{\ell}_1} \sim m_\chi$ and $m_{\tilde{\ell}_1}$ as light as possible. Interestingly, the maximum annihilation cross section is determined by the mass of the lightest slepton, and cannot be increased by further decreasing the mass of the lightest neutralino; collider bounds on the slepton masses thus place a firm bound on the s-wave annihilation cross section. For the lighter sleptons with mass near 100 GeV and with maximal L-R mixing, the s-wave annihilation cross section may be $\mathcal{O}(1)$ pb, providing a large enough annihilation rate to account for the dark matter relic density.

If $\sin(2\alpha) \ll 1$, then the v^2-suppressed terms in the matrix element become important. In this limit,

$$\frac{c_1}{x_f} = (0.6\text{ pb}) \left(\frac{20}{x_f}\right) \left(\frac{m_{\tilde{\ell}_1}}{100\text{ GeV}}\right)^{-2} \left(\frac{8\left(Y_L^4 \cos^4\alpha + Y_R^4 \sin^4\alpha\right)(r_1 + (1/r_1))}{\left(r_1^{1/2}+r_1^{-1/2}\right)^4} + \frac{r_2}{r_1} \frac{8\left(Y_L^4 \sin^4\alpha + Y_R^4 \cos^4\alpha\right)(r_2 + (1/r_2))}{\left(r_2^{1/2}+r_2^{-1/2}\right)^4} \right). \quad (3.10)$$

Assuming $m_{\tilde{\ell}_1} \leq m_{\tilde{\ell}_2}$, it is clear that these v^2-suppressed terms are maximized for $\sin\alpha = 1$ in the charged lepton annihilation channel, and for $\cos\alpha = 1$ for the neutrino channel. If $m_{\tilde{\ell}_1} \sim m_\chi$, then annihilation to each charged lepton can provide a contribution to the annihilation cross section of $\sim$ 0.6 pb; thus, we expect that annihilation into the e, μ and τ channels together can deplete the relic density enough to satisfy observational constraints.

[3]Note that this conclusion is based specifically on the process $\chi\chi \to \bar{\ell}\ell$ via slepton exchange. If $m_\chi/m_{\tilde{\ell}_1} \approx 1$, coannihilation processes may be important, in which case heavier LSPs and heavier sleptons are possible.

We also note that the contribution of the neutrino channel is suppressed by a factor of 16 relative to the charged lepton channels, due to the hypercharge of the left-handed neutrino. Thus, sneutrino mediation can only provide a small contribution to the total annihilation cross section for a viable model. Although these p-wave annihilation channels can play a significant role in dark matter annihilation at freeze-out, they have negligible impact on dark matter annihilation in the present epoch.

In the simplified model that we consider here, the only deviation from MFV arises from the presence of nontrivial mixing of the scalar chiral eigenstates. This requires both a nontrivial left-right mixing angle α and nondegeneracy of the mass eigenstates (if the mass eigenstates are degenerate, then a redefinition of the eigenstates is sufficient to absorb the mixing angle).

CHAPTER 4

GAMMA-RAY SIGNALS

The ongoing annihilations of WIMPs may result in observable cosmic-ray signals, such as in the cosmic gamma-ray spectrum and/or in the cosmic-ray positron and/or antiproton fraction. Typically, various reactions involving the final state lepton pairs result in an almost featureless secondary photon spectrum. In the simplified model, we consider, however, a distinctive feature may be contained in the internal bremsstrahlung (IB) spectrum and the associated line signals.

The ongoing search for such photon signals of dark matter annihilation involves various ground-based and satellite-based experiments. The ground-based atmospheric Cherenkov Telescope Array (CTA) [206, 207] are most effective for dark matter that is somewhat heavier than 100 GeV. The Fermi Gamma-Ray Space Telescope, in contrast, is better suited to study dark matter masses in the range 0.1 to a few hundred GeV, which is the range we are interested in here. In addition, the future satellite-based experiment GAMMA-400 [208] is expected to be launched with better energy resolution and sensitivity, making it possible to distinguish between a sharply peaked IB spectrum and a true line signal.

In this chapter, we outline how we analyze the associated gamma-ray signals that may be observable in indirect dark matter searches. The processes which we will consider are $\chi\chi \to \gamma\gamma$, $\chi\chi \to \gamma Z$, and $\chi\chi \to \bar{f}f\gamma$. All of these processes have been considered in the past [209–212], but either for special cases or different purposes. Our goal here will be to consider the most general spectra that can arise for these processes in a simplified model in which a Majorana fermion dark matter particle couples to a Dirac fermion (which may or may not be a SM fermion) through the exchange of two charged scalars, with an arbitrary

---

This chapter is adapted from published articles: Phys. Rev. D **90**, *095007 (2014). MSSM Dark Matter and a Light Slepton Sector: The Incredible Bulk. K. Fukushima, C. Kelso, J. Kumar, P. Sandick, T. Yamamoto.* ©*Owned by the authors, published by American Physical Society, 2014. and Phys. Rev. D* **94**, *015022 (2016). Gamma-Ray Signals from Dark Matter Annihilation via Charged Mediators. J. Kumar, P. Sandick, F. Teng, T. Yamamoto.* ©*Owned by the authors, published by American Physical Society, 2016. With kind permission of the American Physical Society.*

left-right mixing angle and CP-violating phase.

In particular, we find the most general spectrum for internal bremsstrahlung, which interpolates between the regimes dominated by virtual internal bremsstrahlung and by final state radiation. We also examine the effect of the mixing angle and CP-violating phase on these signals, which raises some intriguing observable signals, including the helicity asymmetry of the photons in the $\chi\chi \to \gamma\gamma$ channel. It has been known for some time that the photon emission due to inverse Compton scattering and bremsstrahlung in the Galactic electromagnetic fields (so-called secondary emission) can be a source of gamma-ray signals, and therefore should be accounted for to reconstruct the observed photon spectrum. However it heavily depends on modeling of the dark matter distribution and cosmic-ray propagation, and is not included in this dissertation, since explaining certain gamma-ray signals from particular regions of galaxies is not our intention.

This chapter is organized as follows: we discuss the general features of the relevant gamma-ray signals in Sec. 4.1. In Sec. 4.2, we describe the monochromatic line signals, and present how we analyze the spectrum in detail. In Sec. 4.3, we similarly describe the general internal bremsstrahlung gamma-ray signature.

We present our numerical results in Sec. 6.6. These include the complete spectrum for the process $\chi\chi \to \bar{f}f\gamma$ as a function of mixing angle, which interpolates between the hard regime, dominated by virtual internal bremsstrahlung, and the soft regime, dominated by soft and collinear final state radiation. The ratio of the cross sections for $\chi\chi \to \gamma\gamma$ to $\chi\chi \to \gamma Z$ as a function of mixing angle and CP-violating phase, and the difference in rates for the production of left-circularly and right-circularly polarized photons via the process $\chi\chi \to \gamma\gamma$, are also discussed.

4.1 General features

If the cross section for the process $\chi\chi \to \bar{f}f$ is not suppressed, it will dominate over processes such as $\chi\chi \to \bar{f}f\gamma$ and $\chi\chi \to \gamma\gamma, \gamma Z$, which will be suppressed by factors of at least $\alpha_{\rm EM}$ and $\alpha_{\rm EM}^2$, respectively. In this case, prompt gamma-ray signals are sometimes considered to be less promising from an observational standpoint, because models that would produce prompt gamma-ray signals large enough to be observed with current or near future experiments can already be probed by searches for cosmic rays produced by

the process $\chi\chi \to \bar{f}f$. However, current exclusion limits based on searches for positrons or antiprotons are subject to large systematic uncertainties related to assumptions about the astrophysical backgrounds and propagation of charged particles in our Galaxy; if these assumptions are weakened, then the exclusion limits from cosmic-ray searches can be similarly weakened, permitting even the suppressed $\chi\chi \to \bar{f}f\gamma$, $\gamma\gamma$, and γZ signals to be relevant. The Feynman diagrams for the two-body annihilation $\chi\chi \to \bar{f}f$ and internal bremsstrahlung $\chi\chi \to \bar{f}f\gamma$ are shown in Figure 4.1, while those for the one-loop process $\chi\chi \to \gamma\gamma$ are shown later in Figure 4.2, where a detailed discussion on this process is presented.

There are two scenarios in which the $\chi\chi \to \bar{f}f$ annihilation cross section is suppressed:

(i) If $m_f > m_\chi$, then $\chi\chi \to \bar{f}f$ is not kinematically allowed.

(ii) If there is minimal flavor violation (MFV), then the cross section for the process $\chi\chi \to \bar{f}f$ is suppressed by a factor $(m_f/m_\chi)^2$.

In the case where $m_f/m_\chi > 1$, the processes $\chi\chi \to \bar{f}f, \bar{f}f\gamma$ are forbidden, allowing the processes $\chi\chi \to \gamma\gamma$ and $\chi\chi \to \gamma Z$ to be the most important (other processes, such as $\chi\chi \to ZZ, W^+W^-$ may have similar cross sections but are likely to be less observationally important compared to a clean gamma-ray signal). This scenario is relevant in the case where dark matter couples to a new, heavy charged fermion.

The photon spectrum is defined as the photon number per annihilation per energy bin, and can be broken into a continuum spectrum and a contribution from monochromatic photons,

$$\frac{dN}{dx} = \left(\frac{dN}{dx}\right)_{\text{cont.}} + \left(\frac{dN}{dx}\right)_{\text{line}}. \tag{4.1}$$

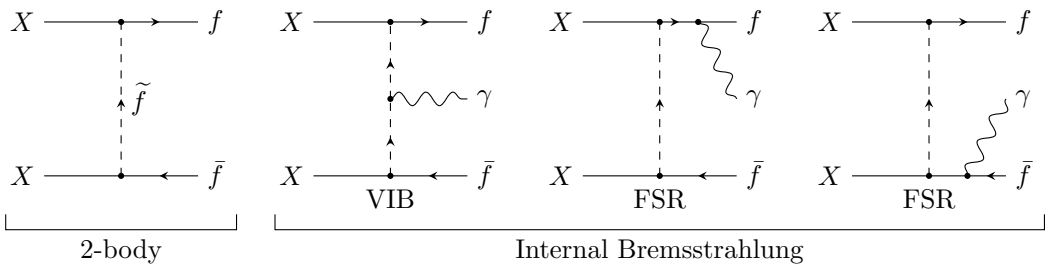

Figure 4.1. Feynman diagrams for two-body annihilation and IB.

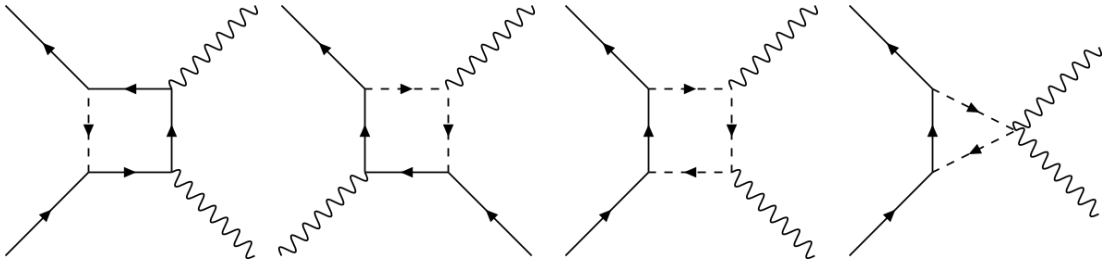

Figure 4.2. Feynman diagrams that contribute to the one-loop process $\chi\chi \to \gamma\gamma$. Diagrams with initial and final state particles exchanged are not listed.

In our case, the continuum spectrum comes mainly from IB and other prompt emission from the final state particles,

$$\left(\frac{dN}{dx}\right)_{\text{cont.}} = \frac{1}{\langle\sigma v\rangle_{\text{tot.}}}\left[\frac{d\,\langle\sigma v\rangle_{\text{IB}}}{dx} + \sum_i N_i \frac{d\,\langle\sigma v\rangle_i}{dx}\right], \tag{4.2}$$

where N_i is the number of photons produced in a single annihilation process and the sum over i includes all higher order prompt emissions, which includes the radiation from hadronic decay of the final state SM particles. $\langle\sigma v\rangle_{\text{IB}}$ is the IB cross section, which will be described in Sec. 4.3. Note that the spectrum is normalized by $\langle\sigma v\rangle_{\text{tot.}}$, the total annihilation cross section, which includes all possible annihilation channels.

As discussed below, the line spectrum consists of the $\gamma\gamma$ and γZ peaks,

$$\left(\frac{dN}{dx}\right)_{\text{line}} = \frac{1}{\langle\sigma v\rangle_{\text{ann.}}}\Big[2\,\langle\sigma v\rangle_{\gamma\gamma}\,\delta(x-1) + \langle\sigma v\rangle_{\gamma Z}\,\delta(x-x_Z)\Big], \tag{4.3}$$

where $x_Z = E_{\gamma Z}/m_\chi$ as given in Eq. (4.4). These definitions follow Ref. [213].

4.2 Monochromatic gamma-ray line signals

Monochromatic lines in the gamma-ray spectrum arise due to the one-loop annihilation process $\chi\chi \to \gamma X$, where $X = \gamma$, Z, or h. The photon(s) in the final state has (have) energy

$$E_{\gamma X} = m_\chi - \frac{m_X^2}{4m_\chi}, \tag{4.4}$$

where m_X is the mass of the particle X. 1% energy resolution is sufficient to differentiate $\gamma\gamma$ and γZ lines for $m_\chi \lesssim 450\,\text{GeV}$. In the Galactic Center, the relative velocity between dark matter particles is $v \sim 10^{-3}$, so the p-wave component of the dark matter annihilation cross section is suppressed.

The s-wave ($L = 0$) component must arise from a spin-singlet initial state ($S = 0$), since the dark matter particles are Majorana fermions and must be in a totally antisymmetric initial state. This state thus necessarily has vanishing total angular momentum ($J = 0$), implying that the final state particles must have the same helicity. As a result, only the $\gamma\gamma$ and γZ cross sections can develop nonvanishing s-wave components, whilst the leading γh cross section must be p-wave suppressed and is thus too small to be observed.

4.2.1 The analytic two-photon cross section

The interaction between the fermion, scalar, and photon is given by

$$\mathcal{L}_{\text{QED}} = Qe\,\overline{f}\gamma^{\mu}A_{\mu}f + \sum_{i=1,2}\left[Q^2e^2A^{\mu}A_{\mu}\tilde{f}_i^{*}\tilde{f}_i + \left(iQe\tilde{f}_i^{*}A^{\mu}\partial_{\mu}\tilde{f}_i - \text{c.c}\right)\right], \tag{4.5}$$

where Q is the electric charge of the fermion and scalar. We denote the momenta of the two initial state dark matter particles as k_1 and k_2, and the momenta of the two final state photons as k_3 and k_4. Since the annihilation takes place between two dark matter particles at rest, the momentum configuration is

$$\begin{aligned} k_1 &= k_2 = k = (m_{\chi}, 0, 0, 0) \\ k_3 &= (m_{\chi}, m_{\chi}\,\hat{n}) \\ k_4 &= (m_{\chi}, -m_{\chi}\,\hat{n}), \end{aligned} \tag{4.6}$$

where the unit vector $\hat{n}$ gives the direction of the photon momentum. Using the spinor helicity formalism, we choose the polarization vectors as

$$\begin{aligned} \epsilon_3^{\mu}(+) \equiv \epsilon_+^{\mu}(k_3;k_4) &= \frac{1}{\sqrt{2}}\frac{[k_3\,|\gamma^{\mu}|\,k_4\rangle}{\langle k_4k_3\rangle} \\ \epsilon_3^{\mu}(-) \equiv \epsilon_-^{\mu}(k_3;k_4) &= \frac{1}{\sqrt{2}}\frac{\langle k_3\,|\gamma^{\mu}|\,k_4]}{[k_4k_3]} \\ \epsilon_4^{\mu}(+) \equiv \epsilon_+^{\mu}(k_4;k_3) &= \frac{1}{\sqrt{2}}\frac{[k_4\,|\gamma^{\mu}|\,k_3\rangle}{\langle k_3k_4\rangle} \\ \epsilon_4^{\mu}(-) \equiv \epsilon_-^{\mu}(k_4;k_3) &= \frac{1}{\sqrt{2}}\frac{\langle k_4\,|\gamma^{\mu}|\,k_3]}{[k_3k_4]}, \end{aligned} \tag{4.7}$$

where the notation follows Ref. [214]. The benefit of this choice is that the inner products between opposite helicity vectors are always zero. Feynman diagrams that contribute to the amplitude are displayed in Figure 4.2.

We write the total amplitude $\mathcal{A}$ as

$$\mathcal{A} = \frac{iQ^2\alpha_{\rm EM}}{2\pi}\,(\epsilon_3\cdot\epsilon_4)\left[\frac{\overline{u}(k_1)\gamma^5 v(k_2)}{2m_\chi}\right]\mathscr{A}(h)\,, \tag{4.8}$$

where $\alpha_{\rm EM}$ is the fine structure constant and $h \equiv (h_3+h_4)/2$ such that $h=1$ for the $(++)$ final and $h=-1$ for the $(--)$ final state. The structure $(\epsilon_3\cdot\epsilon_4)\left(\overline{u}_1\gamma^5 v_2\right)$ reflects the s-wave nature of this amplitude, since this factor is nonzero only for the $L=0$ initial state configuration. Then all the contributions from the loop integrals in Figure 4.2 are collected in $\mathscr{A}(h)$, which we write as

$$\mathscr{A}(h) = 2\sum_{i=1,2}\left[S^+_{f\tilde{f}i}\mathcal{I}_i - \left(\frac{m_f}{m_\chi}\right)\left(\Re(D_{f\tilde{f}i})\mathcal{J}_i + ih\Im(D_{f\tilde{f}i})\mathcal{K}_i\right)\right], \tag{4.9}$$

here again we use the shorthand notation

$$\begin{aligned} S^+_{f\tilde{f}i} &= \frac{1}{2}\left(|g^L_{\tilde{f}_i f 1}|^2 + |g^R_{\tilde{f}_i f 1}|^2\right) \\ D_{f\tilde{f}i} &= g^{R*}_{\tilde{f}_i f 1} g^L_{\tilde{f}_i f 1}. \end{aligned} \tag{4.10}$$

Because of the term $ih(\mathcal{K}_1-\mathcal{K}_2)\sin\varphi$, the probabilities of having $(++)$ and $(--)$ photon final states are not equal (note that $\mathcal{I}_i$, $\mathcal{J}_i$, and $\mathcal{K}_i$ are, in general, complex functions), which is a potentially measurable effect of CP violation. The coefficients $\mathcal{I}_i$, $\mathcal{J}_i$, and $\mathcal{K}_i$ are given by

$$\begin{aligned} \mathcal{I}_i &= \frac{m_i^2\, I_2(m_i,m_f)}{m_i^2-m_l^2} - \frac{2m_f^2\, I_1(m_f)}{m_i^2+m_\chi^2-m_f^2} + \frac{m_f^2(m_i^2-m_\chi^2-m_f^2)I_3(m_i,m_f)}{(m_i^2-m_f^2)(m_i^2+m_\chi^2-m_f^2)} \\ \mathcal{J}_i &= \frac{2m_\chi^2\,\left[I_1(m_f)-I_3(m_i,m_f)\right]}{m_i^2+m_\chi^2-m_f^2} \\ \mathcal{K}_i &= \frac{2(m_\chi^2-m_f^2)\,I_1(m_f)}{m_i^2+m_\chi^2-m_f^2} + \frac{2m_i^2\, I_2(m_i,m_f)}{m_i^2-m_f^2} - \frac{2m_i^2 m_\chi^2\, I_3(m_i,m_f)}{(m_i^2-m_f^2)(m_i^2+m_\chi^2-m_f^2)} \\ &\quad - \frac{2m_i^2}{m_i^2-m_\chi^2-m_f^2}\left[I_2(m_i,m_f)-I_1(m_i)\right], \end{aligned} \tag{4.11}$$

where m_i is the mass for the internal scalars (here we have adopted a simplified notation, $m_i \equiv m_{\tilde{f}_i}$ in the main text). We observe that if $m_1=m_2$, we have $(\mathcal{I}_1,\mathcal{J}_1,\mathcal{K}_1)=(\mathcal{I}_2,\mathcal{J}_2,\mathcal{K}_2)$ such that the amplitude will not vanish but it will depend neither on the mixing angle α nor on the CP-violation phase φ. If the integral $\mathcal{K}_1-\mathcal{K}_2$ is complex (which is the case for both the μ and τ channels), the amplitudes of the $(++)$ and $(--)$ final states do not have the same magnitude, which leads to an asymmetry ratio R as presented in Sec. 6.6. Here

I_1 and I_2 are the same as $2m_\chi^2 I_3^{[1]}$ and $2m_\chi^2 I_3^{[2]}$ in Ref. [210]. They are related to the standard three-point scalar loop integrals through

$$\begin{aligned}\frac{I_1(m_a)}{2m_\chi^2} &= C_0\left[0,0,4m_\chi^2,m_a^2,m_a^2,m_a^2\right]\\ \frac{I_2(m_a,m_b)}{2m_\chi^2} &= C_0\left[0,m_\chi^2,-m_\chi^2,m_a^2,m_a^2,m_b^2\right],\end{aligned} \tag{4.12}$$

in which we follow the convention of `LoopTools` [215]. The analytic expressions for $I_{1,2,3}$ are

$$\begin{aligned}I_1(m_a) &= \begin{cases} \frac{1}{4}\left[\log\left(\frac{1+\sqrt{1-m_a^2/m_\chi^2}}{1-\sqrt{1-m_a^2/m_\chi^2}}\right)+i\pi\right]^2 & m_a \le m_\chi \\ -\left[\arctan\sqrt{\frac{1}{m_a^2/m_\chi^2-1}}\right]^2 & m_a > m_\chi \end{cases}\\ I_2(m_a,m_b) &= \left[-\mathrm{Li}_2\left(\frac{m_a^2-m_b^2+m_\chi^2-\sqrt{\Delta_1}}{2m_a^2}\right)-\mathrm{Li}_2\left(\frac{m_a^2-m_b^2+m_\chi^2+\sqrt{\Delta_1}}{2m_a^2}\right)\right.\\ &\quad\left.+\mathrm{Li}_2\left(\frac{m_a^2-m_b^2-m_\chi^2-\sqrt{\Delta_2}}{2m_a^2}\right)+\mathrm{Li}_2\left(\frac{m_a^2-m_b^2-m_\chi^2+\sqrt{\Delta_2}}{2m_a^2}\right)\right]\\ I_3(m_a,m_b) &\equiv I_2(m_b,m_a),\end{aligned} \tag{4.13}$$

where

$$\begin{aligned}\Delta_1 &= (m_a^2-m_b^2-m_\chi^2)^2-4m_\chi^2m_b^2\\ \Delta_2 &= (m_a^2-m_b^2+m_\chi^2)^2+4m_\chi^2m_b^2\,.\end{aligned} \tag{4.14}$$

We note that both the $\mathcal{I}_i$ and $\mathcal{J}_i$ terms are contained in the analytic expression in Refs.[209, 210], but the $\mathcal{K}_i$ term is missing. Finally, we define the square of the total unpolarized amplitude as

$$|\mathcal{M}|^2 = \frac{1}{4}\sum_{s_1,s_2}\sum_{h_3,h_4}|\mathcal{A}|^2 = \frac{Q^4\alpha_{\rm EM}^2}{8\pi^2}\sum_{h=\pm1}|\mathscr{A}(h)|^2\,, \tag{4.15}$$

and the total cross section is

$$\langle\sigma v\rangle_{\gamma\gamma} = \frac{1}{2}\times\frac{|\mathcal{M}|^2}{32\pi m_\chi^2} = \frac{Q^4\alpha_{\rm EM}^2}{512\pi^3 m_\chi^2}\sum_{h=\pm1}|\mathscr{A}(h)|^2\,, \tag{4.16}$$

where the factor $1/2$ accounts for the fact that the final state consists of identical particles.

4.2.2 Numerical calculations

To ensure the accuracy of the results presented here, we perform a scan over the parameter space, conducted as follows. We first generate the analytic amplitudes for both

$\chi\chi \to \gamma\gamma$ and $\chi\chi \to \gamma Z$ using `FeynArts` [216], including left-right scalar mixing and a CP-violating phase. The numerical calculation is performed using `FormCalc` [215]. The package `LoopTools` is internally invoked by `FormCalc` to calculate the loop integrals involved in the amplitudes. However, since our initial state particles are at rest, we have $k_1 = k_2$. It is well known that if two external momenta are collinear, the Gram matrix becomes singular and the tensor loop integrals fail to be linearly independent.[1] For this reason, `FormCalc` breaks down for collinear external momenta, since `LoopTools` uses precisely the Gram matrix to derive higher-point and higher-rank integrals.

To circumvent this issue and arrive at a reliable result, we introduce a small relative velocity, so that the results of `LoopTools` remain stable. For example, we use a center-of-mass energy of $\sqrt{s} = 200.01\,\text{GeV}$ for $m_\chi = 100\,\text{GeV}$ in our numerical calculations. We have checked that the numerical error in the cross section is $\lesssim 1\%$ for annihilations to both $\gamma\gamma$ and $\bar{f}f$ (with scalar mixing), independent of the model parameters. For p-wave dominant cross sections, we perform a linear fit with respect to v^2 to find the coefficients a and b in the expansion $\sigma v = a + bv^2$. We have also checked that the error is $\lesssim 1\%$ in this scenario.

Analytic MSSM calculations of the annihilation cross section to $\gamma\gamma$ and γZ have been presented in Ref. [209–211] in the limit of no CP violation, and those expressions are consistent with the ones presented here. However, if $\varphi \neq 0$, then the amplitude of the $(++)$ photon helicity state will be different from that of the $(--)$ state, unlike the $\varphi = 0$ case. As we argued previously, the difference in the scattering amplitude is chirally suppressed by the fermion mass m_f,

$$\delta\mathcal{A} \sim \alpha_{\text{EM}} |\lambda_L \lambda_R| \sin(2\alpha) \sin\varphi \left(\frac{m_f}{m_\chi}\right), \tag{4.17}$$

a term which does not appear previously in the literature.

In order for CP violation to yield differing cross sections for the $(++)$ and $(--)$ final photon states, it is necessary for $m_f < m_\chi$. If $m_f > m_\chi$, then the CP-violating part of the amplitude is purely imaginary as a result of the optical theorem, and CP conjugation of the matrix element is equivalent to complex conjugation. But if $m_f < m_\chi$, then the intermediate states of the one-loop diagram can go on shell, providing an imaginary component

[1] This leads to the reduction of all the four-point loop integrals that appear in the $\gamma\gamma$ amplitude to three-point scalar loop integrals. For a comprehensive review on the calculation techniques of general tensor loop integrals, see Ref. [217].

to the CP-conserving matrix element, which is necessary for a nontrivial asymmetry. On the other hand, if $m_f > m_\chi$, then the only final states that are kinematically allowed are $\gamma\gamma$ and γZ. In this kinematic regime, if the couplings $\lambda_{L,R}$ are large, these final states will be most easily observable.

4.3 Internal bremsstrahlung

The IB process $\chi\chi \to \bar{f}f\gamma$ can in general produce a steplike feature in the photon spectrum at $E_\gamma \approx m_\chi$ as a consequence of 3-body kinematics. We can separate the IB amplitude into two (not gauge invariant) parts as in Ref. [212]: virtual internal bremsstrahlung (VIB) for the photon attached to the internal scalar propagator and final state radiation (FSR) for the photon attached to the external fermion lines. The full IB amplitude can then be written

$$\mathcal{A}_{\rm IB} = \mathcal{A}_{\rm VIB} + \mathcal{A}_{\rm FSR}\,. \tag{4.18}$$

From $\mathcal{A}_{\rm IB}$, the total differential cross section can be calculated by

$$\frac{d\,\langle\sigma v\rangle_{\rm IB}}{dx} = \frac{x}{512\pi^4}\sqrt{1-\frac{m_f^2}{m_\chi^2(1-x)}}\int d\Omega_{34}\overline{|\mathcal{A}_{\rm IB}|^2}\,, \tag{4.19}$$

where $d\Omega_{34}$ is the integration over the fermions' direction in the fermion pair center-of-mass frame, and $\overline{|\mathcal{A}_{\rm IB}|^2}$ is the squared amplitude with initial spin averaged and final spin summed.

The photon spectrum can exhibit different features depending on the degree of chiral symmetry breaking. If there is no mixing between the scalars associated with the left- and right-handed fermions, there may be a hard peak at the end of the IB spectrum, which can be significant if the dark matter and $\tilde{f}_1$ are nearly degenerate [213]. This can be understood as following: if 2-body annihilation $\chi\chi \to \bar{f}f$ is helicity suppressed, the emission of an additional spin 1 boson from the virtual scalars can lift the suppression. Therefore, we see the production of a fermion and antifermion with opposite helicities, arising from the same Weyl spinor, with the remaining angular momentum carried by the vector boson. This process can be the dominant contribution to the total annihilation in certain cases, even though it is suppressed by $\alpha_{\rm EM}$ and $(m_\chi/m_{\tilde{f}_1})^8$ due to the additional internal scalar propagator. In contrast, the presence of scalar mixing enhances the 2-body

annihilation, which enhances the FSR photon collinear to one of the fermions. In this case FSR dominates IB and the total IB spectrum is fairly flat relative to the case with no mixing.

To illustrate these arguments, we rewrite the total IB amplitude $\mathcal{A}_{\rm IB}$ in terms of three gauge invariant subamplitudes,

$$\mathcal{A}_{\rm IB} = \frac{iQe}{2}\left[\frac{\overline{u}(k_1)\gamma^5 v(k_2)}{2m_\chi}\right]\left(\mathcal{A}_{\rm vb} + \mathcal{A}_{\rm mix} + \mathcal{A}_{m_f}\right), \tag{4.20}$$

where again $k_{1,2}$ are the momenta of the two dark matter particles. The first term, $\mathcal{A}_{\rm vb}$, which refers to chirality flip due to a vector boson, survives in both the massless fermion limit ($m_f \to 0$) and the no-mixing limit ($\alpha = 0$). If we denote the photon momentum and polarization as k_5 and ϵ_5, and the outgoing fermion (antifermion) momentum by $k_{3(4)}$, this amplitude can be written as

$$\mathcal{A}_{\rm vb} = \sum_{i=1,2} \overline{u}(k_3)\,\mathcal{O}_i(|g^R_{\tilde{f}_i f 1}|^2 P_L - |g^L_{\tilde{f}_i f 1}|^2 P_R)v(k_4). \tag{4.21}$$

The matrices $\mathcal{O}_i$ are given by

$$\mathcal{O}_i \equiv \gamma_\mu\left[\frac{k_5^\mu (k_3-k_4)\cdot\epsilon_5 - \epsilon_5^\mu (k_3-k_4)\cdot k_5}{(s_3 - m^2_{\tilde{f}_i})(s_4 - m^2_{\tilde{f}_i})}\right], \tag{4.22}$$

with $s_3 \equiv (k-k_3)^2$ and $s_4 \equiv (k-k_4)^2$. When $m_f = 0$, the cross section due solely to $\mathcal{A}_{\rm vb}$ is

$$\begin{aligned}\frac{d\langle\sigma v\rangle_{\rm vb}}{dx} = \frac{Q^2\alpha_{\rm EM}(1-x)}{64\pi^2 m_\chi^2}\sum_{i=1,2}\left(S^-_{f\tilde{f}i}\right)^2 \\ \times\left[\frac{4x}{(1+\mu_i)(1+\mu_i-2x)} - \frac{2x}{(1+\mu_i-x)^2}\right. \\ \left. -\frac{(1+\mu_i)(1+\mu_i-2x)}{(1+\mu_i-x)^3}\log\frac{1+\mu_i}{1+\mu_i-2x}\right],\end{aligned} \tag{4.23}$$

where $S^-_{f\tilde{f}i} = \left(|g^L_{\tilde{f}_i f 1}|^2 - |g^R_{\tilde{f}_i f 1}|^2\right)/2$, $\mu_i \equiv m^2_{\tilde{f}_i}/m^2_\chi$, and $x \equiv E_\gamma/m_\chi$ is the photon energy fraction.

In the limit $\alpha = 0$, we have $\mathcal{A}_{\rm IB} \sim \mathcal{A}_{\rm vb}$, and we recover the well-known result given, for example, in Ref. [212, 218]. Note that if $\mu_i \sim 1$, the photon spectrum shows a very sharp peak near $x \approx 1$. This enhancement arises in the limit where an outgoing fermion becomes soft; if the dark matter and the scalar are nearly degenerate, then one intermediate scalar propagator goes on shell. The total cross section in the $\alpha, m_f/m_\chi \to 0$ limit is finite:

$$\begin{aligned}\langle\sigma v\rangle_{\rm vb} = \frac{Q^2\alpha_{\rm EM}}{64\pi^2 m_\chi^2}\sum_{i=1,2}\left(S^-_{f\tilde{f}i}\right)^4\left\{(\mu_i+1)\left[\frac{\pi^2}{6} - \log^2\left(\frac{\mu_i+1}{2\mu_i}\right) - 2\mathrm{Li}_2\left(\frac{\mu_i+1}{2\mu_i}\right)\right]\right. \\ \left. + \frac{4\mu_i+3}{\mu_i+1} + \frac{4\mu_i^2-3\mu_i-1}{2\mu_i}\log\left(\frac{\mu_i-1}{\mu_i+1}\right)\right\}.\end{aligned} \tag{4.24}$$

If $\mu_i - 1 \ll 1$, the combination in the curly brackets approaches a constant, $(7/2) - (\pi^2/3)$; if $\mu_i \gg 1$, it behaves as $4/(15\mu_i^4)$.

When $\alpha \neq 0$, there is another contribution to the s-wave amplitude arising from mixing,

$$\mathcal{A}_{\rm mix} = 2m_\chi \sum_{i=1,2} \overline{u}(k_3) \left[\Re(D_{f\tilde{f}i})\gamma^5 - i\Im(D_{f\tilde{f}i}) \right] (\mathcal{V}_i + \mathcal{S}_i) v(k_4), \tag{4.25}$$

where $D_{f\tilde{f}i} = g^{R*}_{\tilde{f}_i f 1} g^L_{\tilde{f}_i f 1}$, and the matrices $\mathcal{V}_i$ and $\mathcal{S}_i$ are given by

$$\begin{aligned}
\mathcal{V}_i &\equiv -\frac{i}{2}\sigma_{\mu\nu} k_5^\mu \epsilon^\nu \left[\frac{1}{(k_3\cdot k_5)(s_4 - m^2_{\tilde{f}_i})} + \frac{1}{(k_4\cdot k_5)(s_3 - m^2_{\tilde{f}_i})} \right] \\
\mathcal{S}_i &\equiv \frac{(k_3 - k_4)\cdot \epsilon_5}{(s_3 - m^2_{\tilde{f}_i})(s_4 - m^2_{\tilde{f}_i})} \\
&\quad + \left[\frac{k_3\cdot\epsilon_5}{(k_3\cdot k_5)(s_4 - m^2_{\tilde{f}_i})} - \frac{k_4\cdot\epsilon_5}{(k_4\cdot k_5)(s_3 - m^2_{\tilde{f}_i})} \right] .
\end{aligned} \tag{4.26}$$

The last piece, $\mathcal{A}_{m_f}$, is proportional to the fermion mass, m_f,

$$\mathcal{A}_{m_f} = -m_f \sum_{i=1,2} \overline{u}(k_3)\gamma^5 S^+_{f\tilde{f}i} (\mathcal{V}_i + \mathcal{S}_i) v(k_4), \tag{4.27}$$

where $S^+_{f\tilde{f}i} = \left(|g^L_{\tilde{f}_i f 1}|^2 + |g^R_{\tilde{f}_i f 1}|^2 \right)/2$. Both $\mathcal{A}_{\rm mix}$ and $\mathcal{A}_{m_f}$ are contributions to the amplitude for producing a fermion and antifermion with the same helicity, where the mixing between Weyl spinors arises from either the nonvanishing mixing angle or the fermion mass term. Comparing with the separation in Eq. (4.18), we find that $\mathcal{A}_{\rm vb}$ contains the entire $\mathcal{A}_{\rm VIB}$ and part of $\mathcal{A}_{\rm FSR}$, while $\mathcal{A}_{\rm mix}$ and $\mathcal{A}_{m_f}$ receive contributions only from $\mathcal{A}_{\rm FSR}$.

Each term in the matrix element can be written as the contraction of a spinor product, with some Lorentz structure, and some function of the momenta. $\mathcal{A}_{\rm vb}$ contains spinor products with vector and axial vector Lorentz structure. The CP-conserving parts of $\mathcal{A}_{\rm mix}$ contain spinor products with scalar and tensor Lorentz structures, while the CP-violating parts contain spinor products with pseudoscalar and tensor Lorentz structures. We do not present the complete differential scattering cross section due to its lengthy expression. However, the spinor products can be found, for example, in Ref. [219], allowing one to evaluate the entire expression.

We note also that each of these terms ($\mathcal{A}_{\rm vb}$, $\mathcal{A}_{\rm mix}$, and $\mathcal{A}_{m_f}$) is suppressed at most by $\sin 2\alpha$ or m_f/m_χ, but not by both. Thus, we expect CP-violating contributions to

bremsstrahlung processes to be subleading, as they are doubly suppressed. Indeed, our explicit calculation verifies that this effect is small.

The lowest order calculation yields a well-known apparent divergence[2] in the cross section for emitting soft or collinear photons via final state radiation, arising from a nearly on-shell fermion propagator. In both the soft and collinear limits, we have $s_3 \approx s_4 \approx -m_\chi^2$, and the only divergent quantity is

$$\mathcal{S}_i + \mathcal{V}_i \to -\left(\frac{\not{\epsilon}_5 \not{k}_5 + 2k_3\cdot\epsilon_5}{2k_3\cdot k_5} - \frac{\not{k}_5\not{\epsilon}_5 + 2k_4\cdot\epsilon_5}{2k_4\cdot k_5}\right)\frac{1}{m_\chi^2 + m_{\tilde{f}_i}^2}\,. \tag{4.28}$$

In particular, for the soft limit, we can further neglect the $\not{k}_5$ in the numerator and get the correct factorization behavior,

$$\mathcal{A}_{\text{IB}} \xrightarrow{\text{soft}} -Qe\left(\frac{k_3\cdot\epsilon_5}{k_3\cdot k_5} - \frac{k_4\cdot\epsilon_5}{k_4\cdot k_5}\right)\mathcal{A}_{\text{2-b}}\,, \tag{4.29}$$

where

$$\mathcal{A}_{\text{2-b}} = \frac{i}{2}m_\chi\left(\frac{\overline{u}(k_1)\gamma^5 v(k_2)}{2m_\chi}\right)\overline{u}(k_3)\left[\Re(\Xi_2)\gamma^5 - i\Im(\Xi_2)\right]v(k_4). \tag{4.30}$$

This leads to the Sudakov log enhancement of the probability for photon emission from final state radiation,

$$\langle\sigma v\rangle_{\text{IB}} \sim \frac{Q^2\alpha_{\text{EM}}}{\pi}\log\left(\frac{s}{E_{th}^2}\right)\log\left(\frac{s}{m_f^2}\right)\times\langle\sigma v\rangle_{\bar{f}f}\,, \tag{4.31}$$

where $s = 4m_\chi^2$ and we have kept only the leading logarithmic enhancement. The first logarithm is the soft photon enhancement, which is cut off by E_{th}, the energy threshold of the photon detector. The second logarithm is the collinear photon enhancement and is cut off by the mass of the fermion. More generally, if the photon is collinear but not necessarily soft, we obtain

$$\frac{d\langle\sigma v\rangle_{\text{IB}}}{dx} \sim \frac{Q^2\alpha_{\text{EM}}}{\pi}\frac{(1-x)^2+1}{x}\log\frac{s(1-x)}{m_f^2}\times\langle\sigma v\rangle_{\bar{f}f} \tag{4.32}$$

from Eq. (4.29), which of course is widely acknowledged as the Weizsäcker-Williams formula. The soft and collinear enhancements thus have little effect on the spectrum as $m_f/m_\chi \to 0$ and $\alpha \to 0$, in which case $\langle\sigma v\rangle_{\bar{f}f} \to 0$. But if $\alpha \neq 0$, then the collinear

[2]This so-called collinear divergence is not physical, since it disappears once higher order and loop corrections are included.

enhancement will have a large effect; one cannot strictly take the $m_f/m_\chi \to 0$ limit, as the nonzero fermion mass cuts off the collinear divergence.

There has been a variety of past work on the spectrum of the $\chi\chi \to \bar{f}f\gamma$ process, and this spectrum is well known in two limits:

(i) $\alpha = 0$, $m_f/m_\chi \to 0$: This corresponds to the case where the process $\chi\chi \to \bar{f}f$ is suppressed, and the dominant process is $\chi\chi \to \bar{f}f\gamma$, yielding a hard spectrum which is dominated by $\mathcal{A}_{\rm vb}$. The soft and collinear emission of photons via FSR has little effect on the spectrum.

(ii) $\alpha = \mathcal{O}(1)$, $m_f/m_\chi \to 0$: In this case, the $\chi\chi \to \bar{f}f$ cross section is unsuppressed, and the dominant contribution to $\chi\chi \to \bar{f}f\gamma$ arises from FSR in the soft and collinear regimes. Here, the details of the interaction are not very important; provided the $\chi\chi \to \bar{f}f$ cross section is unsuppressed, the dominant contribution to $\chi\chi \to \bar{f}f\gamma$ arises from a simple rescaling of the $2 \to 2$ cross section by the Sudakov log factor.

So how about the spectrum in the regime of intermediate α? How can we interpolate between these two limits? If the lightest scalar mediator $\tilde{f}_1$, is much lighter than the heavier scalar, $\tilde{f}_2$, one expects the crossover between these behaviors to occur roughly when

$$\tan^2\alpha \times |\lambda_R/\lambda_L|^2 (m_{\tilde{f}_1}/m_\chi)^4 \log(m_\chi^2/m_f^2) \sim \mathcal{O}(1)\,, \tag{4.33}$$

which corresponds to the point where the suppression of soft FSR due to the small mixing angle is roughly canceled by the enhancement for collinear emission. Note that one expects the hard IB signal to dominate over $2 \to 2$ scattering provided

$$\tan^2\alpha \times |\lambda_R/\lambda_L|^2 (m_{\tilde{f}_1}/m_\chi)^4 < \alpha_{\rm EM}\,. \tag{4.34}$$

We present the results of our calculations in Sec. 6.6.

4.3.1 The analytic expression for the IB cross section

In the nonrelativistic ($v \to 0$) and vanishing lepton mass ($\epsilon = m_f/m_\chi \to 0$) limits, the full analytical expression for the IB cross section at the lowest order is given by

$$d\,\langle\sigma v\rangle_{\rm IB} = \frac{1}{4}\sum_{\rm spins}\left|\mathcal{M}^{NR}\right|^2 \frac{Q^2\alpha_{EM}}{128\pi^2 E_1 E_2} dE_3 dE_5, \tag{4.35}$$

where $E_{1,2}$ are the energies of the DM particles, E_3 is the energy carried by one of the outgoing leptons, and E_5 is that of photon. Defining the outgoing momenta of the leptons, $k_{3,4}$, and that of photon, k_5, as

$$\begin{aligned} k_3^\mu &= \left[E_3, \sqrt{E_3^2 - m_\ell^2}\cos\theta_{35}, \sqrt{E_3^2 - m_\ell^2}\sin\theta_{35}, 0\right] \\ k_4^\mu &= \left[E_4, \sqrt{E_4^2 - m_\ell^2}\cos\theta_{45}, \sqrt{E_4^2 - m_\ell^2}\sin\theta_{45}, 0\right] \\ k_5^\mu &= [E_5, E_5, 0, 0]\,, \end{aligned} \tag{4.36}$$

the spin-averaged matrix is given by

$$\sum_{\text{spins}} \left|\mathcal{M}^{NR}\right|^2 = \sum_{\text{spins}} \left|\mathcal{M}^{NR}_{RR}\right|^2 + \sum_{\text{spins}} \left|\mathcal{M}^{NR}_{LL}\right|^2 + \sum_{\text{spins}} \left|\mathcal{M}^{NR}_{LR}\right|^2, \tag{4.37}$$

where

$$\begin{aligned} \frac{1}{4}\sum_{\text{spins}} \left|\mathcal{M}^{NR}_{RR}\right|^2 &= \sum_{i,j=1,2} |g^R_{\tilde{\ell}_i f 1}|^2 |g^R_{\tilde{\ell}_j f 1}|^2 (D_3 D_4)_i (D_3 D_4)_j (k_3\cdot k_4)\left[(k_3\cdot k_5)^2 + (k_4\cdot k_5)^2\right] \\ \frac{1}{4}\sum_{\text{spins}} \left|\mathcal{M}^{NR}_{LL}\right|^2 &= \sum_{i,j=1,2} |g^L_{\tilde{\ell}_i f 1}|^2 |g^L_{\tilde{\ell}_j f 1}|^2 (D_3 D_4)_i (D_3 D_4)_j (k_3\cdot k_4)\left[(k_3\cdot k_5)^2 + (k_4\cdot k_5)^2\right] \\ \frac{1}{4}\sum_{\text{spins}} \left|\mathcal{M}^{NR}_{LR}\right|^2 &= 4m_\chi^2 \sum_{i,j=1,2} \left(\Re(g^R_{\tilde{\ell}_i \ell 1} g^{L^*}_{\tilde{\ell}_i \ell 1})\Re(g^R_{\tilde{\ell}_j \ell 1} g^{L^*}_{\tilde{\ell}_j \ell 1}) + \Im(g^R_{\tilde{\ell}_i \ell 1} g^{L^*}_{\tilde{\ell}_i \ell i})\Im(g^R_{\tilde{\ell}_j \ell 1} g^{L^*}_{\tilde{\ell}_j \ell 1})\right) \\ &\qquad \times [\mathcal{A}_{ij} + \mathcal{B}_{ij} + \mathcal{C}_{ij}]. \end{aligned} \tag{4.38}$$

In the last line, $\mathcal{A}$ is due to FSR, $\mathcal{B}$ is from interference between FSR and VIB, and $\mathcal{C}$ is from VIB, respectively, each of which are given explicitly by

$$\begin{aligned} \mathcal{A}_{ij} &= \frac{(k_3\cdot k_5)}{(k_4\cdot k_5)} D_{3i} D_{3j} + \left[1 + \frac{(k_3\cdot k_4)}{(k_3\cdot k_5)} + \frac{(k_3\cdot k_4)}{(k_4\cdot k_5)} + \frac{(k_3\cdot k_4)^2}{(k_3\cdot k_5)(k_4\cdot k_5)}\right] D_{3i} D_{4j} + (3 \leftrightarrow 4) \\ \mathcal{B}_{ij} &= (k_3\cdot k_4) D_{3i} D_{4i}\left[\left(\frac{2m_\chi^2}{(k_3\cdot k_5)} - 1\right) D_{4j} + \left(\frac{2m_\chi^2}{(k_4\cdot k_5)} - 1\right) D_{3j}\right] + (i \leftrightarrow j) \\ \mathcal{C}_{ij} &= 2(k_3\cdot k_4)^2 D_{3i} D_{4i} D_{3j} D_{4j}, \end{aligned} \tag{4.39}$$

where $D_{ij}^{-1} = [(k_i - m_\chi)^2 - m^2_{\tilde{\ell}_j}]^2$ is the propagator of the intermediate slepton. Note also that all other interference terms of $\mathcal{M}^{NR}_{RR}$ or $\mathcal{M}^{NR}_{LL}$ with $\mathcal{M}^{NR}_{LR}$ vanish.

The integration of Eq. (4.35) over E_3 requires special care since the expression above, Eq. (4.39) in particular, has collinear divergences in the massless lepton limit. To find the correct integral limits which do not include the singularity, we first rewrite E_3 and E_5 in

dimensionless variables, $x = E_3/m_\chi$, and $y = E_5/m_\chi$. Working out the 3-body phase space including the non-zero mass, we find the maximum/minimum of x is

$$x = \frac{(1-y)(2-y) \pm \sqrt{(1-y)^2(2-y)^2 - (1-y)[4(1-y)^2 + \epsilon^2 y^2]}}{2(1-y)}, \tag{4.40}$$

where y ranges from 0 to $1-\epsilon^2$.

4.3.2 The IB spectrum from radiative scalar decay

So far, we have discussed the general features of the IB spectrum and cross section for DM annihilation. In this section, however, we will find the photon spectrum for radiative decay of a neutral scalar boson into a fermion pair for later use. Here we suppose a hypothetical neutral scalar boson, ϕ, interacts with the SM fermion, f, via,

$$\mathcal{L}_{\rm int} = -g\phi\bar{f}f, \tag{4.41}$$

where g is the coupling constant. The lowest order decay rate for this process is given by

$$\Gamma_0 = \frac{g^2}{32\pi} m_\phi \left(1 - \frac{4m_f^2}{m_\phi^2}\right)^{\frac{3}{2}}, \tag{4.42}$$

where m_ϕ is the neutral scalar mass. Note that contrary to the case of DM annihilation, the photon emission is only due to FSR in this case. The photon spectrum, to lowest order, is

$$\begin{aligned}\frac{dN}{dx} &= \frac{1}{\Gamma_0}\frac{d\Gamma_{\rm IB}}{dx} \\ &= \frac{Q^2\alpha_{\rm EM}}{4\pi}\left(1 - \frac{4m_f^2}{m_\phi^2}\right)^{-\frac{3}{2}} \int_{x_{\rm min}}^{x_{\rm max}} dx(\mathcal{T}_0 + \mathcal{T}_1 + \mathcal{T}_2).\end{aligned} \tag{4.43}$$

Here $\mathcal{T}_i$ are defined as

$$\begin{aligned}\mathcal{T}_0 &= 2\left[\frac{(k_4\cdot k_5)}{(k_3\cdot k_5)} + \frac{(k_3\cdot k_5)}{(k_4\cdot k_5)} + \frac{m_\phi^2(k_3\cdot k_4)}{(k_3\cdot k_5)(k_4\cdot k_5)} + 2\right] \\ \mathcal{T}_1 &= m_\ell^2\left[\frac{(4k_3\cdot k_5 - m_\phi^2)}{(k_3\cdot k_5)^2} + \frac{(4k_4\cdot k_5 - m_\phi^2)}{(k_4\cdot k_5)^2} - \frac{2(m_\phi^2 + 2k_3\cdot k_4)}{(k_3\cdot k_5)(k_4\cdot k_5)}\right] \\ \mathcal{T}_2 &= 4m_\ell^4\left[\frac{1}{(k_3\cdot k_5)^2} + \frac{1}{(k_4\cdot k_5)^2} + \frac{1}{(k_3\cdot k_5)(k_4\cdot k_5)}\right],\end{aligned} \tag{4.44}$$

where $k_{3,4,5}$ are defined by Eq. (4.36), and $x_{\rm min}$ and $x_{\rm max}$ are given by Eq. (4.40).

In the light fermion limit, $\epsilon \ll 1$,

$$x_{\rm min} = 1 - y + \frac{y}{4(1-y)}\epsilon^2 + \mathcal{O}(\epsilon^4)$$

$$x_{\max} = 1 - \frac{y}{4(1-y)}\epsilon^2 + \mathcal{O}(\epsilon^4), \tag{4.45}$$

and we see that the photon multiplicity, at leading order, reduces to

$$\begin{aligned}\frac{dN}{dx} &= \frac{Q^2\alpha_{\mathrm{EM}}}{4\pi}\frac{2-2y+y^2}{y}\left[\ln\left|\frac{x+y-1}{1-x}\right|\right]_{x_{\min}}^{x_{\max}} + \mathcal{O}(\epsilon^2) \\ &= \frac{Q^2\alpha_{\mathrm{EM}}}{2\pi}\frac{2-2y+y^2}{y}\ln\left|\frac{-\epsilon^2+4(1-y)}{\epsilon^2}\right| + \mathcal{O}(\epsilon^2),\end{aligned} \tag{4.46}$$

which can be seen in the Weizsäcker-Williams approximation.

CHAPTER 5

SM LEPTON DIPOLE MOMENTS

Large chiral mixing angle and *CP*-violating phase induce large dipole moments of the Standard Model leptons due to chiral symmetry breaking. We find that stringent constraints on these parameters come from precise measurements of the magnetic dipole moments of the SM leptons, which also strongly constrain the *s*-wave annihilation cross section of DM into lepton pairs.

5.1 A correction to the SM lepton dipole moments

If ℓ is a charged lepton, then the interaction given in Eq. (2.4) will induce a correction to the lepton dipole moments due to chiral symmetry breaking. The interaction with an external EM field A_μ and lepton is, in general, given by a fermion bilinear $\bar{\ell}\Gamma^\mu \ell A_\mu$, where the vertex Γ_μ is characterized by the EM form factors,

$$\Gamma_\mu = F(q^2)\gamma_\mu + M(q^2)\sigma_{\mu\nu}q^\nu + E(q^2)\sigma_{\mu\nu}q^\nu\gamma_5 + A(q^2)(q^2\gamma_\mu - \not{q}q_\mu)\gamma_5, \tag{5.1}$$

where F, M, E, and A denote the normal magnetic, anomalous magnetic and electric dipole, and anapole form factors, respectively. Here the bilinears with $\sigma_{\mu\nu}$ and $\sigma_{\mu\nu}q^\nu\gamma_5$, corresponding to anomalous electromagnetic moment operators, are chiral symmetry violating.

In our scenario, a contribution to the electric or magnetic dipole moments of the Standard Model leptons can arise from one-loop vertex correction diagrams with the bino and sleptons running in the loop, as shown in Figure 5.1. Because the dipole moment operators flip the lepton helicity, the contributions to the dipole moments from the bino-slepton loops

---

This chapter is adapted from published articles: Phys. Rev. D **90**, *095007 (2014). MSSM Dark Matter and a Light Slepton Sector: The Incredible Bulk. K. Fukushima, C. Kelso, J. Kumar, P. Sandick, T. Yamamoto.* ©*Owned by the authors, published by American Physical Society, 2014. and Phys. Rev. D* **94**, *015022 (2016). Gamma-Ray Signals from Dark Matter Annihilation via Charged Mediators. J. Kumar, P. Sandick, F. Teng, T. Yamamoto.* ©*Owned by the authors, published by American Physical Society, 2016. With kind permission of the American Physical Society.*

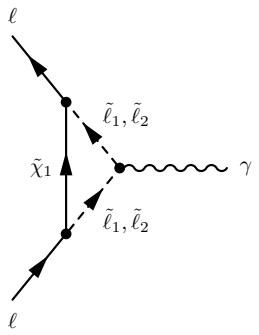

Figure 5.1. Feynman diagram for the one-loop vertex correction.

can be large if L-R slepton mixing is large. But the electric dipole moment can only receive a non-vanishing contribution if the CP-violating phase φ is nonzero.

The expressions for the corrections to the magnetic and electric dipole moments are

$$\begin{aligned} \delta a_\ell &= \sum_{i=1,2} \frac{m_\ell m_\chi}{8\pi^2 m^2_{\tilde{\ell}_i}} \Re(D_{f\tilde{f}i}) Q_{\tilde{\ell}_i} B(r_i) + \sum_{i=1,2} \frac{m^2_\ell}{4\pi^2 m^2_{\tilde{\ell}_i}} S^+_{f\tilde{f}i} Q_{\tilde{\ell}_i} \mathcal{B}(r_i) \\ \frac{2d_\ell}{e} &= \sum_{i=1,2} \frac{m_\ell m_\chi}{8\pi^2 m^2_{\tilde{\ell}_i}} \Im(D_{f\tilde{f}i}) Q_{\tilde{\ell}_i} B(r_i), \end{aligned} \tag{5.2}$$

where $Q_{\tilde{\ell}_i}$ is the electric charge of $\tilde{\ell}_i$, $r_i = m^2_\chi / m^2_{\tilde{\ell}_i}$ and

$$\begin{aligned} B(r) &= \frac{1}{2(1-r)^2}\left(1 + r + \frac{2r\ln r}{1-r}\right) \\ \mathcal{B}(r) &= \frac{1}{12(1-r)^3}\left(1 - 5r - 2r^2 - \frac{6r^2\ln r}{1-r}\right). \end{aligned} \tag{5.3}$$

$B(r)$ behaves at $r \approx 1$ as

$$B(r) \approx \frac{1}{6} + \frac{1-r}{12} + \frac{1}{20}(1-r)^2 + \mathcal{O}\left((1-r)^3\right). \tag{5.4}$$

In the limit $m_\ell \to 0$, the contributions to the anomalous magnetic moment, $a = (g-2)/2$, and the electric dipole moment, $d/|e|$, of the associated lepton due to new physics are [220]

$$\begin{aligned} \Delta a &= \frac{m_\ell m_{\tilde{\chi}}}{4\pi^2 m^2_{\tilde{\ell}_1}} g^2 Y_L Y_R \cos\varphi \cos\alpha \sin\alpha \left[\frac{1}{2(1-r_1)^2}\left(1 + r_1 + \frac{2r_1\ln r_1}{1-r_1}\right)\right] - (\tilde{\ell}_1 \to \tilde{\ell}_2) \\ \frac{d}{|e|} &= \frac{m_\chi}{8\pi^2 m^2_{\tilde{\ell}_1}} g^2 Y_L Y_R \sin\varphi \cos\alpha \sin\alpha \left[\frac{1}{2(1-r_1)^2}\left(1 + r_1 + \frac{2r_1\ln r_1}{1-r_1}\right)\right] \\ &\quad -(\tilde{\ell}_1 \to \tilde{\ell}_2), \end{aligned} \tag{5.5}$$

where $r_i \equiv m^2_\chi / m^2_{\tilde{\ell}_i}$. Since charginos are assumed to be very heavy, diagrams with charginos and sneutrinos in the loop do not contribute.

5.2 The relation between dipole moments and the annihilation cross section

Because dark matter annihilation from an $L = 0$ initial state also requires a lepton helicity flip, one may relate the s-wave part of the $\chi\chi \to \ell^+\ell^-$ annihilation cross section to induced corrections to the electric and magnetic dipole moments of ℓ. In particular, in the limit where the r_i are small, we find

$$\begin{aligned} c_0 &\sim 32\pi^3 \left[(\Delta a_\ell)^2 + \left(\frac{2 m_\ell d_\ell}{|e|} \right)^2 \right] m_\ell^{-2} + \mathcal{O}(r_i) \\ &\sim 3.9 \times 10^{11} \text{pb} \left[(\Delta a_\ell)^2 + \left(\frac{2 m_\ell d_\ell}{|e|} \right)^2 \right] \left(\frac{m_\ell}{\text{GeV}} \right)^{-2}. \end{aligned} \tag{5.6}$$

This relation is similar to that found for scalar dark matter, as anticipated in Ref. [221]. However, c_0 is maximized for $r_i \sim 1$, $r_{j \neq i} \to 0$. In this limit, we find

$$\begin{aligned} c_0 &\sim 72\pi^3 \left[(\Delta a_\ell)^2 + \left(\frac{2 m_\ell d_\ell}{|e|} \right)^2 \right] m_\ell^{-2} + \mathcal{O}\left((1 - r_i)^2 \text{ or } r_j \right) \\ &\sim 8.7 \times 10^{11} \text{pb} \left[(\Delta a_\ell)^2 + \left(\frac{2 m_\ell d_\ell}{|e|} \right)^2 \right] \left(\frac{m_\ell}{\text{GeV}} \right)^{-2}. \end{aligned} \tag{5.7}$$

CHAPTER 6

RESULTS AND CONSTRAINTS ON MODEL

In this chapter, we present the results of calculations discussed in the preceding chapters, and place limits on our model parameter space using observations and experimental data. We find our model is viable, especially if DM primarily couples to μ and/or τ. The possible observable signatures will also be discussed in this chapter, including the gamma-ray spectra and the polarization of monochromatic gamma-rays.

6.1 Sparticle mass limits

Null searches for supersymmetric particles imply a lower limit of 780 GeV for light degenerate first and second generation squarks [222]. Constraints on squark masses in CMSSM are even more stringent, and exclude squarks below 1.7 TeV for certain benchmark models [222, 223]. If we relax some unification constraints imposed in the CMSSM at the grand unified theory scale, then it has been shown that the MSSM-9 model [224, 225] can contain a $\sim$ 1 TeV Higgsino LSP or a $\sim$ 3 TeV wino LSP, which are viable thermal dark matter candidates satisfying the relic density.

On the other hand, the current limit on the mass of any slepton is much weaker. We still have the possibility that heavy squarks provide the necessary loop corrections to the mass of the SM-like Higgs while light sleptons provide the main dark matter annihilation channel.

The current mass limits for supersymmetric particles are summarized by the Particle Data Group [5]. The limits (under some minimal assumptions) that the right-handed scalar particles must satisfy are: selectrons must be heavier than 107 GeV; smuons must be heav-

---

This chapter is adapted from published articles: Phys. Rev. D **90**, *095007 (2014). MSSM Dark Matter and a Light Slepton Sector: The Incredible Bulk. K. Fukushima, C. Kelso, J. Kumar, P. Sandick, T. Yamamoto.* ©*Owned by the authors, published by American Physical Society, 2014. and Phys. Rev. D* **94**, *015022 (2016). Gamma-Ray Signals from Dark Matter Annihilation via Charged Mediators. J. Kumar, P. Sandick, F. Teng, T. Yamamoto.* ©*Owned by the authors, published by American Physical Society, 2016. With kind permission of the American Physical Society.*

ier than 94 GeV; staus must be heavier than 82 GeV; and sneutrinos must be heavier than 94 GeV. In addition, the LHC has placed bounds on these particles through searches for their direct production. Limits on the slepton mass (both left and right handed selectrons and smuons) are presented by the ATLAS collaboration in Ref. [226]. A left handed slepton with a mass of 170 GeV to 300 GeV is excluded at 95% CL for a neutralino mass of 100 GeV. A right-handed slepton is still unconstrained for a neutralino mass of 100 GeV. The CMS collaboration also performs a similar search with slightly weaker results, although they only provide limits for the left-handed sleptons [227]. LEP experiments only put a lower limit at $\sim 100\,\text{GeV}$ [228–231], while the LHC 8 TeV run has excluded left-handed sleptons below 310 GeV and right-handed sleptons below 235 GeV, assuming a massless bino LSP [232, 233]. For a massive bino LSP with mass m_χ, a new allowed region opens up for sleptons lighter than approximately $m_\chi + 80\,\text{GeV}$ [234, 235]. The LHC 14 TeV run has the potential to push the upper exclusion limit to as high as 900 GeV (for a Higgsino LSP) but cannot move the lower exclusion limit [236].

Although these constraints are phrased as bounds on scalar superpartners, the lesson is more general: LHC constraints place tight bounds on colored scalars but weaker bounds on QCD-neutral scalars. As we are considering significant mixing, these LHC limits can only be used as guidelines since a dedicated analysis including the effects of mixing would be required, which is beyond the scope of this work.

6.2 Dipole moment constraints

In Table 6.1, we present the most recent measurements of the anomalous magnetic moments and electric dipole moments of the SM-charged leptons [5, 237–243], along with the expectations for the anomalous magnetic moments within the SM. The leading order contributions to the electric dipole moments of the charged leptons within the SM occur only at more than three loops [244], and are many orders of magnitude below the current constraints.

The 2σ ranges for the anomalous magnetic moments of the SM charged leptons are

$$\begin{aligned} -2.66 \times 10^{-12} &< \Delta a_e < 0.62 \times 10^{-12} \\ 128 \times 10^{-11} &< \Delta a_\mu < 448 \times 10^{-11} \end{aligned}$$

Table 6.1. Measured dipole moments for the SM charged leptons and SM expectations.

	Measured Value	SM Expectation
a_e	$1159652180.76(0.27) \times 10^{-12}$	$1159652181.78(0.06)(0.04)(0.03)(0.77) \times 10^{-12}$
a_μ	$116592091.(54)(33) \times 10^{-11}$	$116591803(1)(42)(26) \times 10^{-11}$
a_τ	$117721(5) \times 10^{-8}$	$-0.018(0.017)$
d_e/e	$(-2.1 \pm 3.7 \pm 2.5) \times 10^{-29}\,\text{cm}$	~ 0
d_μ/e	$(-0.1 \pm 0.9) \times 10^{-19}\,\text{cm}$	
$\text{Re}(d_\tau/e)$	$(1.15 \pm 1.70) \times 10^{-17}\,\text{cm}$	

$$-0.015 \quad < \quad \Delta a_\tau < 0.053, \tag{6.1}$$

while for the electric dipole moments, we have

$$\begin{aligned} -3.54 \times 10^{-18} < 2m_e \frac{d_e}{e} < 5.71 \times 10^{-18} \\ -1.82 \times 10^{-6} < 2m_\mu \frac{d_\mu}{e} < 2.03 \times 10^{-6} \\ -0.00405 < 2m_\tau \,\text{Re}\left(\frac{d_\tau}{e}\right) < 0.00819. \end{aligned} \tag{6.2}$$

Note that since we assume that the fundamental Lagrangian is CPT-invariant, all dipole moments are real. The precision of the measurement of the magnetic dipole moment of the muon may be increased by up to a factor of 4 with data from E821 at Fermilab [5].

In this leptophilic scenario, the squarks, charginos and neutralinos (except the bino) are all heavy and are chosen to ensure that constraints from the Higgs mass measurement and direct sparticle searches at the LHC are satisfied. This leaves five relevant parameters to explore for a given slepton: α, ϕ, $m_{\tilde{\ell}_{1,2}}$, and m_χ. For each dipole moment corrections depend only on the superpartners of the particular ℓ (and their associated mixing angles and CP-violating phases), with no dependence on any other sleptons.

In Figure 6.1 we present the α and φ dependence of the new physics contributions to (a) the anomalous magnetic and (b) electric dipole moments of the muon for a case with light smuons, with all other sleptons heavy. In this example, $m_\chi = 100$ GeV, $m_{\tilde{\mu}_1} = 120$ GeV and $m_{\tilde{\mu}_2} = 300$ GeV. The planes are shaded according to the contribution to (a) the anomalous magnetic moment of the muon and (b) the electric dipole moment of the muon. The darker red region in Figure 6.1 (a) is where this model fully accounts for the measured muon anomalous magnetic moment to 2σ, while in the lighter red shaded region new physics provides a contribution that is comparable to the measured value in

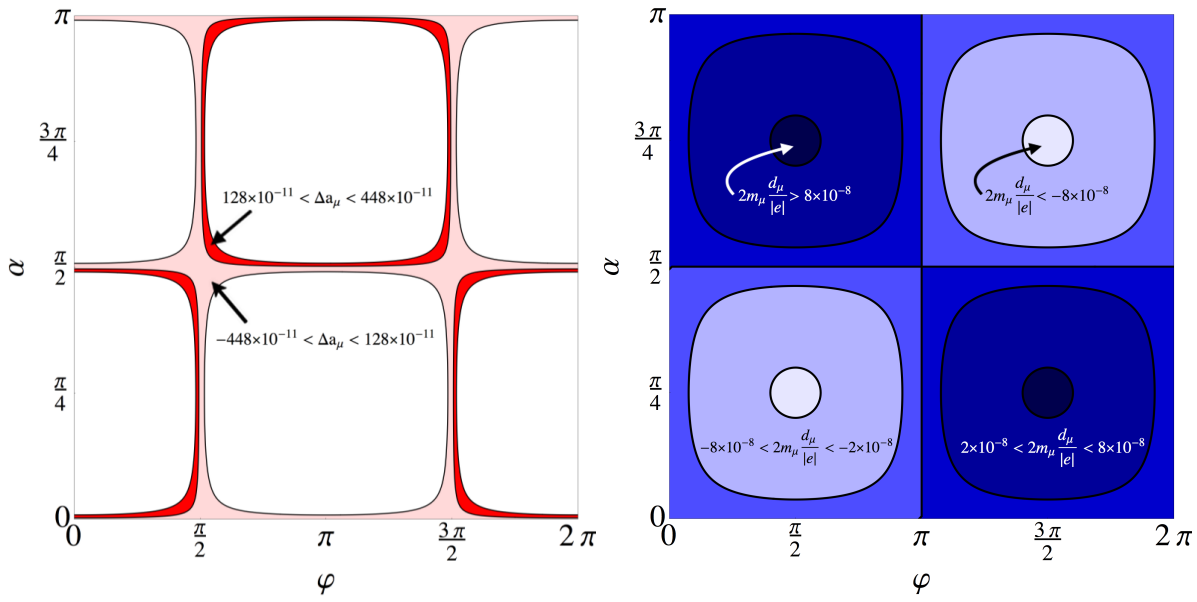

(a) Δa_μ (b) $2m_\mu d_\mu/|e|$

Figure 6.1. The dependence of the contribution to (a) the anomalous magnetic and (b) electric dipole moments of the muon on the smuon L-R mixing angle, α, and the CP-violating phase, φ, for $m_\chi = 100$ GeV, $m_{\tilde{\mu}_1} = 120$ GeV, and $m_{\tilde{\mu}_2} = 300$ GeV. (a) The darker red region is where this model fully accounts for the measured muon anomalous magnetic moment to 2σ, while the lighter red shaded region provides a contribution that is comparable to the measured value in magnitude. (b) The electric dipole moment is unconstrained everywhere in the plane.

magnitude. The contribution to the anomalous magnetic moment vanishes for $\varphi = n\pi/2$ for n odd and for $\alpha = n\pi/2$ for integers n. As shown in Figure 6.1 (b), the electric dipole moment is unconstrained everywhere in the plane, and the shading indicates the value of the contribution to the muon electric dipole moment, which reaches minima at $(\varphi, \alpha) = (\pi/2, \pi/4)$ and $(3\pi/2, 3\pi/4)$ of $2m_\mu d/|e| \approx -10^{-7}$, and maxima at $(3\pi/2, \pi/4)$ and $(\pi/2, 3\pi/4)$ of $2m_\mu d/|e| \approx 10^{-7}$. These values are roughly an order of magnitude below the current sensitivity. The contribution to the electric dipole moment vanishes for $\varphi = n\pi$ and $\alpha = n\pi/2$ for integers n. The only case in which contributions to both dipole moments vanish is that of zero mixing.

6.3 Constraints from the DM relic density

As discussed previously, the Planck satellite has very accurately measured the dark matter abundance to be $\Omega_c h^2 = 0.1196 \pm 0.0031$ [51]. This requires the dark matter an-

nihilation in any particular scenario to be sufficient to ensure that dark matter was not overproduced in the early Universe. This very restrictive constraint will limit the allowed parameter space in these models.

For each annihilation channel $\chi\chi \rightarrow \ell^+\ell^-$, the annihilation cross section depends only on the superpartners of the particular ℓ (and their associated mixing angle and *CP*-violating phase), with no dependence on any other sleptons. As such, we can separately analyze each channel and simply sum the cross sections to determine the relic density if more than one channel is relevant.

In Figure 6.2 we present the α and φ dependence of (a) the neutralino thermal relic density and (b) the neutralino annihilation cross section today for a case with light smuons, with all other sleptons heavy. In this example, $m_\chi = 100$ GeV, $m_{\tilde{\mu}_1} = 120$ GeV and $m_{\tilde{\mu}_2} = 300$ GeV.

As expected, the annihilation cross section is maximized near maximal L-R squark mixing ($\alpha = \pi/4, 3\pi/4$) and is almost zero at $\alpha = 0, \pi$, while being nearly independent of φ. The slight deviations from these above expectations arise from terms which scale as m_ℓ/m_χ; these terms are significant only for annihilation to the τ channel, and even then amount to roughly a $\sim 5\%$ effect. The dependence of the annihilation cross section on the slepton parameters is largely independent of the choice of final state leptons; the distinction between annihilation channels arises instead from the experimental constraints on the slepton masses and the dipole moment corrections.

In Figure 6.2, the thermal relic density is not quite low enough to be within the 2σ Planck range for this particular choice of m_χ and $m_{\tilde{\mu}_{1,2}}$, though this could easily be accomplished with only a small branching fraction to another final state, such as would occur if there were also a relatively light stau, or with the addition of a very small Higgsino content to the LSP. The annihilation cross section today clearly resembles the inverse of the thermal relic density, with expected values $\sim 10^{-26}$ cm^3 s^{-1}. Neither the relic abundance nor the annihilation cross section today depend strongly on the fermion mass; therefore these results are approximately valid for all lepton final states.

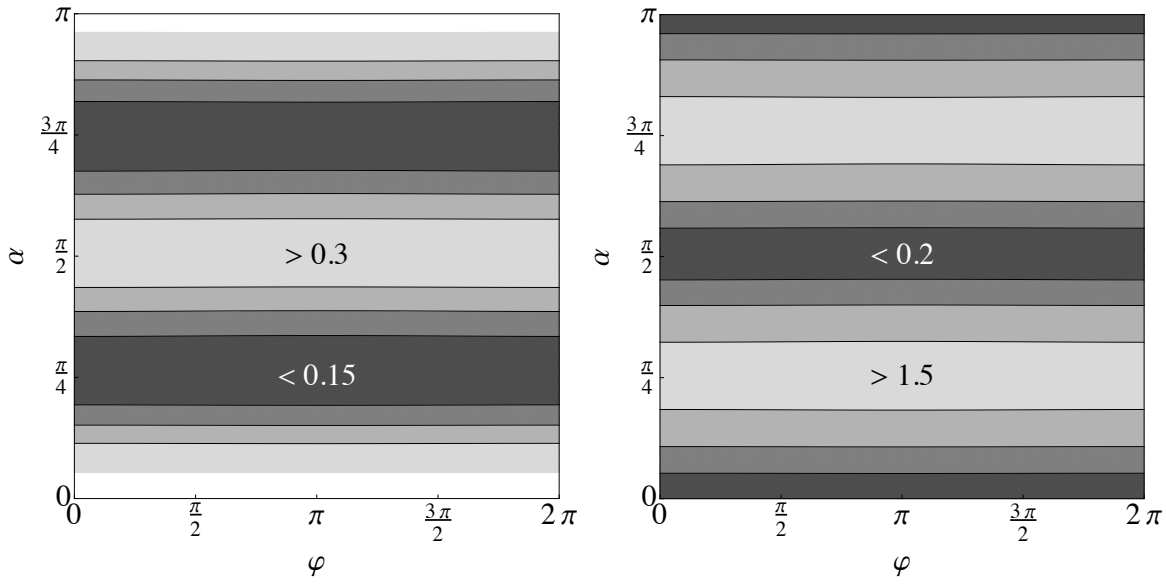

(a) $\Omega_c h^2$ (b) $\langle\sigma v\rangle_{\text{ann.}} / (10^{-26}\ \text{cm}^3\ \text{s}^{-1})$

Figure 6.2. The dependence of (a) the neutralino relic density and (b) the neutralino annihilation cross section today on the smuon L-R mixing angle, α, and the CP-violating phase, φ, for $m_\chi = 100$ GeV, $m_{\tilde{\mu}_1} = 120$ GeV, and $m_{\tilde{\mu}_2} = 300$ GeV.

6.4 Cosmology and collider constraints

To gain insight into how general these features are, we can marginalize over the relevant masses and examine the constraints on the mixing angle and *CP*-violating phase. The three different charged lepton scenarios are shown in Figure 6.3 for the μ channel and Figure 6.4 for the e and τ channels. In each case, the greyed regions are excluded because the relic density would exceed the 2σ upper limit measured by Planck. The blue and red regions are favored by constraints on the electric and magnetic dipole moments, respectively.

We see from Figures 6.3 and 6.4 that applying the constraints in Eqs. (6.1) and (6.2) to Eq. (5.7), annihilation to muons or taus can play a significant role in dark matter annihilation in the current epoch, whereas for the selectron, there are no regions that satisfy all three constraints. For muons, constraints on the anomalous magnetic moment force $\varphi \sim \pm\pi/2$. In this case, the corrections to the muon dipole moment are almost entirely *CP*-violating, and the contribution to the muon electric dipole moment is maximized at $2m_\mu|d_\mu/e| \sim \mathcal{O}(10^{-9})$. As of Feburary 2017, the muon electric dipole moment experiments are much less constraining than those of the magnetic dipole moment, making this scenario

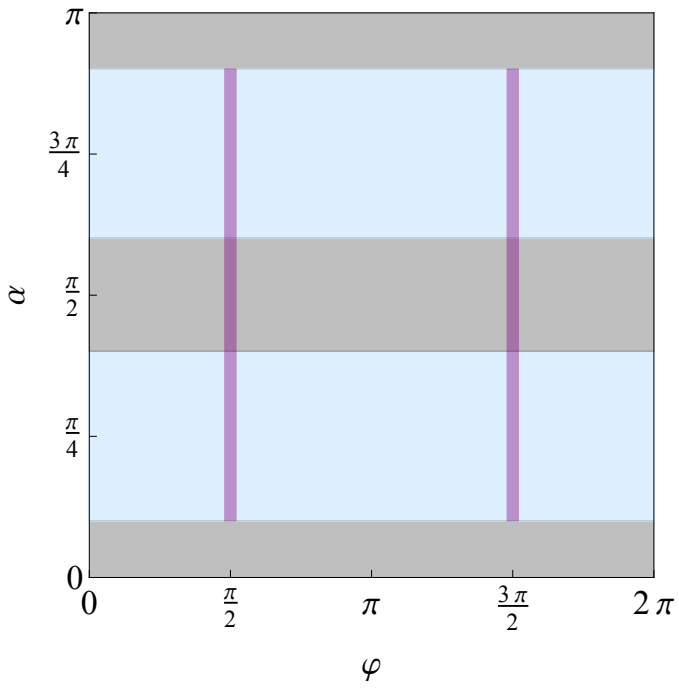

Figure 6.3. The favored regions for the angles for μ case after marginalizing over the smuon masses. The greyed regions are excluded because the relic density would exceed the 2σ measured value. The blue (red) show the regions for the angles where at least one $m_{\tilde{\mu}_1}, m_{\tilde{\mu}_2}$ mass combination produces an electric (magnetic) dipole moment within the current bounds. For the smuon case, the electric dipole moment is not yet constraining these models, while the purple shading shows $\left|\Delta a_\mu\right| \leq 4.5 \times 10^{-9}$ (the $\pm 2\sigma$ region that could explain the measured value of the anomalous magnetic moment of the muon).

perfectly viable. For the τ channel, constraints on both the electric and magnetic dipole moments are too weak to be of any relevance. As such, we see that the relic density constrains α while the dependence of the relevant parameter space on φ is largely trivial.

By contrast, we see that the electron channel can be largely ignored for s-wave annihilation; we see that any choice of α and φ yielding $c_0 \sim 1$ pb would lead to a contribution to either the electric or magnetic dipole moment of the electron far in excess of what could be consistent with experimental measurements, absent some large fine-tuning with other new physics contributions. The selectron L-R mixing angle must vanish to one part in 10^3 in order to satisfy the dipole moment constraints; that is, if $\sin(2\alpha) \approx 0$, then the dipole corrections are small.

Therefore, the constraints for each lepton channels can be summarized as follows:

(i) The $\chi\chi \to e^+e^-$ cross section is constrained to be $\ll 1$ pb, absent fine-tuning

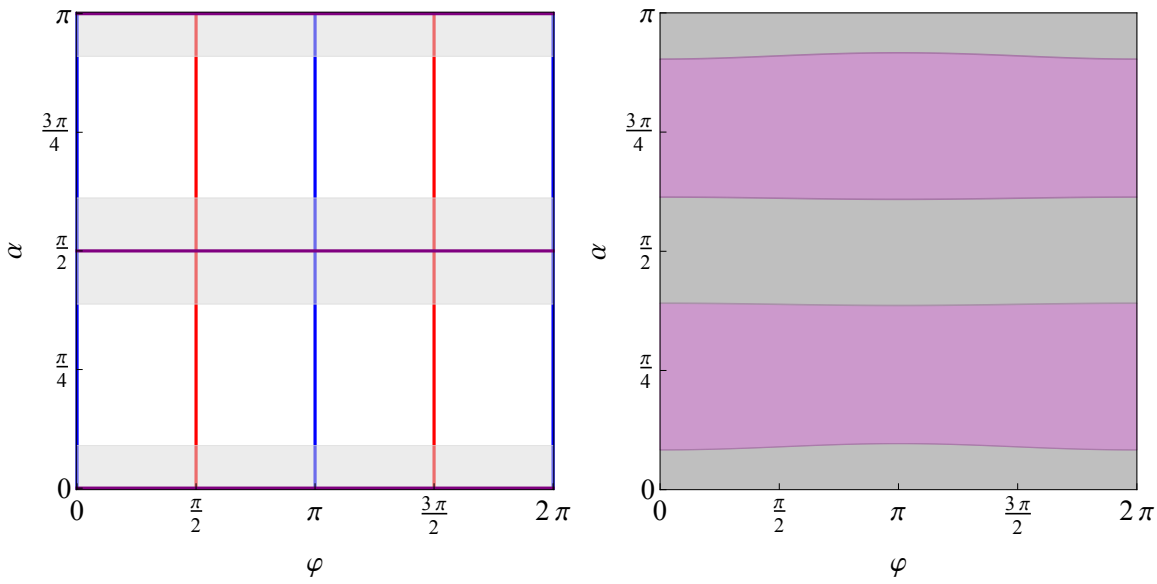

(a) selectron (b) stau

Figure 6.4. The favored regions for the angles in the two different slepton cases, (a) for the selectron and (b) for the stau, after marginalizing over the slepton masses. In each case, the greyed regions are excluded because the relic density would exceed the 2σ measured value. The blue (red) show the regions for the angles where at least one $m_{\tilde{\ell}_1}, m_{\tilde{\ell}_2}$ mass combination produces an electric (magnetic) dipole moment within the current bounds. For the selectron, there are no regions that satisfy all three constraints, whereas for the stau, both dipole moments constraints are too weak to provide any limits so the regions are shaded purple (blue+red).

(ii) The $\chi\chi \to \mu^+\mu^-$ cross section is constrained to be $\ll 1$ pb, absent fine-tuning, unless CP violation is close to maximal ($\varphi \sim \pi/2$). This constraint arises because the muon magnetic dipole moment is much more tightly constrained than its electric dipole moment. For near-maximal CP violation, the annihilation cross section must be less than $\mathcal{O}(100)$ pb, absent fine-tuning.

(iii) The $\chi\chi \to \tau^+\tau^-$ cross section can easily be $\mathcal{O}(1)$ pb, or larger. For our purposes, it is unconstrained by dipole moment bounds.

In Figure 6.5, we also examine how these observables depend on the masses of the smuons. We again choose a dark matter mass of 100 GeV and $\alpha = \pi/4 + 0.02$ (the angle that minimizes the relic density) and $\varphi = \pi/2 - 0.04$. Within the grey regions, one of the smuons would be the LSP. Contours of constant relic density are shown and the red shading indicates the $\pm 2\sigma$ region that would explain the measured value of the anomalous

magnetic moment of the muon. For light smuons, the maximum size of the electric dipole moment would be of order 10^{-9}, which is well below the current limits and is not shown for clarity. We are thus able to find viable regions of parameter space for the light smuons that satisfy all constraints (including the relic density) and can even explain the measured value for the anomalous magnetic moment of the muon.

6.5 Corrections to the SM lepton masses

If the slepton mixing angle α is allowed to be non-zero, then there will be a new contribution to the mass correction for SM leptons arising from the diagram in Figure 6.6, with the bino and sleptons running in the loop.

Note that this contribution includes a term which does not scale as the bare lepton mass, implying that a small lepton mass is no longer technically natural. Essentially, chiral symmetry no longer protects the fermion mass because it is broken by the scalar mass mixing term. However, this correction is not logarithmic in the cutoff scale; the leading contributions from the two diagrams with the two slepton mass eigenstates running in the loop cancel (analogous to the Glashow-Iliopoulos-Maiani mechanism). This contribution to the mass correction is then given by

$$\delta m_\ell \sim \frac{m_\chi}{16\pi^2} Re(\lambda_L \lambda_R^*) \sin(2\alpha) \log\left(\frac{m_{\tilde{\ell}_2}}{m_{\tilde{\ell}_1}}\right), \tag{6.3}$$

and leads to a little hierarchy problem with $\sim$ 1% fine-tuning. We make no attempt to address the flavor or naturalness problems of the SM, however, and thus will not treat this little hierarchy problem as an obstacle. Similarly, we assume a priori that mixing is only allowed between sleptons of the same flavor, thus ensuring that no new FCNCs are induced.

6.6 Indirect detection constraints

The dark matter particles in our models will annihilate primarily to charged leptons (or neutrinos) leading to possibly detectable signals at indirect detection experiments. Strong constraints on dark matter annihilation in the current epoch are placed on these models by gamma-ray searches as well as by the nonobservation of distinct bumps in the otherwise rising positron fraction. In this section, we mainly focus on gamma-ray signatures.

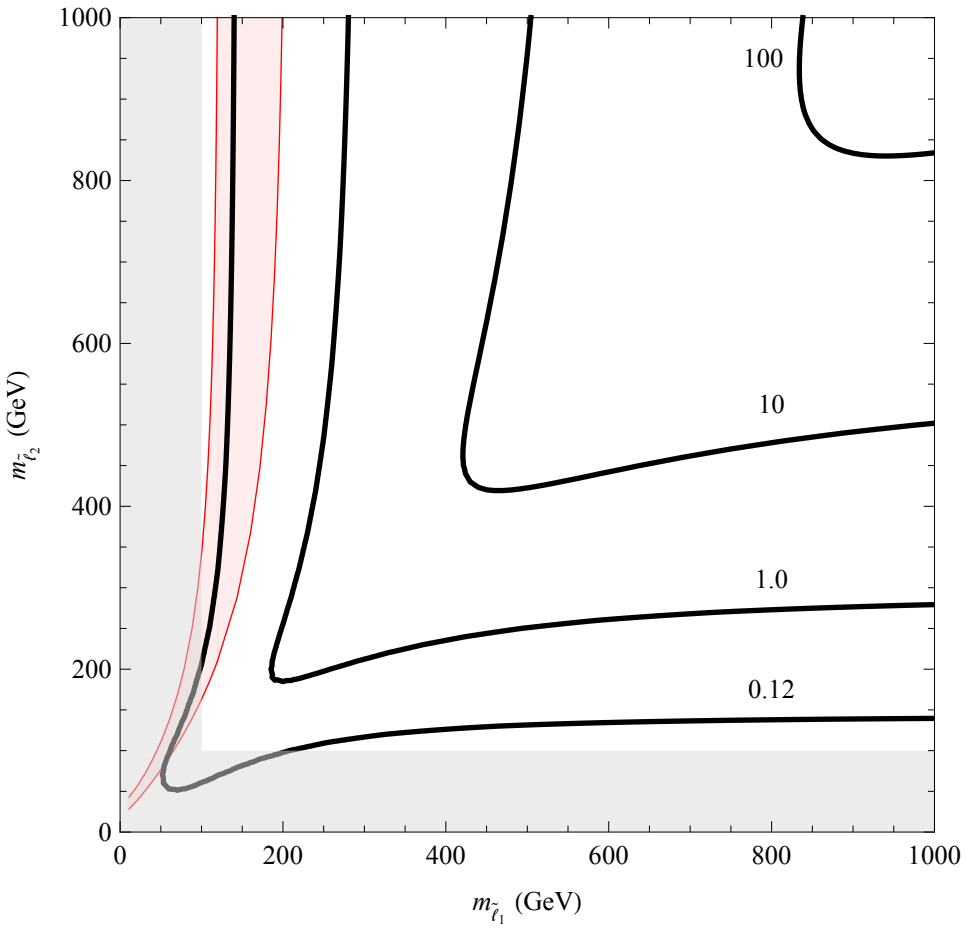

Figure 6.5. The dependence of the relic density and anomalous magnetic moment on the masses of the two smuons for the case of a 100 GeV dark matter particle with $\alpha = \pi/4 + 0.02$ (the angle that minimizes the relic density) and $\varphi = \pi/2 - 0.04$. The grey region is disfavored because the smuon would be the LSP. The labeled contours show the relic density and the red shading indicates the $\pm 2\sigma$ region that would explain the measured value of Δa_μ. For this scenario, the size of the electric dipole moment would be of order 10^{-9}, which is well below the current limits and is left off the plot for clarity.

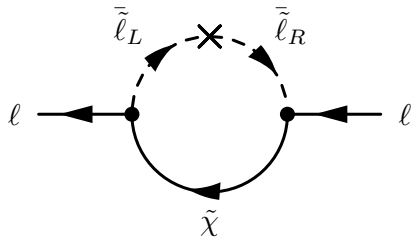

Figure 6.6. Feynman diagram for the mass correction.

6.6.1 Monoenergetic γ-ray searches

In this section we consider the gamma-ray signals arising from the processes $\chi\chi \to \bar{f}f\gamma$, $\gamma\gamma$, and γZ in the most general case, including nontrivial fermion mass and nontrivial left-right mixing and CP-violating phase for the charged mediators. In the following discussion, we will focus on several benchmark models, displayed in Table 6.2. We take $m_\chi = 100\,\text{GeV}$, $m_{\tilde{f}_1} = 120\,\text{GeV}$, and $m_{\tilde{f}_2} = 450\,\text{GeV}$ for models A, B, and C, which are consistent with a supersymmetric implementation of the Lagrangian in Eq. (2.4), while $m_\chi = 100\,\text{GeV}$, $m_{\tilde{f}_1} = 102.5\,\text{GeV}$, and $m_{\tilde{f}_2} = 450\,\text{GeV}$ for models D and E, which are explicitly nonsupersymmetric due to the couplings $\lambda_{L,R}$ and, in the case of model E, an additional heavy fermion. Note that for all of these benchmark points, the new charged particles are fully consistent with constraints from the LHC and LEP. Benchmark E presents an interesting case, as it contains a new charged fermion with $m_f = 105\,\text{GeV}$. Such a particle is within the energy reach of the LHC, and one must worry if such a particle would already be excluded by current data. But LHC sensitivity to new charged particles depends greatly on the particle decay chains; it is easy to choose a decay scenario for which f would escape current LHC limits. For example, if the new 105 GeV fermion decayed to a SM charged lepton and a new $\sim 100\,\text{GeV}$ invisible scalar, then this charged fermion would escape detection for the same reason that light sfermions do in the compressed spectrum scenario. The new invisible scalar need not contribute to dark matter, or even be long lived, provided its lifetime is long enough to decay outside the detector. We will not focus further on this particular decay scenario, which we describe only to demonstrate that benchmark E can be completely consistent with LHC constraints. For models where m_f is even larger, LHC constraints may be more easily satisfied, without qualitatively changing the analytic results we obtain.

Table 6.2. Benchmark models considered in the following discussion.

	Channel	λ_L	λ_R	α	φ	Marker
A	$\mu^+\mu^-$	$\sqrt{2}Y_L g'$	$\sqrt{2}Y_R g'$	$\pi/4$	$\pi/2$	Star
B	$\tau^+\tau^-$				0	Circle
C					$\pi/2$	Cross
D	$\mu^+\mu^-$	0.8	0.8	$\pi/6$	$\pi/2$	Square
D'		0.75	0.75			Diamond
E	$\bar{f}f$, $m_f = 105\,\text{GeV}$	2	2	$\pi/4$	$3\pi/4$	Triangle

In the following subsections, we examine the line signal strengths in the context of different SUSY and non-SUSY models. The search for line signals of dark matter annihilation has been one of the primary goals of various ground-based and satellite-based experiments. In general, the ground-based atmospheric CTA [206, 207] are most effective for dark matter that is somewhat heavier than 100 GeV. For example, with 500 h of observing time, CTA will be sensitive to cross sections $\sim 10^{-27}\text{cm}^3\,\text{s}^{-1}$ for dark matter with mass of ~ 300 GeV annihilating to $\tau^+\tau^-$ in the Galactic center region [245]. Due to its much lower energy threshold, the Fermi Gamma-Ray Space Telescope is better suited to study dark matter masses in the range 0.1 to a few hundred GeV, which is the range we are interested in here. For $m_\chi \lesssim 100$ GeV, the Fermi LAT has set a limit on the thermally averaged annihilation cross section to $\gamma\gamma$ of $\langle\sigma v\rangle_{\gamma\gamma} \approx 10^{-28} \sim 10^{-29}\text{cm}^3\,\text{s}^{-1}$ with the 95% CL containment spanning approximately one order of magnitude using the PASS 8 analysis of 5.8 years of data [26]. However, this limit, as well as any projected sensitivities, is sensitive to the dark matter profile of the Milky Way halo and may move up or down by about one order of magnitude for different profiles. We hope that the sensitivity to $\langle\sigma v\rangle_{\gamma\gamma}$ will be improved with additional data and/or new technology. Future satellite-based experiments GAMMA-400 [208] and HERD [246] are expected to reach $\langle\sigma v\rangle_{\gamma\gamma} \lesssim 10^{-28}\text{cm}^3\,\text{s}^{-1}$ for $m_\chi = 100\,\text{GeV}$. In addition, each of these experiments is expected to have energy resolution of $\sim 1\%$, which is much better than Fermi-LAT's ($\sim 10\%$ at 100 GeV), making it possible to distinguish between a sharply peaked IB spectrum and a true line signal.

We first consider the SUSY case, as in Ref. [202], where f and $\widetilde{f}$ are SM leptons and MSSM sleptons, therefore denoted as ℓ and $\widetilde{\ell}$ in this subsection. In Figure 6.7, we display the cross sections (a) $\langle\sigma v\rangle_{\gamma\gamma}$ and (b) $\langle\sigma v\rangle_{\gamma Z}$ as functions of α for $\varphi = 0$, $\pi/2$, and π. Since $\langle\sigma v\rangle_{\gamma Z}$ is only mildly sensitive to the CP-violating phase, φ, we show the cross section as a function of φ for $\alpha = \pi/4$ in the inset of the right panel. Turning first to the left panel, we see an increase of $\langle\sigma v\rangle_{\gamma\gamma}$ by a factor of 6 as α ranges from zero to $\pi/4$ at $\varphi = \pi/2$ (and as much as a factor of $\gtrsim 10$ over the full range of α shown). For the τ channel, displayed in Figure 6.7, the dependence on φ is significant (in contrast to the μ channel): At $\alpha \approx \pi/4$, $\langle\sigma v\rangle_{\gamma\gamma}$ varies by a factor of 2 as φ ranges from zero to $\pi/2$. Turning to the right panel, we see that there is an increase in $\langle\sigma v\rangle_{\gamma Z}$ by about a factor of 16 for $\alpha = \pi/2$ relative to $\alpha = 0$. This arises from the fact that $Y_R = 2Y_L$: for $\alpha = \pi/2$ ($\alpha = 0$), the lighter

scalar mass eigenstate consists entirely of the right-handed (left-handed) component, the contribution to the cross section of which is proportional to Y_R^4 (Y_L^4). This enhancement is possible only when the two-body annihilation cross section is suppressed ($\alpha = n\pi/2$ for n odd), and thus the relic abundance of binos is too large. If another mechanism, such as coannihilation, helped to lower the relic abundance, or if dark matter were nonthermal, it may be possible for the line signal to be much larger than that suggested by the benchmark points. As we see in the right panel of Figure 6.7, the dependence of $\langle \sigma v \rangle_{\gamma Z}$ on the CP-violating phase is not as significant as it is for annihilation to $\gamma\gamma$, even for the τ channel.

In Figure 6.8, we display a contour plot of $\langle \sigma v \rangle_{\gamma\gamma}$ with respect to the chiral mixing, α, and CP-violating phase, φ. The regions of parameter space in which the dark matter is a thermal relic are shaded blue, and, for the μ channel, the regions compatible with the measurement of the muon anomalous magnetic moment are shaded red/magenta (for the τ channel, the dipole moment measurements do not constrain the parameter space). Benchmarks A, B, and C are also marked.

Unfortunately for the SUSY case, these monochromatic photon signals lie well below the current experimental sensitivity. Nonetheless, it is worth considering the possibility of an eventual detection. As discussed in Sec. 4.2, once a statistical excess of these line signals is observed, and if the dark matter mass lies in the range $m_Z < m_\chi \lesssim 140\,\text{GeV}$ (for Fermi-LAT) or $\lesssim 450\,\text{GeV}$ (for GAMMA-400 or HERD), the ratio of the dark matter annihilation cross section into $\gamma\gamma$ and γZ will be of significant interest for determining the nature of the dark matter particle and the theory of physics beyond the SM in which it resides. Indeed, this ratio does not suffer from astrophysical uncertainties in the dark matter distribution in our Galaxy [209]. In Ref. [247], a wide range of MSSM parameter space is examined, and an attempt is made to use the ratio of $2\,\langle \sigma v \rangle_{\gamma\gamma} \,/\, \langle \sigma v \rangle_{\gamma Z}$ to distinguish among coannihilation, funnel, and focus point scenarios in mSUGRA, as well as within more general MSSM scenarios.

Following the same line of analysis, we plot the annihilation cross section to $\gamma\gamma$ (left) and the ratio $2\,\langle \sigma v \rangle_{\gamma\gamma} \,/\, \langle \sigma v \rangle_{\gamma Z}$ (right) as functions of the slepton masses in Figure 6.9 for the μ (top) and τ (middle and bottom) channels for $m_\chi = 100\,\text{GeV}$ and $\alpha = \pi/4$. In the top panels, we display the μ channel with $\varphi = \pi/2$ and in the middle and lower panels, we display the tau channel with $\varphi = 0$ and $\pi/2$, respectively. In the left panels, we display the

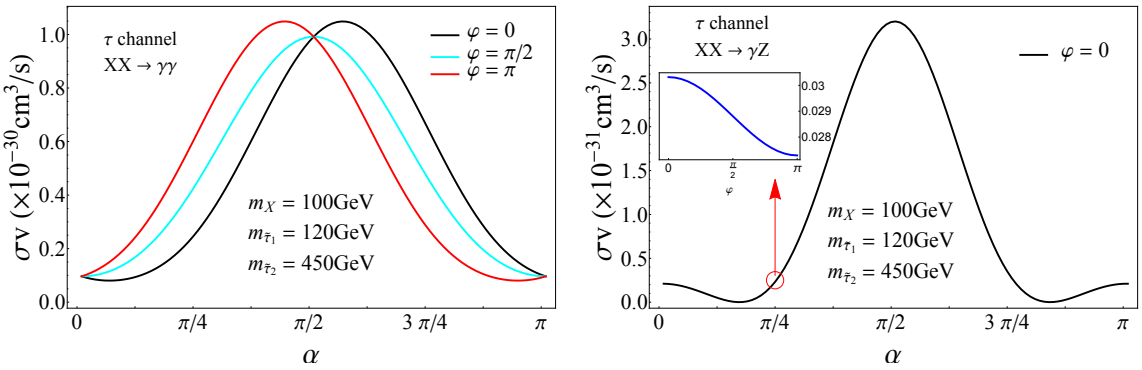

(a) $\gamma\gamma$ (b) γZ

Figure 6.7. The dependence of (a) $\langle\sigma v\rangle_{\gamma\gamma}$ and (b) $\langle\sigma v\rangle_{\gamma Z}$ on α and φ for SUSY bino dark matter with coupling only to τ and $\widetilde{\tau}$.

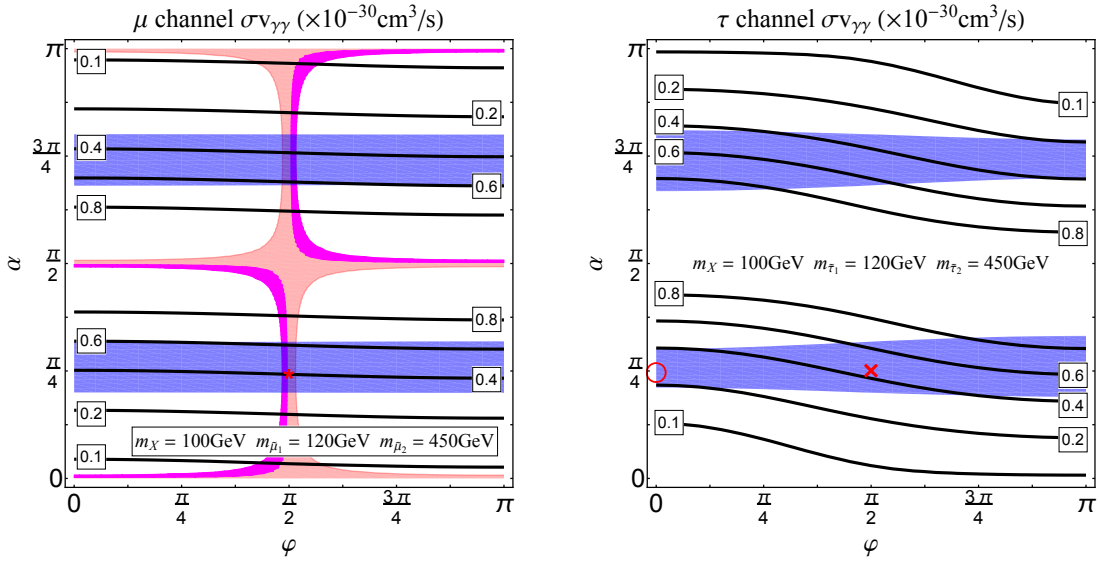

(a) μ channel (b) τ channel

Figure 6.8. The dependence of $\langle\sigma v\rangle_{\gamma\gamma}$ on the slepton mixing angle, α, and the CP-violating phase, φ, for (a) the μ channel and (b) τ channel, for the SUSY case $\lambda_L = 2\lambda_R$. In each plot, the blue stripe indicates the region that satisfies $0.11 < \Omega h^2 < 0.13$. In the μ channel plot (left), the light magenta region of our parameter space leads to $128 \times 10^{-11} < a_\mu < 448 \times 10^{-11}$, which resolves the issue of the muon anomalous dipole moment. In the light red region, we have instead $-448 \times 10^{-11} < a_\mu < 128 \times 10^{-11}$, which neither solves nor exacerbates the discrepancy between the observed muon anomalous magnetic moment and the SM expectation. For the τ channel, the dipole moment measurements do not constrain the parameter space. The red markers (star, circle, and cross) indicate the positions of our benchmark models (A, B, and C, respectively).

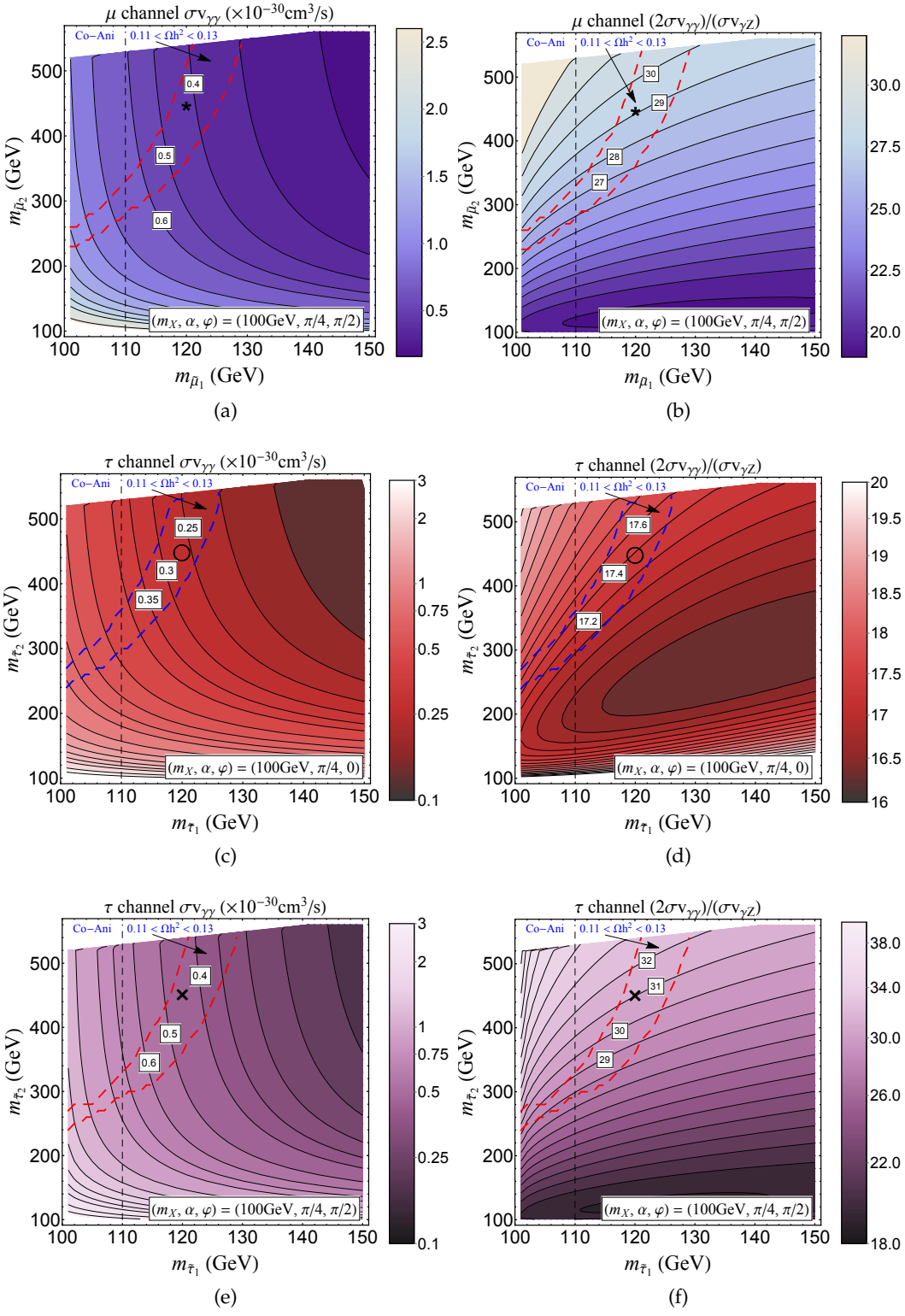

Figure 6.9. The dependence of the $\chi\chi \to \gamma\gamma$ cross section (left) and the ratio $2\langle\sigma v\rangle_{\gamma\gamma} / \langle\sigma v\rangle_{\gamma Z}$ (right) on the slepton masses for the SUSY case, $\lambda_L = 2\lambda_R$. The black markers in each plane indicate the positions of our benchmark points. Note that in three of the plots we have used a log-scaled color function.

$\chi\chi \to \gamma\gamma$ cross sections in units of 10^{-30} cm^3 s^{-1}, while in the right panels we show the ratio $2\langle\sigma v\rangle_{\gamma\gamma} / \langle\sigma v\rangle_{\gamma Z}$. The parameter space that accommodates thermal relic dark matter lies between the thick dashed contours that cut diagonally across each plane. As expected, $\langle\sigma v\rangle_{\gamma\gamma}$ decreases as the slepton masses increase. Similarly, the ratio $2\langle\sigma v\rangle_{\gamma\gamma} / \langle\sigma v\rangle_{\gamma Z}$ increases as the difference between $m_{\tilde{\ell}_1}$ and $m_{\tilde{\ell}_2}$ increases. $2\langle\sigma v\rangle_{\gamma\gamma} / \langle\sigma v\rangle_{\gamma Z}$ is larger than 17.0 for $\varphi = 0$ in the τ channel. Although not presented in Figure 6.9, this approximately holds true for the μ channel as well. In the case of $\varphi = \pi/2$, $2\langle\sigma v\rangle_{\gamma\gamma} / \langle\sigma v\rangle_{\gamma Z}$ is greater than 26 for the μ channel and greater than 28 for the τ channel. By contrast, in the coannihilation region in mSUGRA, $2\langle\sigma v\rangle_{\gamma\gamma} / \langle\sigma v\rangle_{\gamma Z}$ ranges from 7-12 (see Figure 5 in Ref. [247]). It is therefore possible that if both the $\gamma\gamma$ and γZ lines are observable, the ratio of the signal strengths could be used to distinguish between, for example, the coannihilation region and a model similar to the Incredible Bulk. Though these scenarios could, in principle, also be distinguished by the cosmic-ray signal arising from $\chi\chi \to \ell^+\ell^-$, such a signal would be subject to astrophysical uncertainties and would therefore leave much room for doubt.

In summary, the $\chi\chi \to \gamma\gamma$ cross sections increase by a factor of ~ 2 as φ varies from 0 to $\pi/2$, as does the the ratio $2\langle\sigma v\rangle_{\gamma\gamma} / \langle\sigma v\rangle_{\gamma Z}$ (since the $\chi\chi \to \gamma Z$ cross section is insensitive to the value of φ). As the slepton masses increase, $\langle\sigma v\rangle_{\gamma\gamma}$ becomes smaller, while $2\langle\sigma v\rangle_{\gamma\gamma} / \langle\sigma v\rangle_{\gamma Z}$ increases as the difference between $m_{\tilde{\ell}_1}$ and $m_{\tilde{\ell}_2}$ increases.

There are two other scenarios we consider, beyond the Incredible Bulk scenario of binolike dark matter in the MSSM, in which the monoenergetic gamma-ray line signals are particularly interesting: $f = \mu$ (benchmark D), and $m_f > m_\chi$ (benchmark E), each with arbitrary but perturbative couplings. If $m_f > m_\chi$, as in benchmark E, the processes $\chi\chi \to \bar{f}f(\gamma)$ are kinematically forbidden, and the processes $\chi\chi \to \gamma\gamma, \gamma Z$ will be the most important for indirect detection.

If $f = \mu$, as in benchmark D, then the process $\chi\chi \to \mu^+\mu^-$ produces few photons or antiprotons through final state decay. As a result, the $2 \to 2$ cross section is constrained only by positron searches and dipole moment constraints. Tight constraints on the $\chi\chi \to \mu^+\mu^-$ cross section have been presented in the literature based on AMS-02 positron searches [16], which would require $\langle\sigma v\rangle_{\mu^+\mu^-} \lesssim 1$ pb. But these analyses have relatively large systematic uncertainties arising from assumptions about the sources of astrophysical backgrounds and propagation effects [248]. A full discussion of these issues is beyond the scope of this

work, but it suffices to note that gamma-ray signal arising from the process $\chi\chi \to \gamma\gamma, \gamma Z$ is much cleaner than the positron signal arising from the process $\chi\chi \to \mu^+\mu^-$, particularly since the gamma-ray signal can point back to sources which are well understood, such as dwarf spheroidals. As a result, these gamma-ray signals are of interest even for large α and $\lambda_{L,R}$, where the $\chi\chi \to \mu^+\mu^-$ cross section would be in tension with analyses of AMS-02 electron flux data. Note, however, that this rationale would be less compelling in the case where $f = \tau$, as in this case, the process $\chi\chi \to \tau^+\tau^-$ can produce gamma-ray signals from dwarf spheroidals, arising from hadronic $\tau^\pm$ decay.

In Figure 6.10, we show the cross section for the process $\chi\chi \to \gamma\gamma$ as a function of α and φ for benchmark E. We see that Fermi line searches [26] tend to constrain models with large left-right mixing and small CP violation. Note that this is in contrast to the case of $m_f < m_\chi$, where larger CP violation tends to lead to a larger $\langle\sigma v\rangle_{\gamma\gamma}$ cross section. Future experiments with a larger effective area and/or energy resolution could improve on these sensitivities.

In Figure 6.11 we plot, for the μ channel, the asymmetry ratio

$$R = \frac{\sigma(++) - \sigma(--)}{\sigma(++) + \sigma(--)}, \tag{6.4}$$

where $\sigma(\pm\pm)$ is the annihilation cross section with two positive or negative helicity final

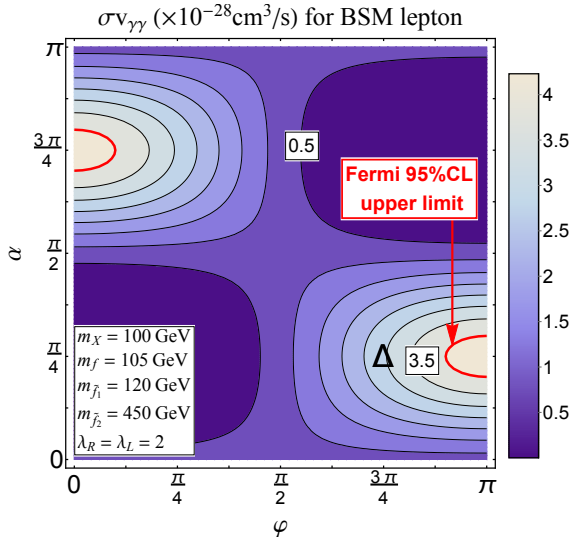

Figure 6.10. The cross section for the process $\chi\chi \to \gamma\gamma$ with $m_f > m_\chi$. Benchmark E is labeled by the triangle. Here and in the following figures, the Fermi line constraint is taken as 4×10^{-28}cm^3/s for $m_\chi = 100$ GeV [26].

state photons. Note that this ratio is independent of the common scaling of λ_L and λ_R. As expected, this asymmetry is maximized at large left-right mixing and the maximal CP-violating phase. At its maximum, the asymmetry is $\sim 2\%$, which is larger than one might naively expect from the m_f/m_χ suppression of the CP-violating term in the matrix element. This arises because the loop integral relevant for the CP-violating term happens to be about an order of magnitude larger than the integral which is relevant for the CP-conserving term in the $m_f \ll m_\chi$ limit. If we have $m_{\tilde{f}_i} > m_f > m_\chi$, as in benchmark E, then R is identically zero, as expected from the optical theorem. The detailed reason is that beyond the branching point $m_f = m_X$, all the loop integrals are real, and the amplitudes of the $(++)$ and $(--)$ final states are conjugate with each other and lead to the same cross section. See the Appendix for details.

In Figure 6.12 we plot the asymmetry ratio R for Benchmark D, except that we instead take $f = \tau$. In this case, as expected, the asymmetry is about an order of magnitude larger, because the m_f/m_χ suppression factor is about a factor of 10 larger. Note that the cross section asymmetry is linear in this suppression factor, since it arises from the interference of the CP-conserving and CP-violating pieces. Although the asymmetry is more pronounced in this case than in the case where the fermion is a muon, the couplings $\lambda_{L,R}$ are also more tightly constrained in this case due to tight bounds on the process $\chi\chi \to \tau^+\tau^-$ arising from Fermi searches for the continuum photons from τ-decay via a neutral pion [8, 249].

In particular, we find the most general spectrum for internal bremsstrahlung, which interpolates between the regimes dominated by virtual internal bremsstrahlung and by final state radiation. We also examine the variation in the ratio $2\,\langle\sigma v\rangle_{\gamma\gamma} \,/\, \langle\sigma v\rangle_{\gamma Z}$ and the helicity asymmetry in the $\chi\chi \to \gamma\gamma$ process, each as a function of the mixing angle and CP-violating phase.

Here, we present our results for the bremsstrahlung and other prompt photon emissions arising from dark matter annihilation to fermions and monochromatic emissions from annihilation to $\gamma\gamma$ and γZ. By prompt emission, we mean the photons produced directly at the dark matter annihilation, including, for example, the hadronic decay of the final state $\tau^\pm$. On the other hand, the photon emission due to inverse Compton scattering and bremsstrahlung in the Galactic electromagnetic fields (so-called secondary emission), which depends on modeling of the dark matter distribution and cosmic-ray propagation, is

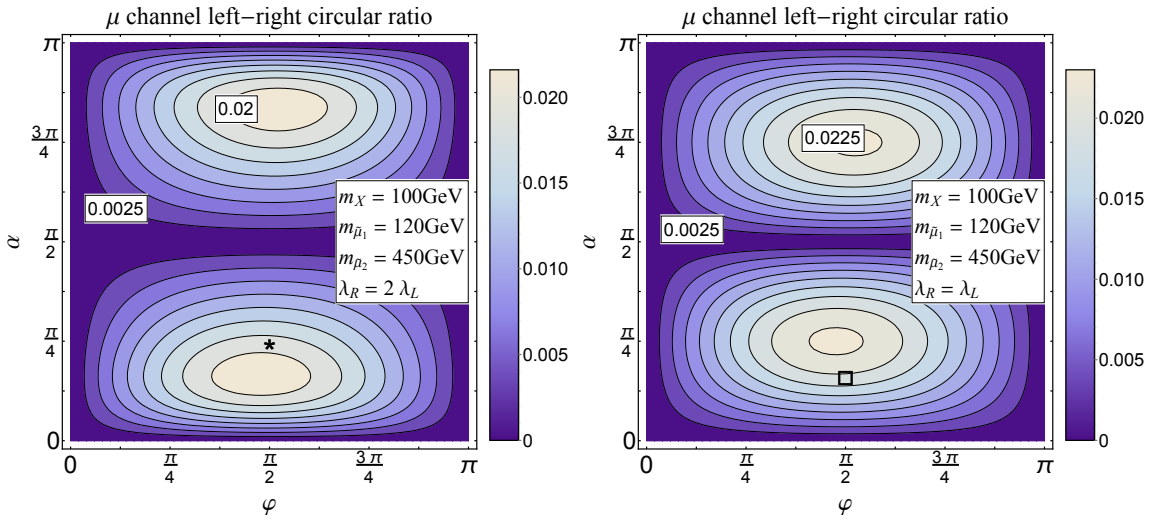

(a) $\lambda_R = 2\lambda_L$ (b) $\lambda_R = \lambda_L$

Figure 6.11. The asymmetry ratio R for the μ channel $\chi\chi \to \gamma\gamma$ process. The left panel shows $\lambda_R = 2\lambda_L$, while the right panel shows $\lambda_L = \lambda_R$. Benchmarks A and D are labeled by the star and square, respectively.

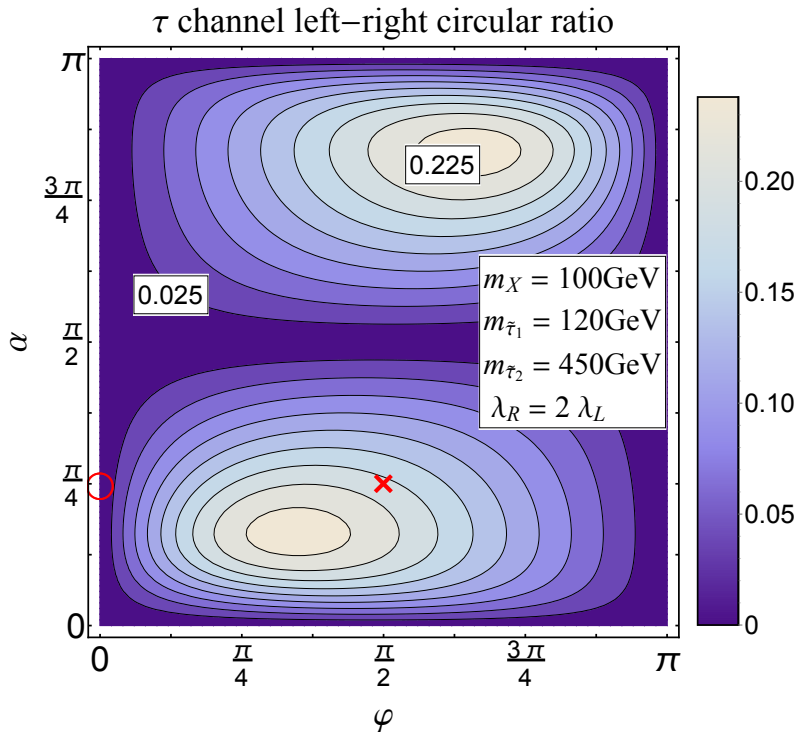

Figure 6.12. The asymmetry ratio R as in Figure 6.11, but for the τ channel, with $\lambda_R = 2\lambda_L$. Benchmarks B and C are labeled by the circle and cross, respectively.

not included, since explaining certain gamma-ray signals at particular regions of galaxies is not our intention.

We would like to make a few general comments regarding the sensitivity of the dark matter annihilation cross sections into $\gamma\gamma$ and γZ to scalar chiral mixing and CP violation. First, both cross sections decrease as the scalar masses increase. Thus, to make a sizable line signal, we need to have at least one scalar mass not too much heavier than the dark matter. If they are very degenerate, of course, coannihilations, not considered here, would also play a role in determining the relic density. Second, the ratio $2\,\langle\sigma v\rangle_{\gamma\gamma} \,/\, \langle\sigma v\rangle_{\gamma Z}$ increases as the difference between the two scalar masses increases. As a very crude estimate, this ratio is approximately $2\tan^{-2}\theta_W \sim 7$, which works well at no mixing. However, by varying the mixing angle and CP-violating phase, we can make it as large as 40 within the MSSM.

The Fermi collaboration has recently released the strongest constraints on dark matter annihilations to leptons in the GeV to TeV mass range by looking at 25 Milky Way satellite galaxies [250]. There are currently no planned gamma-ray experiments that would lead to significant improvements on these indirect detection limits in the channels relevant to our models. The Gamma-400 satellite will have significantly better angular and energy resolution than the Fermi LAT, allowing it to perform very sensitive searches for strong spectral features such as gamma-ray lines [251]. The effective area will be smaller, however, leading to only minor improvements in the limits in the channels relevant to our models [252].

The prospects for indirect detection of these models are quite good. The sensitivity of the Fermi telescope to gamma rays from dwarf galaxies [250] is relevant really only for the case of annihilations to taus: a 100 GeV dark matter particle annihilating with the thermal cross section to $\tau^+\tau^-$ would be roughly a factor of 5 above the current Fermi limit. The improved statistics due to the longer exposure and possible new dwarf galaxies discovered in the southern hemisphere by upcoming large surveys makes this scenario potentially detectable. The electron and muon cases are much less optimistic, however, with the current limits more than an order of magnitude above the thermal cross section. Even the most optimistic assumptions would put these scenarios just on the edge of detectability.

6.6.2 Continuum γ-ray searches

In Figure 6.13, we plot the continuum photon spectrum for both μ and τ final states with three different lightest scalar masses. As expected, the $\alpha = 0$ case produces a hard spectrum which falls rapidly at low energies. The peak feature is more prominent for degenerate χ and $\widetilde{f}_1$. Moreover, the normalization of the spectrum remains stable as $m_f/m_\chi \to 0$. Once α is large enough, the spectrum flattens due to the enhancement in emission of soft photons. If the lightest scalar mediator ($\widetilde{f}_1$, without loss of generality) is much lighter than the heavier scalar, one expects the crossover between these behaviors to occur roughly when

$$\tan^2\alpha \times |\lambda_R/\lambda_L|^2 (m_{\widetilde{f}_1}/m_\chi)^4 \log(m_\chi^2/m_f^2) \sim \mathcal{O}(1)\,, \tag{6.5}$$

which corresponds to the point where the suppression of soft FSR due to the small mixing angle is roughly canceled by the enhancement for collinear emission. Note that one expects the hard IB signal to dominate over $2 \to 2$ scattering provided

$$\tan^2\alpha \times |\lambda_R/\lambda_L|^2 (m_{\widetilde{f}_1}/m_\chi)^4 < \alpha_{\rm EM}\,. \tag{6.6}$$

We thus see, for example, that if $m_\chi \sim 100$ GeV and $f = \mu$, then for a choice of parameters such that the photon spectrum will interpolate between the hard and FSR regimes, the cross section for $\chi\chi \to \bar{f}f\gamma$ with a hard photon will be $\mathcal{O}(10\%)$ of the $\chi\chi \to \bar{f}f$ cross section. For $f = \tau$, the high energy spectrum behaves in a similar way, but there is an α-independent bump at the low energy end due to the photons from the hadronic decay of $\tau^\pm$.

To get a better idea of when the peak feature disappears, we plot in Figure 6.14 the ratio of the photon number in the peak to the total photon number (integrated from $x = 0.01$ to the cutoff). To find out the peak for each α, we integrate the photon number in a bin of which the width is 10% of its central value and slide it from $x = 0.6$ to the cutoff. The peak corresponds to the maximum photon number found in this process. For $f = \mu$, we may see that the transition happens around $\alpha \sim \pi/100$.

At this point, we would like to clarify the procedure used to obtain the components of the spectra. As mentioned above, prompt photon emission can also come from the decay of the charged SM particles produced by dark matter annihilation. The prompt photon

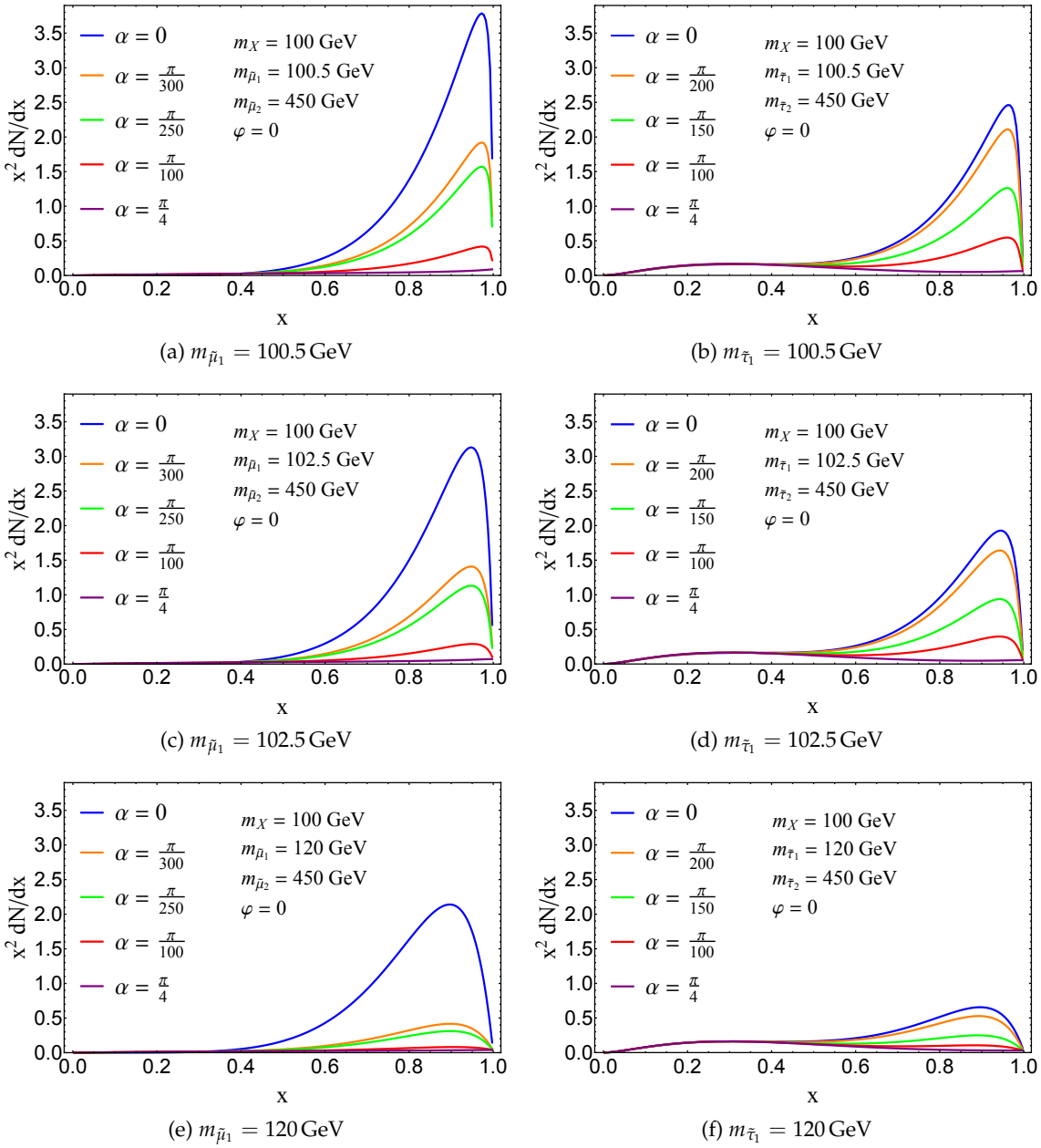

(a) $m_{\tilde{\mu}_1} = 100.5\,\text{GeV}$ (b) $m_{\tilde{\tau}_1} = 100.5\,\text{GeV}$

(c) $m_{\tilde{\mu}_1} = 102.5\,\text{GeV}$ (d) $m_{\tilde{\tau}_1} = 102.5\,\text{GeV}$

(e) $m_{\tilde{\mu}_1} = 120\,\text{GeV}$ (f) $m_{\tilde{\tau}_1} = 120\,\text{GeV}$

Figure 6.13. Dependence of the continuum photon spectrum on α for the process $\chi\chi \to \bar{f}f\gamma$. The left panels show the μ channel and the right show the τ channel. The three $\tilde{\ell}_1$ masses correspond to $\mu_1 = 1.01$, 1.05, and 1.44. We take $\lambda_L = (1/\sqrt{2})g'$, $\lambda_R = \sqrt{2}g'$.

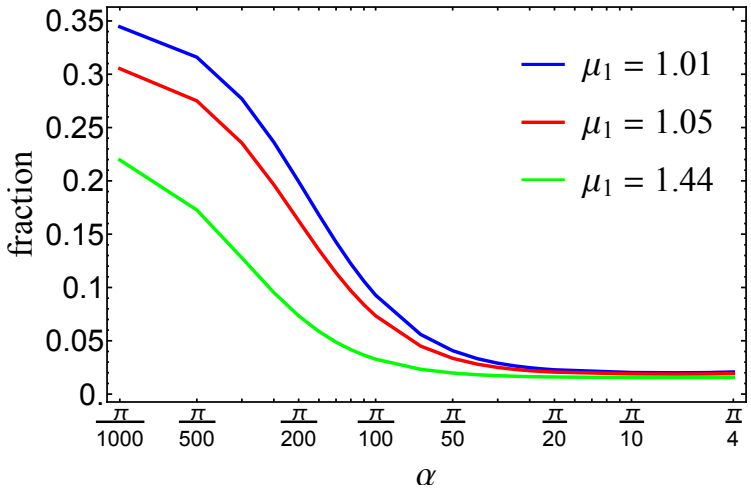

Figure 6.14. The photon number fraction in the peak of $\mu^+\mu^-\gamma$ final state for three different lightest scalar masses. The model parameters are the same as in the left panel of Figure 6.13.

spectrum is usually simulated by event generators such as PYTHIA, which first create the final state phase space for the decay of a hypothetical boson with various branching ratios into SM particles, then simulate the prompt evolution of the final state, and finally return the resultant photon spectrum. In particular, the FSR of the decay, as the leading order contribution, is thus captured by the simulation. But in our calculation of bremsstrahlung, FSR is necessarily included in order for the calculation to be gauge invariant. Thus, as in Ref. [212], we must subtract the FSR from the PYTHIA decay spectrum before adding the bremsstrahlung spectrum.

Moreover, the gamma-ray signals from dark matter annihilation in this scenario are often crucial to observational strategies, because gamma-ray signals are relatively clean, and because the direct annihilation process $\chi\chi \to \bar{f}f$ is often suppressed.

6.6.3 Constraints from the Fermi-LAT γ-ray search data

In Figure 6.15, we plot the Fermi-LAT exclusion contours for $f = \mu$ in the (α, φ) plane for Benchmark D with $\lambda_L = \lambda_R = 0.8$ and $\mu_1 = 1.44$ and Benchmark D' with $\lambda_L = \lambda_R = 0.75$ and $\mu_1 = 1.05$. Since the Fermi-LAT analysis searches for photons, and muon decay produces few photons, this is essentially a search for the $\chi\chi \to \bar{f}f\gamma$ (for these parameters, the monoenergetic photon final states are subdominant). For the

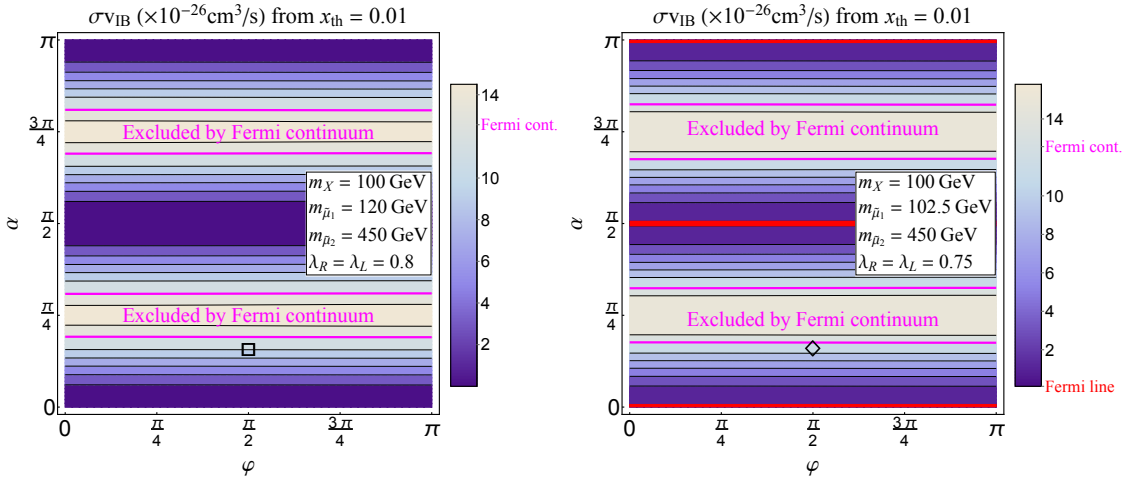

(a) $\mu_1 = 1.44$ (b) $\mu_1 = 1.05$

Figure 6.15. The total IB cross section for (a) $\mu_1 = 1.44$ and $\lambda_L = \lambda_R = 0.8$ and (b) $\mu_1 = 1.05$ and $\lambda_L = \lambda_R = 0.75$. At large mixing, both models are constrained by the Fermi continuum limit; At $\alpha \sim 0$, $\pi/2$ and π, the spectrum of (b) is linelike so it is also constrained by the Fermi line limit. The benchmarks D and D' are labeled by the square and diamond. The Fermi continuum limit is taken from Ref. [27].

parameter range displayed, the maximum cross section for $\chi\chi \to \mu^+\mu^-\gamma$ in the (α, φ)-plane is $\sim 1.4 \times 10^{-25}\text{cm}^3/\text{s}$. For $\mu_1 = 1.44$, the cross section for process $\chi\chi \to \mu^+\mu^-$ is $(20.9\text{ pb}) \times \sin^2 2\alpha$. The continuum limit arises from a stacked search of dwarf spheroidals for photons with $E > 1$ GeV and follows the analysis of Ref. [27]. Although this is not the most recent analysis and does not provide the most stringent limit from dwarf spheroidals, it is applicable here because it makes no assumption about the photon spectrum. Constraints are phrased in terms of a particle physics factor, Φ_{PP},

$$\Phi_{\text{PP}} = \frac{\langle\sigma v\rangle_{\text{ann.}}}{8\pi m_\chi^2} \int_{x_{\text{th}}}^1 dx \left(\frac{dN}{dx}\right)_{\text{cont.}} . \tag{6.7}$$

We take the constraint on Φ_{PP} from Ref. [27],

$$\Phi_{\text{PP}} = 5.0^{+4.3}_{-4.5} \times 10^{-30}\text{cm}^3\,\text{s}^{-1}\,\text{GeV}^{-2} .$$

For the μ final state, with small mixing angle, Φ_{PP} can be approximated by

$$\Phi_{\text{PP}} \approx \frac{\langle\sigma v\rangle_{\text{IB}}}{8\pi m_\chi^2} , \tag{6.8}$$

such that it can be directly translated into an upper limit for $\langle\sigma v\rangle_{\text{IB}}$. For small α, the IB spectrum for $\mu_1 = 1.44$ (left panel of Figure 6.15) might just marginally display a linelike

feature, while for $\mu_1 = 1.05$ (right panel of Figure 6.15), the spectrum is hard enough that it can be constrained by the Fermi-LAT line search [26]. The spectral features of both cases can be understood in light of Figure 6.13.

6.6.4 Constraints from cosmic ray e^+ fraction data

Strong constraints have also been derived from the nonobservation of bumps in the cosmic ray positron fraction due to dark matter annihilation by the AMS-02 [16]. Although the rise in the cosmic ray positron fraction remains unexplained, and could itself be due to dark matter with a mass large enough that a cutoff in the spectrum is not yet observed, lighter dark matter ($\lesssim 100$ GeV) would produce a bump with a cutoff at the dark matter mass if the annihilation rate is sufficiently high. Because the data are of extremely high quality, and no such bumps are observed, a limit on the annihilation cross section can be derived for any dark matter model. For annihilations of 100 GeV WIMPs to charged leptons, the constraints are near or even below the nominal thermal annihilation cross section, $\langle \sigma v \rangle_{\rm therm} \equiv 3 \times 10^{-26}$ cm^3 s^{-1}, as shown in Figure 1.8. For annihilations of 100 GeV dark matter particles to $\mu^+\mu^-$, $\langle \sigma v \rangle \gtrsim 2 \times 10^{-26}$ cm^3 s^{-1} is excluded. Though it is certainly possible for our scenario to have escaped detection, a modest improvement in this constraint may completely exclude our case of light smuons, assuming the only annihilation channel accessible is $\chi\chi \rightarrow \mu^+\mu^-$. For light staus, the current constraints are still a factor of a few above the thermal annihilation cross section, so those models are viable and will remain so for quite some time. And in all cases, the constraints are uncertain by a factor of a few in either direction due primarily to the lack of knowledge about the local density and the energy losses experienced by cosmic rays as they propagate throughout the Galaxy. Of course, if annihilations proceed to more than one final state, for example with some nonzero branching fraction to both muons and taus, then the constraints from indirect detection weaken in proportion to the branching fraction. We note that the constraints on lepton dipole moments would remain as presented, as they are not sensitive to the annihilation rate.

6.6.5 Constraints from the CMB power spectrum data

If dark matter particles annihilate at a sufficiently high rate, energy injection from DM annihilation can alter the recombination history, leading to changes in the temperature and

polarization power spectra of the CMB. CMB anisotropies offer an opportunity to constrain the nature of DM [17, 18, 253]. One of the benefits of this indirect detection technique is that it does not suffer from the astrophysical uncertainties of local signals. Furthermore, CMB experiments such as Planck can achieve limits on the annihilation cross section that are relevant for the interpretation of the rise in the cosmic-ray positron fraction at energies $E_{e^+} \gtrsim 10\,\mathrm{GeV}$ observed by the PAMELA, Fermi, and AMS. The Planck data exclude at 95% confidence level [50] a thermal relic cross section for light WIMPs of mass: $m_\chi \lesssim 44\,\mathrm{GeV}$ annihilating into e^+e^-; $m_\chi \lesssim 16\,\mathrm{GeV}$ annihilating into $\mu^+\mu^-$ or $\bar{b}b$; and $m_\chi \lesssim 11\,\mathrm{GeV}$ annihilating into $\tau^+\tau^-$. However, the constraints weaken for larger WIMP masses. For instance these constraints are still roughly an order of magnitude above a detectable signal for thermal 100 GeV dark matter annihilating into charged leptons. That analysis also shows that even a cosmic variance limited CMB experiment would still be a factor of a few above detection for a thermal 100 GeV dark matter particle.

CHAPTER 7

CONCLUSION

In this dissertation, we have considered a minimal leptophilic version of the MSSM, in which the parameters of the squark and slepton sector are decoupled. In particular, it is assumed that the squarks have large masses which are chosen to satisfy experimental constraints from the Higgs mass measurement, direct collider searches, and rare B decays. The parameters of the bino-slepton sector can then be chosen to address the now decoupled problem of achieving the correct dark matter relic density. The relic density depends only on the bino and slepton masses and the slepton mixing angle. In this simplified sector, there arises a new bulk-like region, in which the correct relic density is achieved with bino dark matter that annihilates through light mediating sleptons. The key region of parameter space is $m_\chi \sim m_{\tilde{\ell}_1} \sim 100$ GeV, with maximal L-R slepton mixing.

The most relevant constraints on this scenario arise from direct slepton searches, and from the contribution of bino-slepton loop diagrams to SM lepton dipole moments. In particular, the only channels for which the dark matter annihilation cross section in the current epoch could be $\sim$ 1 pb (subject to the above constraints) are $\tau^+\tau^-$ and $\mu^+\mu^-$. Moreover, if $\langle\sigma v\rangle_{\chi\chi\to\mu^+\mu^-} \sim 1$ pb, then there must be large CP violation in the smuon sector. p-wave suppressed dark matter annihilation to electrons could be relevant to dark matter freeze-out, but must be unobservable in the current epoch.

We have also considered the implications of this scenario; in particular, possible gamma-ray signatures from dark matter annihilation. We have studied the effect of chiral mixing and a CP-violating phase on the gamma-ray signals from dark matter annihilation into $\gamma\gamma$ and γZ, as well as the internal bremsstrahlung spectrum associated with dark matter

---

This chapter is adapted from published articles: Phys. Rev. D **90**, *095007 (2014). MSSM Dark Matter and a Light Slepton Sector: The Incredible Bulk. K. Fukushima, C. Kelso, J. Kumar, P. Sandick, T. Yamamoto.* ©*Owned by the authors, published by American Physical Society, 2014. and Phys. Rev. D* **94**, *015022 (2016). Gamma-Ray Signals from Dark Matter Annihilation via Charged Mediators. J. Kumar, P. Sandick, F. Teng, T. Yamamoto.* ©*Owned by the authors, published by American Physical Society, 2016. With kind permission of the American Physical Society.*

annihilation into a fermion pair.

We have found that varying the mixing angle results in a prompt photon spectrum for the process $\chi\chi \to \bar{f}f\gamma$ which interpolates between the standard regimes which are dominated by either virtual internal bremsstrahlung or soft/collinear final state radiation. In some regions of parameter space, this deviation from the standard spectrum will be observable, and can provide a clue as to the relative strength of deviations from minimal flavor violation in the underlying theory. For the $2 \to 3$ annihilation process, although the chiral mixing angle is very important in determining the spectrum, the CP-violating phase is less so.

On the other hand, the mixing angle and CP-violating phase are both important for monoenergetic annihilation signals. In particular, varying the mixing angle will change the relative branching fractions to the final states $\gamma\gamma$ and γZ. For sufficiently large couplings in the simplified model, this effect could be observed in future experiments with excellent energy resolution.

Interestingly, a nonvanishing CP-violating phase can result in an asymmetry in the left- vs. right-circularly polarized photons arising from dark matter annihilation. Current gamma-ray instruments are not capable of detecting such polarization for the energy range of interest. Experimental study of this scenario would require a new strategy. Monoenergetic photon signals from dark matter annihilation are sometimes considered the ultimate "smoking gun" for indirect detection; it would be interesting to further study the feasibility of observing the polarization asymmetry in this channel, which is a hallmark of CP-violation.

We present, for reference, a summary of the dark matter abundance and relevant annihilation cross sections for the benchmarks discussed throughout this dissertation in Table 7.1. Here, U. B. and O. B. denote underabundant and overabundant, respectively. $\langle\sigma v\rangle_{\rm IB}$ is integrated from $x = 0.2$. Note that all models satisfy the constraints on the dipole moments of the SM leptons, with the exception of Benchmark A, which does not exacerbate the problem of the muon anomalous magnetic moment, but also does not produce the measured value. If φ is shifted sightly to 0.49π, a_μ will fall into the 2σ range of current experimental measurement, while all the other quantities in the table above remain nearly unchanged. It would be interesting to consider the implications for this scenario if

Table 7.1. Physical quantities derived from our benchmark models.

Model	$\langle\sigma v\rangle_{\ell^+\ell^-}$ $\times 10^{-26}\,\mathrm{cm}^3/\mathrm{s}$	$\langle\sigma v\rangle_{\mathrm{IB}}$ $\times 10^{-27}\,\mathrm{cm}^3/\mathrm{s}$	$\Omega_c h^2$ (thermal)	$\langle\sigma v\rangle_{\gamma\gamma}$ $\times 10^{-28}\,\mathrm{cm}^3/\mathrm{s}$	$\langle\sigma v\rangle_{\gamma Z}$ $\times 10^{-32}\,\mathrm{cm}^3/\mathrm{s}$
A	2.127	4.917	0.1156	4.256×10^{-3}	2.89
B	2.010	2.872	0.1212	2.662×10^{-3}	3.03
C	2.128	3.046	0.1155	4.513×10^{-3}	2.88
D	46.95	108.5	U. B.	8.019×10^{-2}	–
D'	53.53	124.7	U. B.	0.1355	–
E	Forbidden	Forbidden	O. B.	2.9370	–

AMS-02 were to find evidence for dark matter annihilation to electrons or muons with $\langle\sigma v\rangle \sim 1$ pb, but not to taus or hadronic states, which could be distinguished by the absence of the associated photons. If interpreted within the framework of the MSSM, this data would imply that the LSP was largely bino-like, since any significant Higgsino or wino fraction would result in the production of hadronic final states which would yield anti-protons. Moreover, if the only final states consistent with the cosmic ray data were muons and electrons, then we could in fact conclude that the final state consisted of muons and that the mass of the smuons must be relatively light ($\mathcal{O}(100)GeV$). A large bino annihilation cross section to electrons would imply light selectrons and L-R mixing, which is ruled out by the electron electric and magnetic dipole moment bounds (absent some large fine-tuning). Finally, we could conclude that there was large L-R smuon mixing (in order to allow such a large annihilation cross section), and large CP-violation (in order to evade tight bounds from the measurements of the muon magnetic dipole moment).

It is remarkable that so much information could be gleaned about the parameters of the MSSM in this *new bulk* scenario with only data from AMS-02, even without new data from the LHC. But this new bulk region could be sharply probed in the next physics run of the LHC. If the mass of the lightest slepton can be constrained to be larger than ~ 150 GeV, then it would not be possible to explain the observed dark matter relic density without coannihilation in the early Universe, and/or a nontrivial wino/Higgsino fraction.

REFERENCES

[1] D. Larson et al., Astrophys. J. Suppl. **192**, 16 (2011).

[2] S. Courteau et al., Rev. Mod. Phys. **86**, 47 (2014).

[3] S. Blais-Ouellette, *Distribution de la matière sombre dans les galaxies spirales*, PhD thesis, Universitè de Montrèal, 2000.

[4] C. Patrignani et al., Chin. Phys. **C40**, 100001 (2016).

[5] J. Beringer et al., Phys. Rev. **D86**, 010001 (2012).

[6] M. Cahill-Rowley et al., Complementarity and Searches for Dark Matter in the pMSSM, in *Proceedings, 2013 Community Summer Study on the Future of U.S. Particle Physics: Snowmass on the Mississippi (CSS2013): Minneapolis, MN, USA, July 29-August 6, 2013*, 2013.

[7] G. Aad et al., JHEP **10**, 134 (2015).

[8] M. Ackermann et al., Phys. Rev. Lett. **115**, 231301 (2015).

[9] M. Ackermann et al., Astrophys. J. **761**, 91 (2012).

[10] A. Abramowski et al., Phys. Rev. Lett. **106**, 161301 (2011).

[11] J. Aleksić et al., JCAP **1402**, 008 (2014).

[12] K. N. Abazajian, N. Canac, S. Horiuchi, and M. Kaplinghat, Phys. Rev. **D90**, 023526 (2014).

[13] F. Calore, I. Cholis, and C. Weniger, JCAP **1503**, 038 (2015).

[14] C. Gordon and O. Macias, Phys. Rev. **D88**, 083521 (2013), [Erratum: Phys. Rev.D89,no.4,049901(2014)].

[15] T. Daylan et al., Phys. Dark Univ. **12**, 1 (2016).

[16] L. Bergstrom, T. Bringmann, I. Cholis, D. Hooper, and C. Weniger, Phys. Rev. Lett. **111**, 171101 (2013).

[17] S. Galli, F. Iocco, G. Bertone, and A. Melchiorri, Phys. Rev. **D80**, 023505 (2009).

[18] T. R. Slatyer, N. Padmanabhan, and D. P. Finkbeiner, Phys. Rev. **D80**, 043526 (2009).

[19] S. Galli, F. Iocco, G. Bertone, and A. Melchiorri, Phys. Rev. **D84**, 027302 (2011).

[20] T. R. Slatyer, Phys. Rev. **D87**, 123513 (2013).

[21] J. M. Cline and P. Scott, JCAP **1303**, 044 (2013), [Erratum: JCAP1305,E01(2013)].

[22] L. Lopez-Honorez, O. Mena, S. Palomares-Ruiz, and A. C. Vincent, JCAP **1307**, 046 (2013).

[23] M. Ackermann et al., Phys. Rev. Lett. **107**, 241302 (2011).

[24] S. P. Martin, (1997), [Adv. Ser. Direct. High Energy Phys.18,1(1998)].

[25] J. Ellis, F. Luo, K. A. Olive, and P. Sandick, Eur. Phys. J. **C73**, 2403 (2013).

[26] M. Ackermann et al., Phys. Rev. **D91**, 122002 (2015).

[27] A. Geringer-Sameth and S. M. Koushiappas, Phys. Rev. Lett. **107**, 241303 (2011).

[28] M. Peskin and D. Schroeder, *An Introduction to Quantum Field Theory*, Westview Press, 1995.

[29] M. S. Chanowitz, Ann. Rev. Nucl. Part. Sci. **38**, 323 (1988).

[30] S. Dawson, Introduction to electroweak symmetry breaking, in *Proceedings, Summer School in High-energy physics and cosmology: Trieste, Italy, June 29-July 17, 1998*, pages 1–83, 1998.

[31] S. Dawson, AIP Conf. Proc. **1116**, 11 (2009).

[32] F. Englert and R. Brout, Phys. Rev. Lett. **13**, 321 (1964).

[33] P. W. Higgs, Phys. Rev. Lett. **13**, 508 (1964).

[34] S. Chatrchyan et al., Phys. Lett. **B710**, 26 (2012).

[35] G. Aad et al., Phys. Lett. **B710**, 49 (2012).

[36] S. Chatrchyan et al., JHEP **06**, 081 (2013).

[37] S. Chatrchyan et al., Nature Phys. **10**, 557 (2014).

[38] S. Weinberg, Phys. Rev. Lett. **19**, 1264 (1967).

[39] S. Chatrchyan et al., Phys. Lett. **B716**, 30 (2012).

[40] G. Aad et al., Phys. Lett. **B716**, 1 (2012).

[41] T. Hambye and K. Riesselmann, SM Higgs mass bounds from theory, in *e+ e- linear colliders: Physics and detector studies. Proceedings, Workshops, ECFA/DESY, Frascati, Italy, February 5-6, 1996, London, UK, July 4-6, 1996, Munich, Germany, September 16-18, 1996 and Hamburg, Germany, November 20-22, 1996. Pt.E*, 1997.

[42] R. Barate et al., Phys. Lett. **B565**, 61 (2003).

[43] G. Isidori, V. S. Rychkov, A. Strumia, and N. Tetradis, Phys. Rev. **D77**, 025034 (2008).

[44] A. V. Bednyakov, B. A. Kniehl, A. F. Pikelner, and O. L. Veretin, Phys. Rev. Lett. **115**, 201802 (2015).

[45] E. Kolb and M. Turner, *The Early Universe*, Westview Press, 1994.

[46] B. Ryden, *Introduction to Cosmology*, Addison-Wesley, 2002.

[47] E. Hubble, Proc. Nat. Acad. Sci. **15**, 168 (1929).

[48] D. J. Fixsen, Astrophys. J. **707**, 916 (2009).

[49] R. Adam et al., Astron. Astrophys. **594**, A1 (2016).

[50] P. A. R. Ade et al., Astron. Astrophys. **594**, A13 (2016).

[51] P. A. R. Ade et al., Astron. Astrophys. **571**, A16 (2014).

[52] W. L. Freedman et al., Astrophys. J. **553**, 47 (2001).

[53] E. M. L. Humphreys, M. J. Reid, J. M. Moran, L. J. Greenhill, and A. L. Argon, Astrophys. J. **775**, 13 (2013).

[54] O. Lahav and A. R. Liddle, (2014).

[55] V. C. Rubin and W. K. Ford, Jr., Astrophys. J. **159**, 379 (1970).

[56] G. Bertone, D. Hooper, and J. Silk, Phys. Rept. **405**, 279 (2005).

[57] F. Iocco, M. Pato, and G. Bertone, Nature Phys. **11**, 245 (2015).

[58] F. Zwicky, Astrophys. J. **86**, 217 (1937).

[59] R. J. Scherrer and M. S. Turner, Phys. Rev. **D33**, 1585 (1986), [Erratum: Phys. Rev.D34,3263(1986)].

[60] H.-Y. Chiu, Phys. Rev. Lett. **17**, 712 (1966).

[61] B. W. Lee and S. Weinberg, Phys. Rev. Lett. **39**, 165 (1977).

[62] G. Steigman, Ann. Rev. Nucl. Part. Sci. **29**, 313 (1979).

[63] G. Jungman, M. Kamionkowski, and K. Griest, Phys. Rept. **267**, 195 (1996).

[64] R. Catena and P. Ullio, JCAP **1205**, 005 (2012).

[65] M. Pato, O. Agertz, G. Bertone, B. Moore, and R. Teyssier, Phys. Rev. **D82**, 023531 (2010).

[66] N. Bernal, J. E. Forero-Romero, R. Garani, and S. Palomares-Ruiz, JCAP **1409**, 004 (2014).

[67] S. Gillessen et al., Astrophys. J. **692**, 1075 (2009).

[68] J. Bovy, D. W. Hogg, and H.-W. Rix, Astrophys. J. **704**, 1704 (2009).

[69] A. M. Ghez et al., Astrophys. J. **689**, 1044 (2008).

[70] V. Gluscevic, M. I. Gresham, S. D. McDermott, A. H. G. Peter, and K. M. Zurek, JCAP **1512**, 057 (2015).

[71] R. Schoenrich, J. Binney, and W. Dehnen, Mon. Not. Roy. Astron. Soc. **403**, 1829 (2010).

[72] C. Savage, K. Freese, and P. Gondolo, Phys. Rev. **D74**, 043531 (2006).

[73] R. Bernabei et al., Phys. Part. Nucl. **46**, 138 (2015).

[74] C. Savage, G. Gelmini, P. Gondolo, and K. Freese, JCAP **0904**, 010 (2009).

[75] D. S. Akerib et al., Phys. Rev. Lett. **112**, 091303 (2014).

[76] C. Savage, A. Scaffidi, M. White, and A. G. Williams, Phys. Rev. **D92**, 103519 (2015).

[77] J. Cooley, Phys. Dark Univ. **4**, 92 (2014).

[78] K. Choi et al., Phys. Rev. Lett. **114**, 141301 (2015).

[79] J. F. Navarro, C. S. Frenk, and S. D. M. White, Astrophys. J. **462**, 563 (1996).

[80] F. Aharonian, Astron. Astrophys. **503**, 817 (2009).

[81] F. Acero, Mon. Not. Roy. Astron. Soc. **402**, 1877 (2010).

[82] M. Su, T. R. Slatyer, and D. P. Finkbeiner, Astrophys. J. **724**, 1044 (2010).

[83] T. A. Porter and S. Murgia, PoS **ICRC2015**, 815 (2016).

[84] D. Hooper and L. Goodenough, Phys. Lett. **B697**, 412 (2011).

[85] M. Cirelli, (2015).

[86] L. Accardo et al., Phys. Rev. Lett. **113**, 121101 (2014).

[87] M. Aguilar et al., Phys. Rev. Lett. **113**, 121102 (2014).

[88] O. Adriani et al., Phys. Rev. Lett. **111**, 081102 (2013).

[89] M. Cirelli, Pramana **79**, 1021 (2012).

[90] S. Profumo, Central Eur. J. Phys. **10**, 1 (2011).

[91] M. Kachelrieß, A. Neronov, and D. V. Semikoz, Phys. Rev. Lett. **115**, 181103 (2015).

[92] A. Askew, S. Chauhan, B. Penning, W. Shepherd, and M. Tripathi, Int. J. Mod. Phys. **A29**, 1430041 (2014).

[93] M. Aaboud et al., Phys. Lett. **B763**, 251 (2016).

[94] M. Aaboud et al., (2016).

[95] M. Beltran, D. Hooper, E. W. Kolb, Z. A. C. Krusberg, and T. M. P. Tait, JHEP **09**, 037 (2010).

[96] J. Goodman et al., Phys. Lett. **B695**, 185 (2011).

[97] Y. Bai, P. J. Fox, and R. Harnik, JHEP **12**, 048 (2010).

[98] J. Abdallah et al., Phys. Dark Univ. **9-10**, 8 (2015).

[99] J. Wess and B. Zumino, Nucl. Phys. **B70**, 39 (1974).

[100] H. Baer and X. Tata, *Weak scale supersymmetry: From superfields to scattering events*, Cambridge University Press, 2006.

[101] P. Draper and H. Rzehak, Phys. Rept. **619**, 1 (2016).

[102] M. T. Grisaru, W. Siegel, and M. Rocek, Nucl. Phys. **B159**, 429 (1979).

[103] N. Seiberg, Phys. Lett. **B318**, 469 (1993).

[104] P. Langacker and M.-x. Luo, Phys. Rev. **D44**, 817 (1991).

[105] G. F. Giudice and R. Rattazzi, Nucl. Phys. **B757**, 19 (2006).

[106] T. Hebbeker, Phys. Lett. **B470**, 259 (1999).

[107] H. V. Klapdor-Kleingrothaus et al., Eur. Phys. J. **A12**, 147 (2001).

[108] M. Drees and M. M. Nojiri, Phys. Rev. **D47**, 376 (1993).

[109] K. Griest and D. Seckel, Phys. Rev. **D43**, 3191 (1991).

[110] J. Hisano, S. Matsumoto, and M. M. Nojiri, Phys. Rev. Lett. **92**, 031303 (2004).

[111] M. Lattanzi and J. I. Silk, Phys. Rev. **D79**, 083523 (2009).

[112] N. Arkani-Hamed, D. P. Finkbeiner, T. R. Slatyer, and N. Weiner, Phys. Rev. **D79**, 015014 (2009).

[113] J. Hisano, S. Matsumoto, M. Nagai, O. Saito, and M. Senami, Phys. Lett. **B646**, 34 (2007).

[114] J. Fan and M. Reece, JHEP **10**, 124 (2013).

[115] J. Bramante et al., Phys. Rev. **D93**, 063525 (2016).

[116] J. R. Ellis, T. Falk, and K. A. Olive, Phys. Lett. **B444**, 367 (1998).

[117] J. R. Ellis, T. Falk, K. A. Olive, and M. Srednicki, Astropart. Phys. **13**, 181 (2000), [Erratum: Astropart. Phys.15,413(2001)].

[118] J. R. Ellis, K. A. Olive, and Y. Santoso, Astropart. Phys. **18**, 395 (2003).

[119] C. Boehm, A. Djouadi, and M. Drees, Phys. Rev. **D62**, 035012 (2000).

[120] P. Nath and R. L. Arnowitt, Phys. Rev. Lett. **70**, 3696 (1993).

[121] A. Djouadi, M. Drees, and J.-L. Kneur, Phys. Lett. **B624**, 60 (2005).

[122] S. Dimopoulos and D. W. Sutter, Nucl. Phys. **B452**, 496 (1995).

[123] D. W. Sutter, *The Supersymmetric flavor problem and $\mu \to e + \gamma$*, PhD thesis, Stanford U., Phys. Dept., 1995.

[124] F. Gabbiani, E. Gabrielli, A. Masiero, and L. Silvestrini, Nucl. Phys. **B477**, 321 (1996).

[125] M. J. Ramsey-Musolf and S. Su, Phys. Rept. **456**, 1 (2008).

[126] M. Carena, A. Menon, and C. E. M. Wagner, Phys. Rev. **D79**, 075025 (2009).

[127] S. Jager, Eur. Phys. J. **C59**, 497 (2009).

[128] W. Altmannshofer, A. J. Buras, S. Gori, P. Paradisi, and D. M. Straub, Nucl. Phys. **B830**, 17 (2010).

[129] W. Fischler, S. Paban, and S. D. Thomas, Phys. Lett. **B289**, 373 (1992).

[130] K. A. Olive, M. Pospelov, A. Ritz, and Y. Santoso, Phys. Rev. **D72**, 075001 (2005).

[131] M. Pospelov and A. Ritz, Annals Phys. **318**, 119 (2005).

[132] G. F. Giudice and A. Romanino, Phys. Lett. **B634**, 307 (2006).

[133] G. D'Ambrosio, G. F. Giudice, G. Isidori, and A. Strumia, Nucl. Phys. **B645**, 155 (2002).

[134] J. R. Ellis, S. Heinemeyer, K. A. Olive, A. M. Weber, and G. Weiglein, JHEP **08**, 083 (2007).

[135] S. Heinemeyer, X. Miao, S. Su, and G. Weiglein, JHEP **08**, 087 (2008).

[136] G.-C. Cho, K. Hagiwara, Y. Matsumoto, and D. Nomura, JHEP **11**, 068 (2011).

[137] T. Blum et al., (2013).

[138] P. Bechtle et al., Eur. Phys. J. **C76**, 96 (2016).

[139] S. R. Choudhury and N. Gaur, Phys. Lett. **B451**, 86 (1999).

[140] K. S. Babu and C. F. Kolda, Phys. Rev. Lett. **84**, 228 (2000).

[141] G. Isidori and A. Retico, JHEP **11**, 001 (2001).

[142] G. Isidori and A. Retico, JHEP **09**, 063 (2002).

[143] V. Khachatryan et al., Nature **522**, 68 (2015).

[144] R. Aaij et al., Phys. Rev. Lett. **110**, 021801 (2013).

[145] G. Aad et al., Phys. Lett. **B713**, 387 (2012).

[146] T. Aaltonen et al., Phys. Rev. Lett. **107**, 191801 (2011), [Addendum: Phys. Rev. Lett.107,no.23,239903(2011)].

[147] I. Adachi et al., Phys. Rev. Lett. **110**, 131801 (2013).

[148] J. P. Lees et al., Phys. Rev. Lett. **109**, 101802 (2012).

[149] J. P. Lees et al., Phys. Rev. **D88**, 072012 (2013).

[150] R. Aaij et al., Phys. Rev. Lett. **115**, 111803 (2015), [Addendum: Phys. Rev. Lett.115,no.15,159901(2015)].

[151] M. Huschle et al., Phys. Rev. **D92**, 072014 (2015).

[152] S. Chen et al., Phys. Rev. Lett. **87**, 251807 (2001).

[153] T. Hurth, E. Lunghi, and W. Porod, Nucl. Phys. **B704**, 56 (2005).

[154] P. Koppenburg et al., Phys. Rev. Lett. **93**, 061803 (2004).

[155] B. Aubert et al., Determination of the branching fraction for inclusive decays $B \to X_s\gamma$, in *High energy physics. Proceedings, 31st International Conference, ICHEP 2002, Amsterdam, Netherlands, July 25-31, 2002*, 2002.

[156] E. Barberio et al., (2006).

[157] O. Buchmueller et al., Eur. Phys. J. **C74**, 2922 (2014).

[158] F. Mahmoudi, S. Neshatpour, and J. Orloff, JHEP **08**, 092 (2012).

[159] A. Arbey, M. Battaglia, F. Mahmoudi, and D. Martínez Santos, Phys. Rev. **D87**, 035026 (2013).

[160] P. Gondolo and G. Gelmini, Nucl. Phys. **B360**, 145 (1991).

[161] G. Steigman, B. Dasgupta, and J. F. Beacom, Phys. Rev. **D86**, 023506 (2012).

[162] M. Srednicki, R. Watkins, and K. A. Olive, Nucl. Phys. **B310**, 693 (1988).

[163] H. Baer and M. Brhlik, Phys. Rev. **D53**, 597 (1996).

[164] H. Baer and M. Brhlik, Phys. Rev. **D57**, 567 (1998).

[165] H. Baer et al., Phys. Rev. **D63**, 015007 (2000).

[166] S. F. King and J. P. Roberts, JHEP **09**, 036 (2006).

[167] H. Baer, V. Barger, and A. Mustafayev, Phys. Rev. **D85**, 075010 (2012).

[168] G. L. Kane, C. F. Kolda, L. Roszkowski, and J. D. Wells, Phys. Rev. **D49**, 6173 (1994).

[169] J. R. Ellis, T. Falk, K. A. Olive, and M. Schmitt, Phys. Lett. **B388**, 97 (1996).

[170] J. R. Ellis, T. Falk, K. A. Olive, and M. Schmitt, Phys. Lett. **B413**, 355 (1997).

[171] J. R. Ellis, T. Falk, G. Ganis, K. A. Olive, and M. Schmitt, Phys. Rev. **D58**, 095002 (1998).

[172] V. D. Barger and C. Kao, Phys. Rev. **D57**, 3131 (1998).

[173] J. R. Ellis, T. Falk, G. Ganis, and K. A. Olive, Phys. Rev. **D62**, 075010 (2000).

[174] J. R. Ellis, T. Falk, G. Ganis, K. A. Olive, and M. Srednicki, Phys. Lett. **B510**, 236 (2001).

[175] V. D. Barger and C. Kao, Phys. Lett. **B518**, 117 (2001).

[176] L. Roszkowski, R. Ruiz de Austri, and T. Nihei, JHEP **08**, 024 (2001).

[177] A. Djouadi, M. Drees, and J. L. Kneur, JHEP **08**, 055 (2001).

[178] U. Chattopadhyay, A. Corsetti, and P. Nath, Phys. Rev. **D66**, 035003 (2002).

[179] J. R. Ellis, K. A. Olive, and Y. Santoso, New J. Phys. **4**, 32 (2002).

[180] H. Baer et al., JHEP **07**, 050 (2002).

[181] R. L. Arnowitt and B. Dutta, Dark matter, muon g-2 and other accelerator constraints, in *Proceedings, 4th International Workshop on The identification of dark matter (IDM 2002): York, UK, September 2-6, 2002*, pages 114–121, 2002.

[182] J. R. Ellis, K. A. Olive, Y. Santoso, and V. C. Spanos, Phys. Lett. **B565**, 176 (2003).

[183] H. Baer and C. Balazs, JCAP **0305**, 006 (2003).

[184] A. B. Lahanas and D. V. Nanopoulos, Phys. Lett. **B568**, 55 (2003).

[185] U. Chattopadhyay, A. Corsetti, and P. Nath, Phys. Rev. **D68**, 035005 (2003).

[186] C. Munoz, Int. J. Mod. Phys. **A19**, 3093 (2004).

[187] R. L. Arnowitt, B. Dutta, and B. Hu, Dark matter, muon g-2 and other SUSY constraints, in *Beyond the desert. Proceedings, 4th International Conference, Particle physics beyond the standard model, BEYOND 2003, Castle Ringberg, Tegernsee, Germany, June 9-14, 2003*, pages 25–41, 2003.

[188] J. Ellis and K. A. Olive, (2010).

[189] M. Kadastik, K. Kannike, A. Racioppi, and M. Raidal, JHEP **05**, 061 (2012).

[190] C. Strege et al., JCAP **1203**, 030 (2012).

[191] H. Baer, V. Barger, and A. Mustafayev, JHEP **05**, 091 (2012).

[192] S. Akula, P. Nath, and G. Peim, Phys. Lett. **B717**, 188 (2012).

[193] D. Ghosh, M. Guchait, S. Raychaudhuri, and D. Sengupta, Phys. Rev. **D86**, 055007 (2012).

[194] A. Fowlie et al., Phys. Rev. **D86**, 075010 (2012).

[195] O. Buchmueller et al., Eur. Phys. J. **C72**, 2243 (2012).

[196] S. Akula and P. Nath, Phys. Rev. **D87**, 115022 (2013).

[197] M. Ibe, T. T. Yanagida, and N. Yokozaki, JHEP **08**, 067 (2013).

[198] J. L. Evans, M. Ibe, K. A. Olive, and T. T. Yanagida, Eur. Phys. J. **C74**, 2775 (2014).

[199] M. R. Buckley, D. Hooper, and J. Kumar, Phys. Rev. **D88**, 063532 (2013).

[200] A. Pierce, N. R. Shah, and K. Freese, (2013).

[201] J. Edsjo, *Aspects of neutrino detection of neutralino dark matter*, PhD thesis, Uppsala U., 1997.

[202] K. Fukushima, C. Kelso, J. Kumar, P. Sandick, and T. Yamamoto, Phys. Rev. **D90**, 095007 (2014).

[203] J. Hisano and S. Sugiyama, Phys. Lett. **B696**, 92 (2011), [Erratum: Phys. Lett.B719,472(2013)].

[204] G. Belanger, S. Biswas, C. Boehm, and B. Mukhopadhyaya, JHEP **12**, 076 (2012).

[205] G. Bélanger et al., Phys. Lett. **B726**, 773 (2013).

[206] V. Lefranc and E. Moulin, PoS **ICRC2015**, 1208 (2016).

[207] M. Actis et al., Exper. Astron. **32**, 193 (2011).

[208] N. Topchiev et al., PoS **ICRC2015**, 1026 (2016).

[209] L. Bergstrom and P. Ullio, Nucl. Phys. **B504**, 27 (1997).

[210] Z. Bern, P. Gondolo, and M. Perelstein, Phys. Lett. **B411**, 86 (1997).

[211] P. Ullio and L. Bergstrom, Phys. Rev. **D57**, 1962 (1998).

[212] T. Bringmann, L. Bergstrom, and J. Edsjo, JHEP **01**, 049 (2008).

[213] T. Bringmann and F. Calore, Phys. Rev. Lett. **112**, 071301 (2014).

[214] H. Elvang and Y.-t. Huang, (2013).

[215] T. Hahn and M. Perez-Victoria, Comput. Phys. Commun. **118**, 153 (1999).

[216] T. Hahn, Comput. Phys. Commun. **140**, 418 (2001).

[217] R. K. Ellis, Z. Kunszt, K. Melnikov, and G. Zanderighi, Phys. Rept. **518**, 141 (2012).

[218] L. Bergstrom, Phys. Lett. **B225**, 372 (1989).

[219] J. Kumar and D. Marfatia, Phys. Rev. **D88**, 014035 (2013).

[220] K. Cheung, O. C. W. Kong, and J. S. Lee, JHEP **06**, 020 (2009).

[221] K. Fukushima and J. Kumar, Phys. Rev. **D88**, 056017 (2013).

[222] G. Aad et al., JHEP **09**, 176 (2014).

[223] S. Chatrchyan et al., JHEP **06**, 055 (2014).

[224] M. E. Cabrera, A. Casas, R. Ruiz de Austri, and G. Bertone, JHEP **12**, 114 (2014).

[225] M. E. Cabrera-Catalan, S. Ando, C. Weniger, and F. Zandanel, Phys. Rev. **D92**, 035018 (2015).

[226] T. A. collaboration, (2013).

[227] V. Khachatryan et al., Eur. Phys. J. **C74**, 3036 (2014).

[228] A. Heister et al., Phys. Lett. **B544**, 73 (2002).

[229] P. Achard et al., Phys. Lett. **B580**, 37 (2004).

[230] J. Abdallah et al., Eur. Phys. J. **C31**, 421 (2003).

[231] G. Abbiendi et al., Eur. Phys. J. **C14**, 51 (2000).

[232] G. Aad et al., JHEP **05**, 071 (2014).

[233] S. Chatrchyan et al., JHEP **11**, 147 (2012).

[234] G. Aad et al., JHEP **05**, 071 (2014).

[235] S. Chatrchyan et al., JHEP **11**, 147 (2012).

[236] J. Eckel, M. J. Ramsey-Musolf, W. Shepherd, and S. Su, JHEP **11**, 117 (2014).

[237] T. Aoyama, M. Hayakawa, T. Kinoshita, and M. Nio, Phys. Rev. Lett. **109**, 111807 (2012).

[238] S. G. Karshenboim, Phys. Usp. **56**, 883 (2013), [Usp. Fiz. Nauk183,935(2013)].

[239] J. Baron et al., Science **343**, 269 (2014).

[240] G. W. Bennett et al., Phys. Rev. **D80**, 052008 (2009).

[241] S. Eidelman and M. Passera, Mod. Phys. Lett. **A22**, 159 (2007).

[242] J. Abdallah et al., Eur. Phys. J. **C35**, 159 (2004).

[243] K. Inami et al., Phys. Lett. **B551**, 16 (2003).

[244] M. J. Booth, (1993).

[245] M. Wood et al., Prospects for Indirect Detection of Dark Matter with CTA, in *Proceedings, Community Summer Study 2013: Snowmass on the Mississippi (CSS2013): Minneapolis, MN, USA, July 29-August 6, 2013*, 2013.

[246] X. Huang et al., Astropart. Phys. **78**, 35 (2016).

[247] C. E. Yaguna, Phys. Rev. **D80**, 115002 (2009).

[248] M. Di Mauro, F. Donato, N. Fornengo, and A. Vittino, JCAP **1605**, 031 (2016).

[249] J. Rico, M. Wood, A. Drlica-Wagner, and J. Aleksić, PoS **ICRC2015**, 1206 (2016).

[250] M. Ackermann et al., Phys. Rev. **D89**, 042001 (2014).

[251] A. A. Moiseev et al., Dark Matter Search Perspectives with GAMMA-400, in *Proceedings, 33rd International Cosmic Ray Conference (ICRC2013): Rio de Janeiro, Brazil, July 2-9, 2013*, page 0626, 2013.

[252] L. Bergstrom, G. Bertone, J. Conrad, C. Farnier, and C. Weniger, JCAP **1211**, 025 (2012).

[253] D. P. Finkbeiner, S. Galli, T. Lin, and T. R. Slatyer, Phys. Rev. **D85**, 043522 (2012).